universität wien

DISSERTATION / DOCTORAL THESIS

Titel der Dissertation /Title of the Doctoral Thesis

„Nucleo-cytoplasmic compartmentalization after an open mitosis“

verfasst von / submitted by

Mina Petrovic

angestrebter akademischer Grad / in partial fulfilment of the requirements for the degree of

Doctor of Philosophy (PhD)

Wien, 2021/ Vienna 2021

Studienkennzahl lt. Studienblatt / degree programme code as it appears on the student record sheet:	UA 794 685 490
Dissertationsgebiet lt. Studienblatt / field of study as it appears on the student record sheet:	Molekulare Biologie
Betreut von / Supervisor:	Dipl.-Biol. Dr. Daniel Gerlich

Acknowledgements

This thesis would not have been possible without the support of several people, whom I give a special thank you to.

Firstly, I thank Daniel, for his mentorship and guidance on both scientific and personal aspect. I am honored to have had him as a PhD supervisor as along the way I learned so much, not only about the life of cells, but also about the life of scientists. I am particularly grateful for Daniel's understanding attitude which was essential in scientifically demanding times. Next, I would like to thank Gerlich lab members, for their scientific support, but more importantly for always cheering me on and being by my side. You guys are the best, I will miss the joyful spirit of the lab the most. A special thank you goes to Claudia, for being the root of this lab and making me feel at home. None of this would be possible without you and having you as a friend is a true privilege.

I would further like to thank my thesis committee members for their guidance on my PhD journey, particularly Sara Cuylen-Haering for her constant support and patience during manuscript finalization. My project would not have succeeded without all the help from the VBC facility services, and a special shout out goes to Pawel, Tobias, and Alberto for all the imaging issues they resolved on the fly. Further I thank Liam Holt, for sharing valuable reagents designed in his lab which were key to our scientific discoveries. I also want to thank my PhD selection and the PhD program organizers, for providing scientific and administrative support that made this a much smoother ride.

More on, I would like to thank my best friend Ina, for being there through thick and thin, for all the laughs, all-night studying sessions, endless experiment troubleshooting, for keeping me relaxed and making me go on. Then I must thank Petar, for his sassiness is the main spice of my life, and for fighting all my battles alongside. Milos, thank you for constant reminders that life is more than science. Danezi, thank you for being my rock and inspiring me to do more. And thank you to my roots, Diva i entourage, I would never be where I am without the power and wit of these strong women.

The final thank you goes to the members of my family. To my aunt, for believing in me and supporting me from the first step I took at university. To my sister, for always having my back no matter how far apart we are. And finally thank you mom and dad, for always being my haven, the wind in my back, and for letting me make my own choices. I could never make it without you.

Table of Contents

Abstract

Cells of animals and plants disassemble their nucleus during mitosis such that mitotic chromosomes can be segregated by the mitotic spindle. The loss of a nuclear envelope barrier leads to intermixing of nuclear and cytoplasmic components and exposes chromosomes to a plethora of cytoplasmic macromolecules. At the end of mitosis, nuclear and cytoplasmic compartments are reestablished, and macromolecules of up to 40 nm diameter are retargeted to their designated compartments via transport through the nuclear pores. How components larger than the size limit of nuclear pores are moved out of the nucleus at the end of mitosis is unclear. By imaging fluorescent nanoparticles and mature ribosomes, we demonstrate that the bulk mass of large cytoplasmic components is removed from the reassembling nucleus by coalescence of chromosomes to a dense cluster prior to nuclear envelope assembly. We found that chromosome clustering is regulated by a chromosome periphery protein Ki-67, whose molecular brushes reorganize during mitotic exit. By manipulating electrical charge of various cytoplasmic probes, we further show that electrostatic interactions are a key regulator of cytoplasmic exclusion from compact mitotic chromosomes. Besides a role in removing cytoplasm during nuclear assembly, the exclusion of negatively charged cytoplasmic components also helps keeping tubulin dimers out of mitotic chromosomes to warrant their faithful segregation. Taken together, our study provides insights on how chromosomes keep cytoplasmic components at their proper locations during and after open mitosis.

Zusammenfassung

Tierische und pflanzliche Zellen bauen während der Mitose ihren Kern ab, so dass die mitotischen Chromosomen durch die mitotische Spindel segregiert werden können. Verlust der Kernhüllenbarriere führt zu einer Vermischung von Kern- und Zytoplasmabestandteilen und setzt die Chromosomen einer Fülle von zytoplasmatischen Makromolekülen aus. Am Ende der Mitose werden die Kern- und Zytoplasma-Kompartimente wiederhergestellt, und Makromoleküle mit einem Durchmesser von bis zu 40 nm werden durch die Kernporen wieder in ihre vorgesehenen Kompartimente transportiert. Wie die Komponenten, die größer als die Größengrenze der Kernporen sind, am Ende der Mitose aus dem Zellkern transportiert werden, ist unklar. Mit Hilfe von fluoreszierenden Nanopartikeln und Ribosomen zeigen wir, dass die Masse großer zytoplasmatischer Komponenten aus dem neu zusammensetzenden Kern entfernt wird, indem die Chromosomen vor dem Zusammenbau der Kernhülle zu einem dichten Cluster zusammenkommen. Die Chromosomenclusterung wird durch das Chromosomenperipherieprotein Ki-67 reguliert, dessen molekulare Bürsten sich am Ende der Mitose reorganisieren. Durch Manipulation der elektrischen Ladung verschiedener zytoplasmatischer Sonden zeigen wir ausserdem, dass elektrostatische Wechselwirkungen ein wichtiger Regulator der zytoplasmatischen Partitionierung relativ zu kompakten mitotischen Chromosomen während der offenen Mitose sind. Neben dem Ausschluss von zytoplasmatischen Komponenten während des Kernaufgbus spielt die elektrostatische Abstoßung von löslichen Tubulin-Dimeren zum Ausschluss von Mikrotubuli aus chromosomalen Regionen bei, was für die korrekte Chromosomensegregation wichtig ist. Zusammengenommen liefert unsere Studie Erkenntnisse darüber, wie Chromosomen das Zytoplasma am rechten Ort in der Zelle halten während und nach der offenen Mitose.

1 Introduction

1.1. Quiescent and dividing cells

The cell is the basic structural and functional unit of life. The continuation of life is ensured by cell division, a complex and well-orchestrated process through which cells multiply. Depending on the outside stimuli and environmental signaling, cells decide whether to stay in a paused, so-called quiescent state, or enter the cell cycle which leads to cell division[1]. Immortal cell lines allow the studying of molecular aspects of the human cell cycle on a single cell level. Genetic manipulation of such isolated cells, as well as the advancement of microscopy and molecular biology techniques continue to provide better understanding of the mammalian cell division process.

1.2. Main events of the cell cycle

The eukaryotic cell cycle is comprised of two main stages: interphase, during which a cell prepares for division, and mitosis, during which a cell divides into two new daughter cells (Fig. 1.1, adapted from [2]). Interphase is divided into three phases, two gap phases G1 and G2 which occur before and after S phase, respectively. When a cell receives mitogenic signals and leaves its quiescent G0 state, it enters G1 phase of interphase. Alternatively, a cell may enter G1 phase after having gone through mitosis, if the conditions continue to favor cell cycling over quiescence. The G1 phase is the longest phase in which cells grow and synthesize proteins necessary for further cell cycle progression. In S phase cells replicate their entire genome. Replication of every deoxyribonucleic acid (DNA) molecule leaves each chromosome with two identical sister chromatids. In G2 phase cells continue to synthesize proteins required for subsequent cell cycle phases, but also duplicate their organelles and repair any DNA breakages that may have occurred during replication.

Cell division consists of 5 main phases: prophase, prometaphase, metaphase, anaphase and telophase. Prophase is characterized by chromatin compaction and chromosome formation. Compact chromosome bodies consist of two sister chromatids joined at the centromere region. In early prophase chromosomes are still tethered to the intact nuclear envelope. In prophase centrioles separate and start traveling towards opposite cell poles, while microtubules polymerize to form the mitotic spindle. In late prophase and prometaphase of higher eukaryotes the nuclear envelope breaks down and chromosomes detach from envelope sheets which then become part of the endoplasmic reticulum (ER). Growing microtubules attach to chromosomes via protein complex called kinetochore, localized in the centromeric chromosomal region, and guide chromosomes towards the cell equator. In metaphase,

chromosomes are aligned in the cell center forming the metaphase plate, with each sister chromatid oriented towards one of the cell poles and attached to a separate bundle of microtubules. At anaphase onset, sister chromatids separate, and two copies of the duplicated genome are moved by the spindle towards opposite cell poles. In telophase chromosomes start decondensing and are again enclosed by the nuclear envelope, reforming a functional nucleus. The last stage of mitosis is the division of cytoplasm, cytokinesis, which is completed by the separation of cell membrane and formation of two independent daughter cells[3].

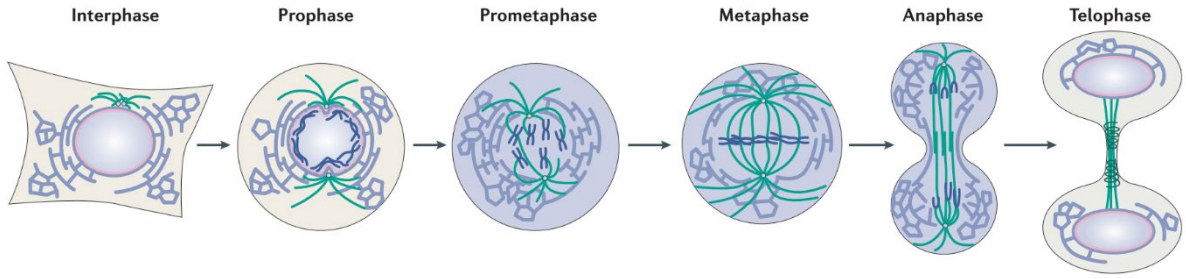

Figure 1.1. **Phases of the cell cycle**. Adapted from [2].

The order of cell cycle events is tightly regulated to ensure proper transfer of the genetic material through cell generations. The main regulators of the cell cycle are protein complexes comprised of two subunits, enzymatic cyclin-dependent kinase (CDK) subunit, and a regulatory cyclin subunit[4]. The levels of CDKs throughout the cell cycle remain relatively constant, while the concentration of cyclins changes in different stages, ensuring timely activation of their enzymatic partner[1].

1.3. Cell cycle regulation

1.3.1. Cyclin-CDK cell cycle regulation

According to the traditional cell cycle regulation model, the holoenzymes that regulate the beginning of the cell cycle are cyclinD-CDK4 and cyclinD-CDK6. When a cell receives mitogenic or growth factor signals from the environment, it activates a phosphorylation cascade through Ras-Raf-MAPK pathway, which leads to cyclin D synthesis and subsequent CDK4 and CDK6 activation[5]. In early G1 phase, these kinases phosphorylate retinoblastoma (Rb) pocket proteins[6] which causes their dissociation from E2F transcription factor proteins and subsequent transcription initiation. This ensures synthesis of factors necessary for G1/S transition and DNA replication, such as E-cyclins[7,8]. In late G1, newly synthesized E-cyclins form complexes with CDK2 to phosphorylate substrates required for further S phase preparation, such as proteins necessary for histone expression, centrosome duplication, DNA repair etc[9].

When a cell enters S phase, cyclin E is degraded and replaced with cyclin A bound to CDK2[10]. Cyclin A-CDK2 complexes phosphorylate cell division control protein homolog 6 (CDC6) which induces its export from the nucleus and prevents re-replication[11]. Further on, phosphorylation of repressor proteins enables transcription of histone genes[12]. Most importantly, cyclin A-CDK2 phosphorylation of CDC20 protein enables further cell cycle progression[13].

During late S phase the levels of cyclin B start to increase and cyclin B-CDK1 complexes form, yet they remain inactive until late G2 phase. This holoenzyme is the master regulator of mitotic progression and regulates key mitotic events until cyclin B degradation in late anaphase[14]. In early mitotic stages cyclin B-CDK1 phosphorylates nuclear lamins, lamin B receptor protein (LBR) and nucleoporins leading to the disassembly of the nuclear envelope and nuclear pores[15]. Further on, CDK1-dependent phosphorylation prevents re-replication, globally inhibits transcription and translation, and promotes centrosome separation and chromosome condensation[16,17,18]. During metaphase to anaphase transition, cyclin B-CDK1 phosphorylates CDC20, a cofactor of anaphase promoting complex (APC or cyclosome) which leads to sister chromatid separation and cyclin B degradation by the proteasome[19]. Cyclin B degradation decreases CDK1 activity in late mitosis and allows the APC complex to contact another cofactor CDH1 (CDC20 homologue 1). This triggers further APC-induced degradation of all cyclins and establishes a reset point for the start of a new cell cycle[19] (Fig. 1.2, adapted from [20]).

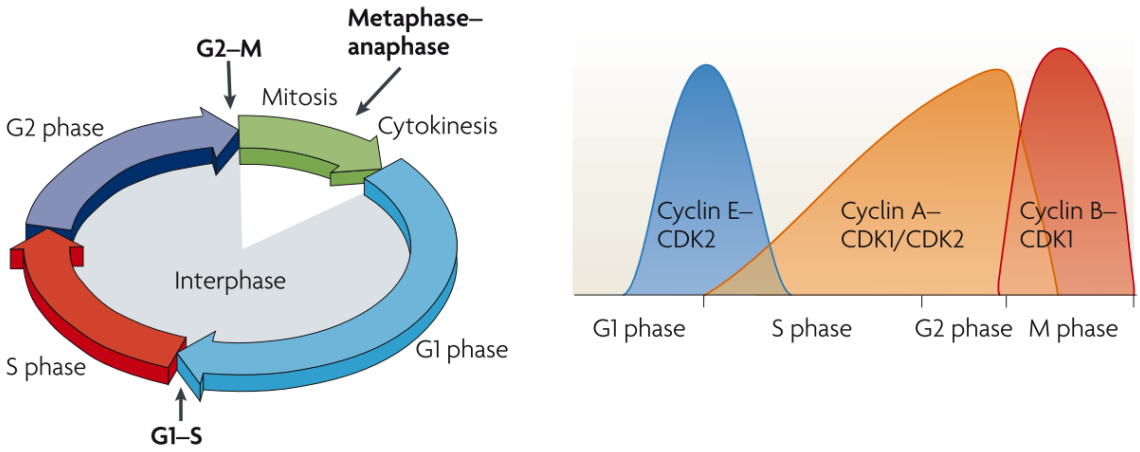

Figure 1.2. **The classical model of cell cycle regulation.** Different cyclin-CDK complexes are active during different stages of the cell cycle: cyclin E-CDK2 regulates late G1 phase, cyclin A-CDK1/CDK2 regulates S and G2 phase, while cyclin B-CDK1 regulates mitosis. For full cell cycle progression three main checkpoints must be satisfied: at G2-M transition, directly before anaphase onset, and prior to S phase entry. Adapted from [20].

It is important to emphasize that apart from cyclin binding, CDK activity is additionally regulated through phosphorylation, interaction with inhibitor proteins, degradation, and through cellular localization[1]. Finally, although the classical view proposes sequential

activation of different cyclins guiding cells through the cell cycle, recent studies suggest that CDKs have partially redundant functions[4].

1.3.2. Cell cycle checkpoints

In preparation for each cell division, a cell must double its contents to provide enough nutrients, proteins, lipid membranes, organelles etc. to each daughter cell. Therefore, cell size represents one of the key criteria monitored before cell division commitment. Cell growth occurs in G1 and G2 phase and cell size during these phases influences the length of stay in the phase- large cells progress towards mitosis faster[21]. The molecular mechanism of cell size sensing is not known. A potential sensor could be the number of synthesized proteins. Ribosomal content of a cell should directly correlate with its size, therefore the amount of protein synthesized might be a good size indicator[22].

Entry into mitosis requires that chromosomal DNA is intact, which is ensured by DNA damage repair checkpoints. These checkpoints prevent premature activation of CDKs and resolve issues which may cause replisome stalling during S-phase[23,24,25].

If DNA replication and cell growth have been successful, the mitotic kinase CDK1 triggers mitotic entry. The prerequisites for anaphase progression are biorientation of sister chromatids and proper microtubule- kinetochore attachment. The checkpoint verifying these requirements is the Spindle Assembly Checkpoint (SAC)[26]. Proper kinetochore-microtubule attachment is sensed by the protein MAD2, component of mitotic checkpoint complex (MCC)[27]. Cell treatment with microtubule-depolymerizing compound nocodazole causes accumulation of MAD2 on chromosomes and SAC activation, while spindle attachment to kinetochores reduces MAD2 levels and inactivates SAC[28]. The microtubule motor dynein plays an important role in SAC inactivation at anaphase onset because it strips several SAC proteins from kinetochores and enables their concentration at the cell poles[29]. Another way of SAC inactivation is through the tension generated by the properly attached bi-oriented sister chromatids. Amphitelic kinetochore attachments stretch out centromeric chromatin, increase kinetochore distance and produce tension which stabilizes kinetochore-microtubule interactions[30]. In case both sister chromatids attach to the microtubules originating from the same spindle pole (syntelic attachment), lack of tension causes destabilization of such attachments through the action of SAC component, Aurora B kinase[31]. The most critical role of Aurora B is in correcting merotelic attachments – a situation in which one sister kinetochore is connected to microtubules from both cell poles. Aurora B kinase controls several complexes at the kinetochore-microtubule binding site and can reactivate the SAC through destabilization of faulty attachments[32]. Therefore, Aurora B is not necessary to sustain mitotic arrest in

nocodazole treatment which causes spindle depolymerization, but it is crucial in taxol treatment which stabilizes microtubules and does not disturb kinetochore occupancy[33,34]. Finally, inhibition of Aurora B causes a significant reduction of MAD2 levels in nocodazole treated cells, eventually leading to SAC inactivation regardless of kinetochore occupancy[35].

As mitosis involves drastic cellular reorganization, it is essential that all cell compartments are properly reconstituted in the emerging daughter cells. In animal cells, which completely disassemble the cell nucleus during cell division, a key requirement is the proper nuclear reassembly after mitosis.

1.4. Interphase cell compartmentalization

1.4.1. The cell nucleus

1.4.1.1. Interphase chromatin organization

The nucleus is a membrane-bounded compartment of eukaryotic cells which stores genetic material during interphase. Up to several-meter-long DNA molecules are packed into a µm-sized nucleus, bordered by the nuclear envelope. Such tight packaging of DNA is achieved through several mechanisms[36]. Firstly, DNA is wrapped around histone protein complexes to form nucleosomes. Post-translational modifications of histones are implicated as one of the regulators of chromatin organization[37]. Further on, chromatin organization depends on the process of loop extrusion, performed by the Structural Maintenance of Chromosomes (SMC) proteins[38]. In interphase, the loop extruding complex is cohesin. Using ATP hydrolysis, cohesin complex protrudes DNA fiber through the ring formed from its subunits shaping it into a loop whose ends are brough into proximity[39]. On a large scale, interphase chromatin is comprised of spatially separated chromosomal territories, each storing the DNA content of one chromosome that includes both active and inactive chromatin types[40]. The transcription status of chromatin has been correlated with the level of compaction – densely packed heterochromatin regions are usually repressed, while open chromatin provides accessibility to the transcription machinery[40]. Histone acetylation is a common mark of active open chromatin, which is removed prior to mitotic entry to allow compact mitotic chromosome formation[41,42].

1.4.1.2. The nucleolus

The nucleolus is a prominent and well-characterized nuclear organelle. Mammalian cell nucleoli are separated into three sub-compartments: the fibrillar center (FC) surrounded by the dense fibrillar component (DFC), embedded together into the granular component (GC)[43] (Fig. 1.3, adapted from [43]). These compartments organize around tandem repeats of ribosomal

DNA (rDNA) genes on acrocentric chromosomes and have the major role in ribosomal biogenesis[44]. Ribosomal biogenesis begins with the transcription of rDNA genes by RNA pol I at the border of FC and DFC. Newly synthesized 47S transcript is then cleaved into 28S, 18S and 5.8S rRNAs (ribosomal ribonucleic acids) and post-transcriptionally modified by small nucleolar ribonucleoproteins (snoRNPs) which accumulate in the DFC region. Transcripts are then assembled into pre-ribosomal particles through addition of several ribosomal proteins in the GC region, and sent off to the nucleoplasm, where further modifications are made (for instance addition of 5S rRNA) before export through the nuclear pores[45] (Fig. 1.3, adapted from [43]). Although nucleoli are not surrounded by a membrane barrier, they represent separated entities within the nucleus with a distinct roughly spherical shape[46]. Recent studies show that nucleolar biogenesis depends on liquid-liquid phase separation (LLPS). Multiphase liquid immiscibility might be the base for layered nucleolar appearance[47]. Nucleolar proteins often contain intrinsically disordered as well as glycine-arginine rich regions which could drive LLPS[48]. *In vitro* experiments support this idea since both fibrillarin (present in the DFC) and nucleophosmin (present in the GC) phase separate *in vitro*, particularly in the presence of rRNAs, but do not favor mutual interactions[49,50,51]. Nucleoli transiently disassemble during each open mitosis. The key role in organization of nucleolar components during this time plays nucleolar protein Ki-67. It organizes chromosome periphery, a thick layer on the surface of mitotic chromosomes, which retains most of the nucleolar components[52].

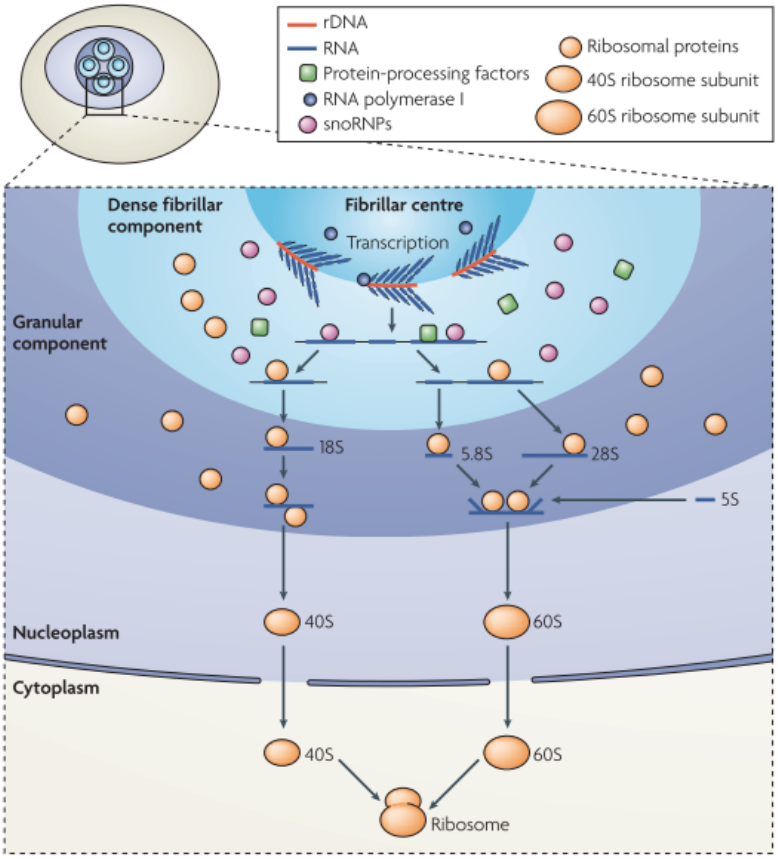

Figure 1.3. **Nucleolar organization and ribosome synthesis**. Mammalian nucleoli are separated into three sub-compartments: fibrillar center (FC), dense fibrillar component (DFC) and granular component (GC). rDNA transcription occurs at the boundary between FC and DFC. The transcripts are spliced and modified in the DFC and ribonuclear proteins added in GC. Final maturation of ribosomal subunits is finished in nucleoplasm, after which they are transported to cytoplasm. Mature translationally competent ribosomes assemble by joining of the two subunits in the cytoplasm. Adapted from [43].

1.4.1.3. Nuclear envelope and transport

The cell nucleus is enwrapped by the nuclear envelope (NE), a continuation of the endoplasmic reticulum (ER) made up of a double lipid bilayer. The bilayer closer to the inner nuclear space is referred to as inner nuclear membrane (INM), while the bilayer closer to the cytoplasm represents the outer nuclear membrane (ONM). Perinuclear space localized between the two membranes is continuous with the lumen of the ER. The INM and ONM fuse at numerous sites to form nuclear pores- places of exchange between the nucleus and the cytoplasm[2]. This exchange is tightly regulated by nucleoporins (NUPs), proteins which form large nuclear pore complexes (NPCs)[53]. Both the INM and ONM contain many proteins that provide additional communication between compartments. Linker of nucleoskeleton and cytoskeleton (LINC) complexes are comprised of SUN domain proteins and nesprins and are responsible for force transmission by connecting cytoskeletal elements of the nucleus and the cytoplasm[54]. Beneath the INM on the nuclear side in metazoan cells is the nuclear lamina, an

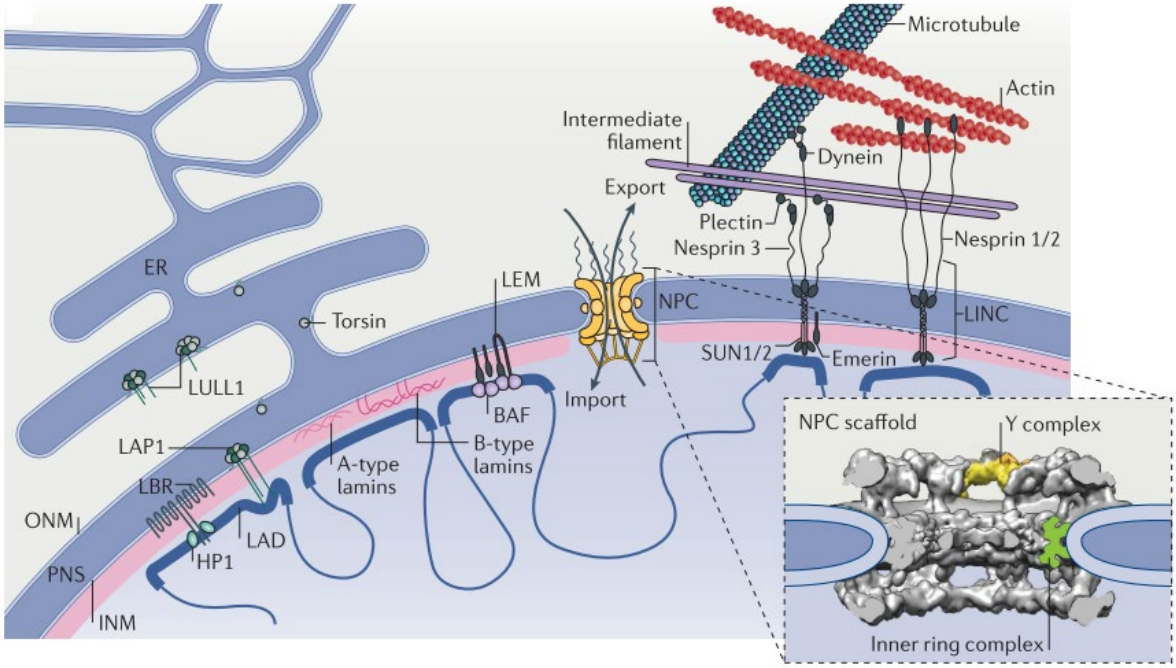

Figure 1.4. **Nuclear envelope (NE) organization**. Two lipid bilayers, inner and outer nuclear membrane (INM and ONM) enclose the perinuclear space. Nuclear lamina is located under INM and contacts heterochromatic regions termed lamina-associated domains (LADs). The transport through the NE occurs through nuclear pore complexes (insert). Adapted from [2].

additional supportive layer comprised of two types of intermediate filaments, A-type and B-type lamins[55]. The balance between the two types of lamins defines the level of nuclear envelope rigidity, A-type lamins confer nuclear stiffness, while B-type lamins confer elasticity[56]. Specific regions of heterochromatin, lamina associated domains (LADs), bind to nuclear lamina, and establish communication between the nuclear envelope and the genome (Fig.

1.4, adapted from [2]). This way nuclear lamina plays a role in chromatin organization and in genome expression[57].

NPCs are large complexes comprised of 30 different evolutionary conserved proteins, nucleoporins, and have a mass of 120 MDa in humans[58]. The structure of the NPC can be divided into three ring complexes: the inner pore ring, embedded at the fusion place of INM and ONM; the cytoplasmic ring; and the nuclear ring, localized at the cytoplasmic and nuclear side of the membrane fusion site and anchored by the inner ring (Fig. 1.4, inset, adapted from [2]). Additional peripheral elements extend into the nucleoplasm and cytoplasm, nuclear basket bound to the nuclear ring, and cytoplasmic filaments, extending from the cytoplasmic ring[59]. Most nucleoporins can be characterized either as scaffold NUPs, which have structured protein domains and serve primarily as building blocks, or FG-NUPs that are enriched with disordered phenylalanine-glycine repeats and are directly involved in controlling the permeability of the pore[60]. Most FG-NUPs are localized in the pore's central channel, yet some also contain structured domains important for interactions with other NUPs and can protrude towards cytoplasm or nucleoplasm[61].

Active transport through the nuclear pore requires several additional soluble factors: nuclear transport receptors (NTRs; importins and exportins of the karyopherin family), shuttling energy providing GTPase RAN, and additional recycling factors, nuclear transport factor 2 (NTF2) and cellular apoptosis susceptibility (CAS)[58]. Protein cargo to be imported into the nucleus carries a nuclear localization signal (NLS) recognized by the importins[62]. The cargo-importin-α-importin-β complex is translocated through the central channel of the NPC via interactions between the transport receptors and FG repeats of NUPs. Once in the nucleus, RAN·GTP binds to the transport complex causing the release of the cargo[63]. RAN·GTP-importin-β and RAN·GTP-importin-α-CAS are shuttled back into the cytoplasm and disassembled through GTP hydrolysis. Leftover RAN·GDP is then recycled back into the nucleus with the help of NTF2[64]. A similar energy-dependent shuttling mechanism is employed for exporting cargos into the cytoplasm. Exportin 1 (also known as CRM1) binds to the cargo containing nuclear export signal (NES) and this complex is exported in a RAN·GTP-dependent manner. Cargo is released in the cytoplasm upon GTP hydrolysis[58].

Specific details of the transport through the central pore channel and the precise organization of FG-NUPs are still unclear. It has been reported that NTRs form low-affinity transient interactions with FG-NUPs during transport[65], but how FG-NUPs are organized to form a selective transport barrier is still under debate. The key unresolved question giving rise to two opposing models is whether FG-NUPs form interactions between themselves. According to the 'virtual gating model', the affinity of FG repeats of each individual NUP for cargo binding

determines the chances for cargo transport, whereby FG-FG interactions are not involved in defining the permeability barrier[66]. An alternative 'selective phase model' relies on FG-FG interactions to form a meshwork which selectively transports cargos up to a certain size[67]. Such selectivity would according to this model be a result of phase separation within the central transport channel. Biological phase separation requires presence of scaffold proteins that create and retain the phase, and additional interacting proteins, which are able to enter the phase due to their affinity for binding sites of scaffold proteins[68]. It is conceivable that FG-NUPs in this scenario take the role of scaffold proteins interacting with one another forming a phase which different NTR-bound cargos can enter[58]. Several studies have reported such phase separation behavior *in vitro*. Purified FG repeats form FG hydrogels which enable fast entry of the NTR-cargo complexes but exclude other inert proteins. The hydrogel formation depends on weak cohesive hydrophobic interactions between FG motifs[69]. On the other hand, NTRs are the most hydrophobic soluble proteins in eukaryotic cells and can form such interactions with FG repeats and translocate into the phase within milliseconds[70]. In addition, seemingly inert substrates can be transformed to mimic transport speeds of the NTRs by increase of hydrophobic surface residues as well as histidine, cysteine, and arginine content[71]. Therefore, it is expected that the properties of the cargo itself will play a role in the translocation efficacy.

Another cargo feature relevant for transport is size. Small proteins up to ~30 kDa (or ~9 nm in diameter) can freely diffuse through the nuclear pore[72], while larger substrates require active transport via NTRs. Electron microscopy of differently sized gold particles coated with an NLS containing protein bound to importins revealed after microinjection into oocytes maximal particle size that can pass through the NPC to be 39 nm[73]. Transport of larger cargos across the nuclear envelope is reported in a couple of isolated cases. For example, the nucleocapsids of herpesviruses are assembled in the nucleus and are 120 nm in size, therefore too large for NPC transport, yet for complete viral assembly their export into the cytoplasm is necessary. The export is achieved through nuclear egress, which is initiated by local disassembly of the nuclear lamina through the action of viral kinase pUS3 and cellular kinase PKC. Next viral capsids are enclosed by a layer of INM and form vesicles that enter perinuclear space[74]. The release of the capsids into the cytoplasm requires vesicle fusion with the ONM. The exact molecular players of this process are still unknown; however, members of the AAA^+ ATPase family Torsins have been implicated in the process[75]. Another example is export of RNP granules from the nuclei of myocytes in neuro-muscular junctions of *D. melanogaster*. The neural stimulation of the muscle cell causes nuclear entry of a specific receptor which then binds ribonucleoprotein (RNP) granules containing RNAs encoding postsynaptic proteins[76]. The details of the export are unresolved, but involve a specific kinase which initiates lamina

dissolving, similar to the kinase of herpes viruses[77]. Finally, a recent study used correlative light and electron microscopy to show that HIV capsids of 60 nm diameter can be inserted into the NPC channel without fundamental changes in the NPC structure[78]. Taken together, most conventional cellular cargos can only pass through the NPC complex if they are below the 39 nm threshold.

1.4.2. Importance of eukaryotic nucleo-cytoplasmic compartmentalization

The evolution of the nuclear envelope and NPC-mediated transport allowed for physical separation of essential cell processes in eukaryotic cells. This includes messenger RNA (mRNA) synthesis and processing to be confined to the nucleus, whereas protein synthesis is confined to the cytoplasm[79]. This compartmentalization further allowed complex gene evolution with non-coding sequences, introns, which are transcribed but subsequently cut out of pre-mRNAs, generating a variety of different mRNA products coming from a single gene, and expanding the encoding potential of the eukaryotic genome[80]. The physical separation of unprocessed mRNAs from the protein synthesis machinery is thus essential in retaining eukaryotic cell homeostasis, as it provides a filter for RNA preselection before translation[81].

Although ribosomal subunits are synthesized in the nucleus, they are not fully assembled into mature ribosomes until they reach the cytoplasm (Fig. 1.3, adapted from [43]). The nuclear export of both 40S and 60S ribosomal subunits depends on CRM1 exportin and the Ran-GTPase system. CRM1 recognizes the NES on adaptor proteins, which bind ribosomal subunits and guide the entire complex through the NPC via interactions with FG-NUPs[82]. In yeast cells the adaptor protein for pre-60S export is Nmd3. The release of Nmd3 from 60S subunit happens once the complex arrives in the cytoplasm, with the help of several cytoplasmic proteins, among others ribosomal protein Rpl10[83]. The release of Nmd3 is coupled with the binding of Rpl10 to the 60S subunit, which might be one of the mechanisms to prevent ribosome maturation before nuclear export[84]. Mature ribosomes therefore lack adaptor proteins which could guide their transport through the NPC back into the nucleus and should remain in the cytoplasm for as long as they are translationally competent.

The tightly regulated exchange between the nucleus and the cytoplasm of interphase eukaryotic cells provides physical separation of cell processes. However, in higher eukaryotes the nuclear envelope border is lost upon mitotic entry.

1.5. Cell compartmentalization during mitosis

1.5.1. Mitotic entry

During division, cells of higher eukaryotes undergo extensive reorganization: the cell shape changes, chromatin compacts to form chromosomes, centrosomes separate and become seeding points for microtubule aster formation, and the nuclear envelope breaks down allowing mitotic spindle access to individual chromosomes. In addition, the localization and the number of most organelles changes to enable chromosome separation and accommodate the needs of newly forming daughter cells[85].

1.5.1.1. Cell rounding

Cell rounding during mitosis requires disassembly of focal adhesions, complexes which represent connection points between the actin cytoskeleton and the extracellular matrix[86]. This disassembly depends on inactivation of small GTPase Rap1 - cells with a constitutively active form of this protein maintain a flat morphology during mitosis[87]. The inhibition of rounding can further impair efficient capture of mitotic chromosomes by the spindle since the flattened surface spreads chromosomes further apart and out of reach for astral microtubules. Rounded mitotic cells retain contact with the substratum through thin actin fibers forming at the sites of previous focal adhesions[88]. The cell shape is supported by formation of a cortical actomyosin network which also serves as attachment site for centrosomal microtubule asters and aids establishment of cell polarity by organizing dynein rich polar zones[89].

1.5.1.2. NE disassembly and ER reorganization

During mitotic entry, animal cells disassemble their nuclear envelope and NPCs, which disrupts the permeability barrier between the nucleus and the cytoplasm. The release of nucleoporins into the cytoplasm begins with the hyperphosphorylation of NUP98, followed by other scaffold and FG-NUPs, executed by cyclin B-CDK1, PLK1 and NIMA-related kinases[90]. The removal of the NE membranes depends on breaking the interactions between the INM proteins and the nuclear lamina or chromatin[85]. CDK1 phosphorylation of extraluminal domains of INM proteins causes their dispersal into the ER. Lamina disassembly is also mediated by phosphorylation and includes the release of soluble A-type lamins into the cytoplasm, and retention of depolymerized B-type lamins as a part of the ER[91]. Further on, several changes in chromatin contribute to the detachment of the NE. Aurora B mediated phosphorylation of histone H3 at serine 10 causes chromatin detachment from heterochromatin protein 1 (HP1), which might contribute to the release of HP1- binding INM

protein LBR from chromatin[92,93]. During interphase, the barrier-to-autointegration factor (BAF) protein connects chromatin to the LEM domain proteins of the INM. Upon mitotic entry, BAF is phosphorylated by vaccinia-related kinase (VRK) and dissociated from chromatin, breaking the chromatin-NE link[94]. Failure to remove the NE from chromatin during mitotic entry impairs mitotic progression and leads to aberrant NE formation at the end of division[95].

In interphase cells, ER interactions with microtubules ensure ER spreading throughout the cell, while the NE contacts microtubules through LINC complexes[85]. In early prophase, NE invaginations which will aid NE fenestration are initiated by microtubule-dependent forces with the help of the minus-end-directed motor dynein[96]. After NEBD, ER interactions with microtubules are inhibited to ensure clearance of the ER from the mitotic spindle area. This is achieved through phosphorylation of two ER proteins, and via active removal by REEP3/4 protein. Depletion of REEP3/4 leads to ER membrane collapse onto the metaphase plate and causes chromosome segregation defects and aberrant nuclear morphology[97]. Whether mitotic ER is organized in the shape of sheets or elongated tubules remains an open question. Some studies in *Drosophila* even propose the formation of an ER membrane around the mitotic spindle which prevents the entry of other organelles into the spindle area[98].

1.5.1.3. Mitotic chromosome compaction

Maximal chromatin compaction is achieved in mitosis, when a cell forms mitotic chromosomes, compact rod-shaped bodies which pass on the genetic information to each daughter cell. Their specific shape is achieved through action of the mitotic subset of Smc proteins, condensin I and II[99]. However, condensins are not the only factor contributing to chromosome organziation. The acutely induced knock down of the common Smc2 subunit of both condensins, leads to the loss of chromosome shape, yet the relatively compact insoluble state of mitotic chromatin remains[100]. Therefore, the ability to compact is an inherent property of the mitotic chromatin polymer that is independent of the action of condensins. Based on *in vitro* findings, histone deacetylation and electrostatic interactions have been proposed as key regulators of this compaction.

The N-terminal tails of core histones are localized at the nucleosome surface, allowing them to be the substrate for posttranslational modifications such as acetylation. Histones are acetylated by histone acetyltransferases (HATs), enzymes which transfer the acetyl group from acetyl-coenzyme A (CoA) to the amino group of the lysine side chains located on histone tails. The p300 HAT deposits acetyl marks on all four core histone tails, as well as other substrates, such as other epigenetic enzymes and transcription factors[101]. Acetylated chromatin is mainly present in interphase, but when a cell starts compacting chromosomes

during mitotic entry most acetyl marks are removed from histones through the action of histone deacetylases (HDACs)[41,42]. Both HATs and HDACs are inactive during mitosis and displaced from mitotic chromosomes[102]. In early stages of telophase, in parallel to chromosomes decondensing, HATs again accumulate on chromatin where they deposit histone acetylation marks.

One of the most important HAT/HDAC substrates implicated in chromatin compaction is the tail of histone H4[103,104]. *In vitro* experiments with synthetic nucleosome arrays propose that this tail is involved in two types of chromatin compaction interactions. The first type are intra-array interactions occurring between the basic patch of the H4 tail and the acidic patch on the surface of the H2A-H2B dimer of the neighboring nucleosome[105]. Acetylation of H4K16 neutralizes the positive charge of the lysin side chain and putatively disrupts these interactions. The second type are inter-array interactions mainly mediated by electrostatic attraction between the H4 positively charged basic patch and DNA of other arrays[106]. These electrostatic H4 tail-DNA interactions may also be affected by acetylation, not only of specific H4K16, but also of other residues. For example, p300 recruitment to phase separated chromatin droplets in the presence of CoA leads to droplets dissolving[107]. The contribution of specific histone tails to mitotic chromosome compaction *in vivo* is still unknown. When altering the chromatin acetylation state *in vivo* most studies rely on the use of Trichostatin A (TSA), a potent global HDAC inhibitor, shown to cause chromosome decompaction and impair cell cycle progression[108].

Tight packaging of DNA also depends on neutralization of its negative charge and weakening of repulsive forces between DNA molecules. This is partially achieved through DNA wrapping around positively charged histone octamers. Electrostatic interactions between the H4 histone tail and DNA molecules of other nucleosome arrays cause *in vitro* aggregate formation[105], which may mimic chromatin compaction occurring during mitosis. However, the cellular context in which mitotic chromosome compaction occurs is rather complex. A release of ATP-bound Mg^{2+} during mitotic entry was reported as one of the factors contributing to mitotic chromosome formation[109]. Another recent publication showed that long-lived RNA molecules (such as repetitive LINE elements) interact with histones to neutralize their positive charge and maintain decompacted chromatin state[110]. A common pattern emerging from these reports is that the more positive charge is present on chromatin the more compaction can be achieved. The relevance of each of the mechanisms for chromosome formation during mitotic entry is still unclear.

1.5.1.4. The chromosome periphery

The chromosome periphery is a thick layer of proteins and RNAs derived mostly from nucleoli, which forms on the chromosome surface during mitotic entry. It occupies roughly a third of the mitotic chromosome volume, and it represents the difference in volume between prophase and metaphase chromosomes[111,112] (Fig. 1.5, adapted from,[112,113]). Components of the chromosome periphery include pre-rRNA, many ribosomal proteins, nucleolin, nucleophosmin, peripherin, Ki-67, as well as several chromosome periphery proteins identified through shotgun analysis of the mitotic chromosome proteome (cPERPs B, C, D and F)[114]. Although the details of chromosome periphery formation are still unclear, it has been shown that Ki-67 is the key molecular organizer, as all other components fail to localize to chromosome surface upon Ki-67 depletion[52].

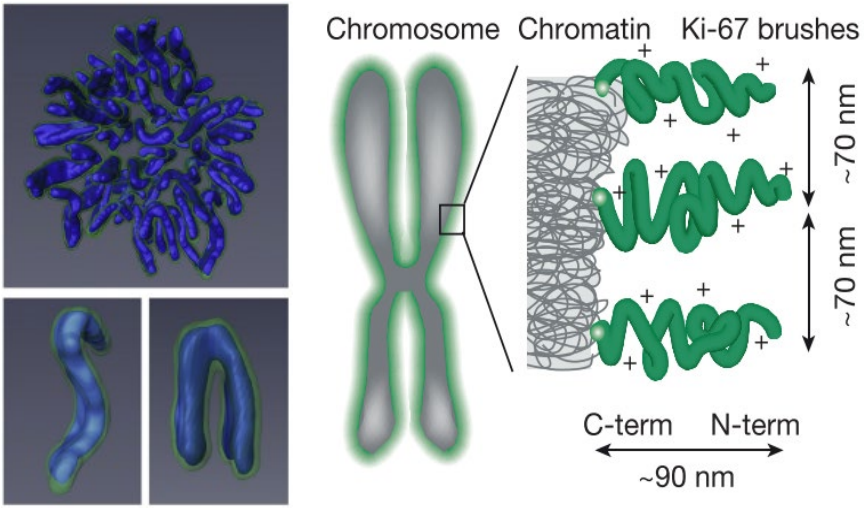

Figure 1.5. **Chromosome periphery organization**. Left: digital model obtained based on 3D-CLEM data. Blue represents naked chromosomes, green shows chromosome periphery. Adapted from [112]. Right: organization of positively charged Ki-67 molecular brushes on chromosome surface. Adapted from [113].

Ki-67 is a common proliferation marker used in cancer prognosis[115], and is conserved only in vertebrates, although it has been reported in mitotic cells of *Schistosoma mansoni*[116]. Ki-67 consists of a forkhead-associated (FHA) N-terminal domain, protein phosphatase 1 (PP1)-binding domain, large unstructured region consisting of 16 tandem repeats of 122 residues, and C-terminal leucine-arginine (LR)-rich DNA binding domain[117]. It binds to the surface of mitotic chromosomes and forms molecular brush-like structures which perpendicularly extend towards the cytoplasm and carry high positive charge (Fig. 1.5, adapted from [112,113]). The dense layer of ~210 Ki-67 molecules per μm^2 plays a key role in mitotic chromosome individualization[113]. Depletion of Ki-67 increases chromosome adhesion, decreases chromosome mobility, and leads to changes in the morphology of metaphase plate, although the intrinsic architecture of metaphase chromosomes remains the same[113,52]. Cells lacking Ki-67 can progress through mitosis, with a delay in anaphase onset. Ki-67's role in chromosome separation is not confined in neither of the specific domains. Series of truncation mutants showed that any part of Ki-67 can restore chromosome individuality as long as it contains the C-terminal DNA-binding domain. The chromosome separation can be re-established in the

absence of Ki-67 through overexpression of core histones, conceivably by mimicking the electrostatic interactions of highly positively charged Ki-67. Therefore, Ki-67 represents an electrostatic and steric barrier which enables chromosome dispersion, similar to surfactant molecules dispersing phase-separated liquid droplets in solvents[113].

Apart from its role in chromosomal dispersion, Ki-67 is necessary for layered organization of chromosome periphery. Ki-67 depletion leads to failure of proper localization of other chromosome periphery proteins, and their accumulation as foci in the cytoplasm, which commonly attach to one tip of the metaphase plate. Such foci often distribute unevenly between the daughter cells after mitosis, potentially causing defects in nucleolar reformation. Although the lack of Ki-67 does not affect the ultrastructure of reforming nucleoli, it causes a decrease in the number of nucleolar organizer regions (NOR) in newly forming cells[52]. This could be explained by the increased adhesion of chromosomes lacking periphery, which might cause fusion of NORs during reactivation. In addition, Ki-67 depleted cells are smaller, have decreased levels of rRNAs and transcription[52]. It is appealing to hypothesize that the displacement of nucleolar proteins from the periphery prevents their timely inclusion in reforming nuclei before nuclear envelope sealing, and leads to lack of material for nucleolar reorganization, and subsequent insufficient ribosomal synthesis. The precise role of the chromosome periphery in re-establishing nucleo-cytoplasmic compartmentalization remains an interesting unexplored question.

1.5.2. Mitotic exit

Once the spindle assembly checkpoint is satisfied, sister chromatids are moved by the mitotic spindle towards the opposite poles, where in telophase new daughter cell nuclei begin to form. Nuclear reformation includes the reversal of all processes occurring during mitotic entry: chromatin decondensation, nuclear envelope reformation and nuclear pore assembly.

1.5.2.1. Chromatin decompaction

Chromosomes become most compact in late anaphase, through condensin-independent axial shortening regulated by Aurora B kinase[118]. Subsequent chromosome decompaction has been suggested to involve active processes that depend on cellular energy in form of ATP and GTP[119]. For instance, removal of ubiquitinylated Aurora B from chromatin depends on ATP hydrolysis by AAA^{+}- ATPase VCP (valosin containing protein) in a complex with two other cofactors[120]. Further on, contact of nuclear membranes with chromosomes was implicated in aiding decondensation: a version of LBR protein lacking the chromatin binding domain caused

defects in nuclear envelope formation and chromatin decondensation[121]. Finally, histone modifications such as acetylation play a role in chromatin decondensation. Histone acetylase hALP which deposits acetyl marks on histones H2B and H4, is recruited by a member of the LINC complex, SUN1, to chromosomes in parallel to NE reformation[122]. Knockdown of SUN1 was shown to cause a delay in decondensation leading to apoptosis. Taken together, although several factors have been shown to contribute to chromosome decondensation at the end of mitosis, the exact mechanism and relative contribution of each factor still awaits clarification.

1.5.2.2. Nuclear envelope reformation

Proper enclosing of all chromosomes and formation of a single nucleus at the end of mitosis is essential for retaining genome integrity. Chromosomes are kept in proximity partially through the action of motor proteins while they move towards the cell poles. Timely inactivation of mitotic CDK1 is essential in temporal restriction of NE reformation to telophase[123]. In addition, BAF crosslinks distant parts of DNA in telophase to form a network surrounding the ensemble of anaphase chromosomes, thereby guiding nuclear membranes to form a single nuclear compartment in each daughter cell[124] (Fig. 1.6, adapted from [124]). In case individual chromosomes position far away from the chromosome ensemble, for example because of incorrect attachment and segregation, they can be enclosed by membranes to form separate micronuclei[2]. Micronuclei are prone to DNA damage, and may lead to genome instability in the following divisions[125].

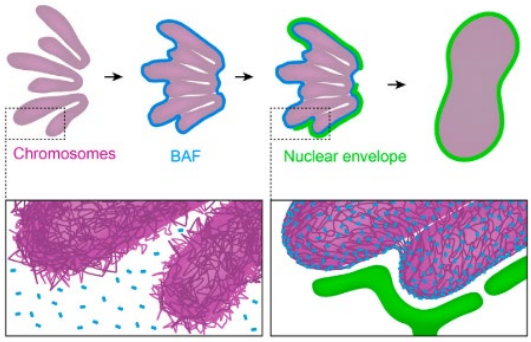

Figure 1.6. **BAF crosslinking guides nuclear envelope reformation**.
Adapted from [124].

The shape of ER membranes approaching the nuclear envelope is still under debate. One model proposes that ER tubules extend from the ER network, contact chromosomes and only then start flattening and expanding to form the INM and ONM[126]. Another model proposes that the ER approaches chromosomes in the form of flattened sheets which will then expand to seal the NE[127]. The two models are not mutually exclusive, considering that differences in ER structures were observed among different cell types. ER binding to chromatin during nuclear assembly is thought to be mediated by the integral proteins of the INM via contact to various chromatin components. LBR interacts with HP1[128], LEM-domain containing proteins contact the previously established BAF network[129], while several nucleoporins can directly contact the DNA[130].

Membrane recruitment to chromosomes is regulated through several mechanisms. Most INM proteins are phosphorylated by CDK1 during nuclear envelope break down (NEBD), and it is conceivable that this phosphorylation is reverted during NE reassembly, involving the phosphatase PP2A-B55alpha[131]. For example, the recruitment of LBR protein to anaphase chromosomes depends on its dephosphorylation. LBR interacts with HP1, whose recruitment to chromatin requires dephosphorylation of histone H3 at S10[132]. Further on, BAF dephosphorylation via PP2A phosphatase and parallel VRK1 inhibition are both necessary for BAF chromatin binding[133]. In addition to temporal regulation through phosphorylation/dephosphorylation cycles, the formation of NE must be physically restricted to chromatin. Mitotic chromosomes are demarcated by a GTPase RAN, which serves for cargo unloading from importins during interphase. It is possible that this RAN-importin interaction plays a role in recruitment of INM proteins to chromosomes during mitotic exit[123]. LBR is stably bound to importin β during mitosis, and is released from this inhibitory complex upon contact with RAN-GTP[134] (Fig. 1.7, adapted from [123]).

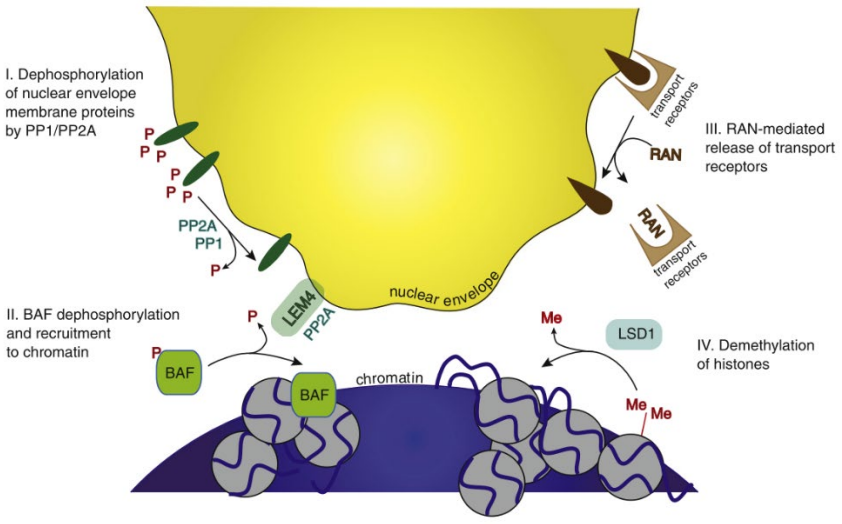

Figure 1.7. **Regulation of nuclear envelope recruitment to chromatin**. NE recruitment to chromatin depends on dephosphorylation of several INM and chromatin proteins, including BAF. The recruitment may be aided by RAN-mediated release of transport receptors and decrease in histone methylation. Adapted from [123].

Several proteins have been proposed to play a role in the final sealing of the NE patches, including SNARE receptors, membrane GTPases atlastins, and ESCRT-III (endosomal sorting complex required for transport)[123]. It has been shown that ESCRT-III recruits the ATPase involved in microtubule disassembly, which might contribute to subsequent NE sealing[135]. After NE sealing and import re-establishment, nuclear lamins undergo dephosphorylation and are enabled to reform the nuclear lamina, as the final step of NE reformation[136].

1.5.2.3. NPC reformation

During mitosis most of the NPC proteins are solubilized in the cytoplasm, very few core proteins reside within the ER[123]. Two models debate whether the NPC is inserted after NE sealing (insertion pathway)[127], or whether it is incorporated into the gaps between sheets of ER while the nuclear envelope is reforming (enclosure pathway)[137]. The first nucleoporin incorporated into the NE binds directly to chromatin and recruits scaffolding Nup107-160 complex[138]. This is followed by recruitment of proteins that establish early contacts between the NPC and the nuclear membranes[139]. Following these initial assembly steps, other NPC proteins are added, building firstly the inner pore and three membrane domain rings, and lastly the nuclear basket and cytoplasmic filaments. The two NPC assembly pathways are not mutually exclusive, it is proposed that the mechanism of assembly of NPCs during mitotic exit is different from the one during interphase[123]. The NPCs assembled during late mitosis are proposed to be incorporated through the enclosure pathway. A recent study used time resolved electron microscopy of HeLa cells to propose that NPC reformation occurs via dilation of core NPC components, which reside in the fenestrae of the ER[140]. The signals through which the NPCs would recognize their designated assembly sites may include curvature sensing ability of certain NUPs or signals from mitotic chromosomes, such as RanGTP levels, or presence of initial chromatin binding complexes[141]. In contrast, during interphase, the NPC incorporation is thought to occur through *de novo* fusion of INM and ONM at specific sites. Integration of NPC components in the insertion pathway would rely on the nuclear transport through pores previously established via enclosure during mitotic exit[142].

2 Open questions and aims of the thesis

The composition and organization of chromatin changes in mitosis to form compact chromosome bodies that can be efficiently moved by the mitotic spindle: cohesin is replaced with loop-forming condensins[99], Ki-67 organizes chromosome periphery and provides chromosome individualization[113], microtubules attach through newly organized kinetochore complexes, additional factors bind to ensure timely mitotic progression and NE reformation[123]. In addition to changing their interactome, chromosomes are exposed to a plethora of other cytoplasmic proteins, complexes, and organelles which they were previously shielded from by the nuclear envelope. Some of these organelles, such as mitochondria, lysosomes, and ER are kept away from mitotic chromosomes by the cytoskeleton, either by being tethered to cortical actin[143,144], actively removed by associated proteins[97], or potentially by a recently proposed spindle envelope[98]. However, many other organelles and macromolecular assemblies, such as ribosomes, are evenly distributed throughout the cytoplasm and come in contact with chromosomes[145]. How the diverse cytoplasmic components interact with mitotic chromosomes during open mitosis, i.e., whether they can enter chromatin or whether they are excluded from chromosomes, is not well understood.

At the end of open mitosis, the nuclear envelope is reformed directly on the surface of decondensing mitotic chromosomes[134]. Concomitantly, the nuclear pore complexes reassemble, and nuclear membrane transport is re-established. This allows reinforcing proper nucleo-cytoplasmic compartmentalization – nuclear proteins, which were not part of the chromosome periphery during mitosis, are actively re-imported through the nuclear pores, while any stray NES-containing cytoplasmic components are shuffled outside of the nucleus. However, the channels of nuclear pores can only accommodate transport of components up to 39 nm in size[73]. Series of classic experiments with inert dextran injections showed that large 40 kDa dextrans remain nuclear after being injected into the cell nucleus, but only until the next mitosis. After the nuclear envelope breaks down during mitotic entry, such dextrans are released into the cytoplasm where they homogenously distribute, yet they do not re-enter nuclei of the newly forming daughter cells[146]. This indicates that although these large molecules are unable to pass through the channels of nuclear pores, an additional mitosis-related mechanism prevents them from localizing within the newly formed nuclei. Which cell components play a role in the observed dextran exclusion from nuclei, what is the molecular mechanism behind the exclusion, and during which mitotic stages does it takes place is still unknown.

In this thesis I aim to define key regulators of cytoplasmic partitioning relative to mitotic chromatin during open mitosis (addressed in section 3.2, [147]) and understand how large

cytoplasmic components are excluded from the reforming nucleus at the end of mitosis (addressed in section 3.1, [148]).

3 Results

3.1. Chromosome clustering by Ki-67 excludes cytoplasm during nuclear assembly

Authors: Sara Cuylen-Haering*, **Mina Petrovic***, Alberto Hernandez Armendariz, Maximilian W.G. Schneider, Matthias Samwer, Claudia Blaukopf, Liam J. Holt and Daniel W. Gerlich

*these authors contributed equally to this work

Status: Published; Nature, pages 1-6, September 2020

My contributions:

-designed, performed, and analyzed all experiments investigating nucleo-cytoplasmic compartmentalization in unperturbed and spindle-less mitosis

-designed, performed and analyzed experiments addressing the role of actin, nuclear envelope transport and H3S10 phosphorylation, verified ribosome labelling, verified chromosome clustering in the presence of the spindle and in the absence of BAF

-contributed to manuscript writing and figure layout

Article

Chromosome clustering by Ki-67 excludes cytoplasm during nuclear assembly

https://doi.org/10.1038/s41586-020-2672-3

Received: 11 November 2019

Accepted: 8 June 2020

Published online: 2 September 2020

Check for updates

Sara Cuylen-Haering[1,2,5]✉, Mina Petrovic[1,5], Alberto Hernandez-Armendariz[2,3], Maximilian W. G. Schneider[1], Matthias Samwer[1], Claudia Blaukopf[1], Liam J. Holt[4] & Daniel W. Gerlich[1]✉

Gene expression in eukaryotes requires the effective separation of nuclear transcription and RNA processing from cytosolic translation[1]. This separation is achieved by the nuclear envelope, which controls the exchange of macromolecules through nuclear pores[2]. During mitosis, however, the nuclear envelope in animal and plant cells disassembles, allowing cytoplasmic and nuclear components to intermix[3]. When the nuclear envelope is reformed, cytoplasmic components are removed from the nucleus by receptor-mediated transport through nuclear pores[2]. These pores have a size limit of 39 nanometres[4–7], which raises the question of how larger cytoplasmic molecules are cleared from the nucleus. Here we show in HeLa cells that large cytoplasmic components are displaced before nuclear envelope assembly by the movement of chromosomes to a dense cluster. This clustering occurs when chromosomes approach the poles of anaphase spindles, and is mediated by a microtubule-independent mechanism that involves the surfactant-like protein Ki-67. Ki-67 forms repulsive molecular brushes during the early stages of mitosis[8], but during mitotic exit the brushes collapse and Ki-67 promotes chromosome clustering. We show that the exclusion of mature ribosomes from the nucleus after mitosis depends on Ki-67-regulated chromosome clustering. Thus, our study reveals that chromosome mechanics help to re-establish the compartmentalization of eukaryotic cells after open mitosis.

To investigate how large cytoplasmic components are excluded from the nucleus after mitosis, we used genetically encoded multimeric nanoparticles (GEMs) of 41-nm diameter[9]. We stably expressed the GEM subunit encapsulin tagged with eGFP (encapsulin–eGFP) in HeLa cells together with a chromatin reference marker, histone H2B fused to mCherry (H2B–mCherry), and observed high concentrations of GEMs in the cytoplasm but not in the nucleus of interphase cells (Fig. 1a). GEMs did not impair cell viability, proliferation or mitosis (Extended Data Fig. 1a–c) and are thus suitable for studying nucleo-cytoplasmic partitioning during mitosis in live cells.

Cytoplasm is excluded during nuclear assembly

To determine the localization of GEMs during nuclear breakdown and reassembly, we imaged cells progressing through mitosis. GEMs remained excluded from the nucleus during late prophase, but rapidly mixed with chromosomes after nuclear envelope breakdown (Fig. 1b, c). During anaphase, GEMs initially localized abundantly between chromosomes but were then progressively excluded as each set of sister chromatids segregated towards the spindle poles (Fig. 1d, e, Supplementary Video 1). Thus, GEMs and chromosomes mix during early mitosis but unmix during mitotic exit.

To examine how large endogenous cytoplasmic components are excluded from the reassembling nucleus, we visualized mature ribosomes in live HeLa cells using the ribosomal protein L10 tagged with eGFP (L10–eGFP)[10], which was efficiently incorporated into mature ribosomes and did not perturb cell proliferation or mitosis (Extended Data Fig. 1a–e). L10–eGFP localized abundantly between neighbouring chromosomes during early anaphase but was then excluded from the future nuclear space during late anaphase, with kinetics similar to those of GEMs (Fig. 1f, g, Supplementary Video 2). Thus, most mature ribosomes are excluded from chromosome regions shortly after the onset of anaphase.

To investigate how the exclusion of GEMs and mature ribosomes from anaphase chromosomes relates to the timing of nuclear envelope assembly, we determined when during mitotic exit transport through nuclear pores is initiated. Live-cell imaging of a nuclear import substrate—the importin β-binding (IBB) domain of importin α[11] fused to eGFP (IBB–eGFP)—revealed that this substrate accumulated in chromosome regions around six minutes after the onset of anaphase (Fig. 1h, i), whereas the exclusion of L10–eGFP was already almost complete five minutes after anaphase onset. Thus, GEMs and mature ribosomes are excluded from the reassembling nucleus before the formation of a transport-competent nuclear envelope.

[1]Institute of Molecular Biotechnology of the Austrian Academy of Sciences, Vienna BioCenter, Vienna, Austria. [2]Cell Biology and Biophysics Unit, European Molecular Biology Laboratory (EMBL), Heidelberg, Germany. [3]Collaboration for joint PhD degree between EMBL and Heidelberg University, Faculty of Biosciences, Heidelberg, Germany. [4]Institute for Systems Genetics, New York University Langone Health, New York, NY, USA. [5]These authors contributed equally: Sara Cuylen-Haering, Mina Petrovic. ✉e-mail: sara.cuylen-haering@embl.de; daniel.gerlich@imba.oeaw.ac.at

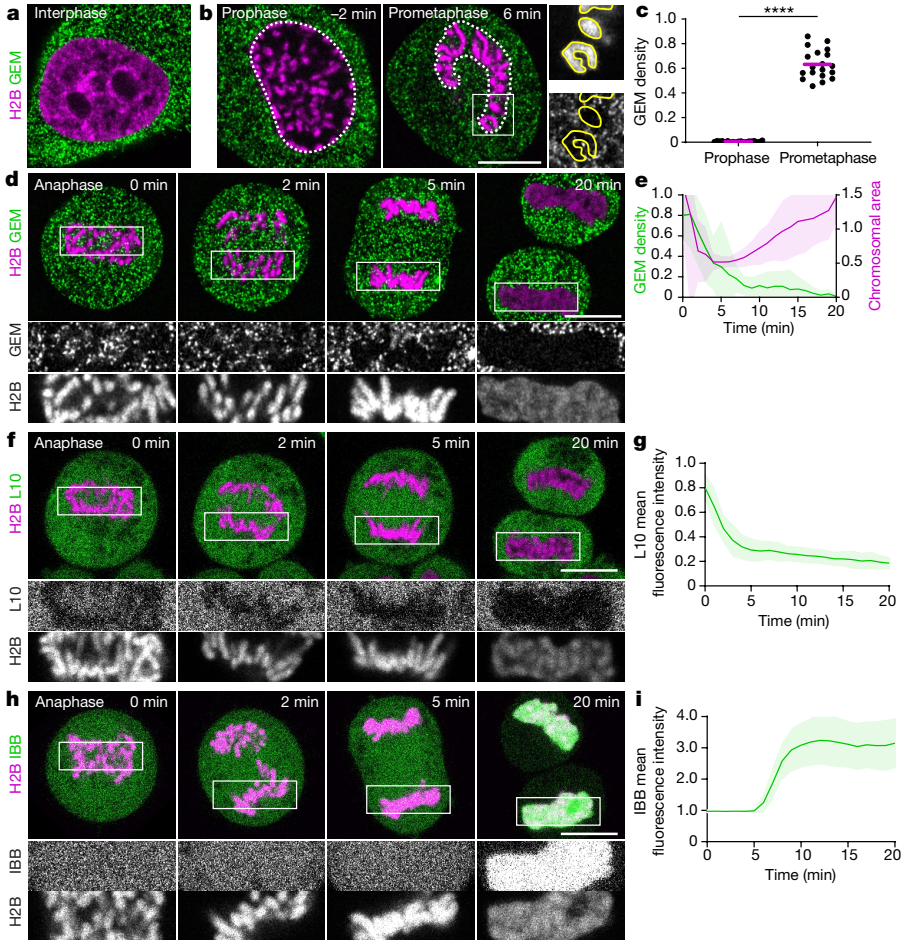

Fig. 1 | Cytoplasmic macromolecules are displaced from the nucleus before the assembly of a transport-competent nuclear envelope. a, **b**, Live HeLa cell expressing GEMs and H2B–mCherry in interphase (**a**) and time-lapse of early mitosis (**b**). White dashed lines represent chromosomal regions quantified in **c**, yellow lines outline individual chromosomes. **c**, GEM density (particles per chromosomal area/particles per cytoplasmic area) in chromosomal regions as in **b**, two minutes before (prophase) and six minutes after (prometaphase) nuclear envelope breakdown. Bars indicate mean; significance was tested by a two-sided ratio paired *t*-test (****$P = 3.6 \times 10^{-23}$). $n = 19$ cells. **d**, HeLa cell expressing GEMs and H2B–mCherry progressing through anaphase. **e**, Quantification of chromosomal area normalized to average of pre-anaphase time points and GEM density within this area, relative to surrounding cytoplasm, in anaphase cells as in **d**. $n = 22$ cells. **f**, HeLa cell expressing the mature ribosome marker L10–eGFP and H2B–mCherry progressing through anaphase. **g**, Quantification of L10–eGFP mean fluorescence intensity within the chromosomal region, normalized to surrounding cytoplasm, in anaphase cells as in **f**. $n = 30$ cells. **h**, HeLa cell expressing the nuclear import substrate IBB–eGFP and H2B–mCherry progressing through anaphase. **i**, Quantification of IBB–eGFP mean fluorescence intensity within the chromosomal region, normalized to pre-anaphase as in **h**. $n = 12$ cells. 0 min refers to anaphase onset in **d**–**i**, time lapse = 1 min. Lines and shaded areas (**e**, **g**, **i**) represent mean ± s.d. Single *z*-slices are shown. Scale bars, 10 µm.

The timing of the exclusion of L10–eGFP from the reassembling nucleus before the onset of transport through nuclear pores suggested that this exclusion should be independent of exportin-1, the transport receptor that mediates the export of pre-ribosomal subunits during biogenesis[12]. Consistent with this hypothesis, we found that the exclusion of L10–eGFP was unaffected by treatment with leptomycin B (Extended Data Fig. 2a, b), an exportin-1 inhibitor[13] (Extended Data Fig. 2c, d). Thus, the exclusion of ribosomes and other large cytoplasmic particles during nuclear assembly appears to be independent of nuclear-pore-mediated transport.

Chromosomes cluster during mitotic exit

The displacement of GEMs and mature ribosomes coincided with the movement of chromosomes to a dense cluster (Fig. 1d–g, Supplementary Videos 1, 2). We therefore hypothesized that nucleo-cytoplasmic compartmentalization might be controlled by the arrangement of chromosomes. Anaphase chromosomes are moved into proximity by spindle-mediated poleward pulling, but the very dense appearance of chromosome clusters in late anaphase suggested that additional spindle-independent mechanisms might be involved. To test for spindle-independent mechanisms of chromosome clustering, we established an assay for nuclear assembly in the absence of a spindle. We incubated mitotic cells in nocodazole to depolymerize microtubules and then acutely inhibited the mitotic kinase CDK1 using flavopiridol to promote mitotic exit in the absence of a spindle[14] (Extended Data Fig. 3a–d). Imaging of IBB–eGFP showed that IBB accumulated in chromosome regions around eight minutes after the addition of flavopiridol (Extended Data Fig. 3e, f), indicating that cells assemble a sealed and transport-competent nuclear envelope during mitotic exit in the absence of a spindle.

We next studied chromosome arrangements during spindle-less mitotic exit. Chromosomes were scattered in the cytoplasm at first, but after the induction of mitotic exit by flavopiridol they formed a single cluster (Fig. 2a). During clustering, the overall area of the chromosome ensemble and the area between neighbouring chromosomes

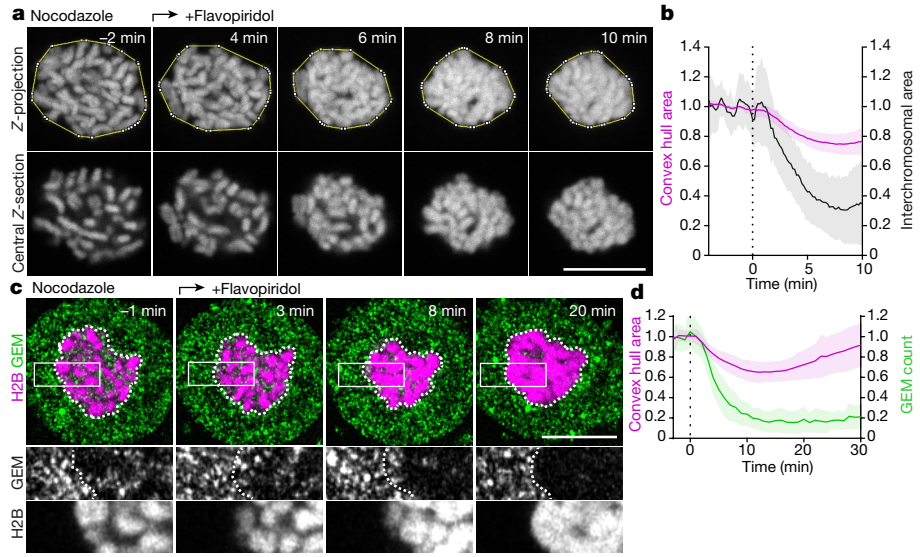

Fig. 2 | Displacement of cytoplasm by spindle-independent chromosome clustering. a, Chromosome organization during spindle-less mitotic exit. Three-dimensional (3D) video of a HeLa cell expressing H2B–mCherry imaged in the presence of nocodazole; flavopiridol was added (t = 0 min) to induce mitotic exit. Yellow lines indicate convex hulls around chromosomes. **b**, Quantification of convex hull area of 16 cells as in **a**, and interchromosomal area normalized to pre-flavopiridol time points. **c**, HeLa cell expressing GEMs and H2B–mCherry, during spindle-less mitotic exit as in **a**. Dashed lines indicate chromosomal area; single z-slices are shown. **d**, GEM particle count within chromosomal area as in **c** (green) and chromosome convex hull area (magenta), normalized to pre-flavopiridol time points. n = 35 cells. Lines and shaded areas (**b**, **d**) represent mean ± s.d.; dashed vertical lines indicate flavopiridol addition. Scale bars, 10 µm.

decreased, reaching a minimum area at around eight minutes—just before the onset of IBB–eGFP import (Extended Data Fig. 3e, f). An alternative procedure to induce mitotic exit using spindle assembly checkpoint inactivation also caused chromosome clustering in spindle-less cells (Extended Data Fig. 3g–i). Thus, chromosomes cluster through a microtubule-independent mechanism before nucleo-cytoplasmic compartmentalization is established by the nuclear envelope.

To investigate the relationship between chromosome clustering and cytoplasmic exclusion, we imaged GEMs during spindle-less mitotic exit. We found that GEMs were progressively excluded while chromosomes formed a cluster (Fig. 2c, d), before the onset of IBB–eGFP import (Extended Data Fig. 3e, f). Thus, the spindle is not required for chromosome clustering or nuclear exclusion of GEMs.

Chromosome clustering might be caused by increased attraction between neighbouring chromosomes or by forces generated by the surrounding cytoskeleton or membranes. Depolymerization of F-actin had no detectable effect on chromosome clustering and nuclear membranes contacted chromosomes only after they had clustered almost to completion (Extended Data Fig. 4a–d). Hence, chromosome clustering does not depend on actin filaments or spatial confinement by nuclear envelope membranes. To test whether clustering results from adhesion between neighbouring chromosomes, we tracked the mobility of individual chromosomes by stably expressing the kinetochore protein CENP-A fused to eGFP, and imaged mitotic cells in the presence of nocodazole. Tracking of CENP-A spots showed that chromosomes moved extensively relative to one another at first, but after the induction of mitotic exit by flavopiridol the clustered chromosomes were almost entirely immobilized (Extended Data Fig. 4e–h, Supplementary Video 3). This restricted chromosome motility is consistent with a model in which increased adhesion between chromosomes mediates clustering.

To test whether chromosomes also cluster in the presence of a spindle, we synchronized cells to metaphase using the proteasome inhibitor MG132 and then added flavopiridol to induce mitotic exit. Before the addition of flavopiridol, many chromosome arms extended from the metaphase plate, but shortly after adding flavopiridol, they formed a single compact cluster (Extended Data Fig. 5a, b). Clustered chromosomes remained aligned in the metaphase plate even when the spindle was subsequently disassembled by addition of nocodazole—in contrast to chromosomes of metaphase cells that were not pretreated with flavopiridol (Extended Data Fig. 5c, d). Thus, chromosomes become adhesive during mitotic exit, which results in the formation of a dense cluster.

Ki-67 regulates chromosome clustering

One candidate to regulate chromosome clustering is the protein barrier-to-autointegration factor (BAF), as it mechanically stabilizes anaphase chromosomes by cross-bridging the DNA of anaphase chromosome ensembles[15]. However, depletion of BAF by RNA interference had no detectable effect on chromosome clustering or GEM exclusion, and eGFP-tagged BAF accumulated on chromosomes after chromosome clustering was complete (Extended Data Fig. 6a–f). Chromosome clustering must therefore be regulated by factors other than BAF.

During prometaphase, chromosomes are kept apart by a repulsive surface formed by the protein Ki-67[8], which might be removed or inactivated during mitotic exit. To test whether chromosome clustering is due to the dissociation of Ki-67 from chromosomes, we imaged endogenously tagged eGFP–Ki-67. Ki-67 remained bound to chromosomes during clustering, both in spindle-less mitotic exit and regular anaphase (Extended Data Fig. 6g–j). Thus, chromosome clustering is not caused by Ki-67 dissociation.

Ki-67 forms molecular brushes at the surface of mitotic chromosomes during prometaphase, with the C terminus bound to the chromosome surface and the N terminus extended into the cytoplasm[8]. This type of molecular brush structure is characteristic of surface-active agents (surfactants) that disperse particles in solution by steric repulsion[16]. To test whether Ki-67 is inactivated during mitotic exit by a reorganization of its brush-like molecular arrangement, we determined the relative positions of the N and C termini of Ki-67 tagged with mCherry and eGFP, respectively[8] (Fig. 3a–d). In prometaphase, the Ki-67 N terminus localized 66 ± 27 nm (mean ± s.d.) towards the cytoplasm relative

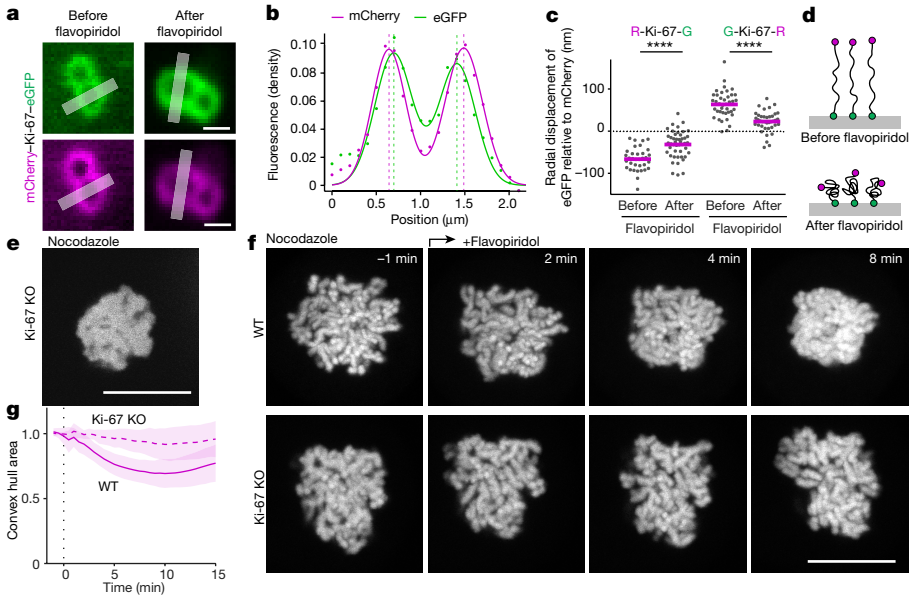

Fig. 3 | Ki-67 regulates chromosome clustering. a–**d**, Molecular organization of Ki-67 on the surface of mitotic chromosomes before and after flavopiridol addition. **a**, Ki-67 was tagged with mCherry on the N terminus and eGFP on the C terminus and expressed in HeLa cells. Sister chromatid pairs oriented perpendicular to the imaging plane were imaged in live mitotic cells. Lines indicate measurement regions for **b**. **b**, Relative positions of mCherry and eGFP along an axis perpendicular to the chromosome surface. Fluorescence densities (dots) were measured along line profiles as in **a** and a sum of two Gaussian functions (lines) was separately fitted to each of the eGFP and mCherry channels to determine peak positions (dashed lines). **c**, The radial displacement of eGFP relative to mCherry peaks was determined on the basis of line profile measurements as in **a**, **b** for mCherry–Ki-67–eGFP (R-Ki-67-G; $n = 34$ chromosomes before flavopiridol, $n = 46$ chromosomes after flavopiridol) and a construct in which the fluorophores were linked in reverse order, eGFP–Ki-67–mCherry (G-Ki-67-R; $n = 40$ chromosomes before flavopiridol, $n = 39$ chromosomes after flavopiridol). Bars indicate mean; significance was tested by a two-tailed unpaired *t*-test (R-Ki-67-G, $^{****}P = 2.3 \times 10^{-6}$; G-Ki-67-R, $^{****}P = 2.1 \times 10^{-8}$). **d**, Model of Ki-67 organization on chromosome surfaces during early mitosis and during mitotic exit. **e**, Ki-67-knockout (KO) cell expressing low levels of H2B–mNeonGreen. Representative example of 14 cells. **f**, Spindle-less mitotic exit in wild-type (WT) cells and in Ki-67-knockout cells that overexpress H2B–mNeonGreen to high levels to suppress the Ki-67-knockout individualization failure phenotype. Live cells were imaged in the presence of nocodazole; flavopiridol was added (time point (t) = 0 min) to induce mitotic exit. *Z*-projection. **g**, Normalized chromosome convex hull area of 24 wild-type and 22 Ki-67-knockout cells as in **f**. Lines and shaded areas represent mean ± s.d. Scale bars, 1 μm (**a**); 10 μm (**e**, **f**).

to its C terminus, whereas after inducing chromosome clustering by flavopiridol, the distance between the two fluorophores decreased to 32 ± 32 nm. A construct with inverted fluorophore positions yielded results consistent with this finding (Fig. 3c, d). Thus, the extended molecular brushes that are formed by Ki-67 during early mitosis collapse when chromosomes cluster during mitotic exit.

The collapse of the Ki-67 molecular brushes suggests an inactivation of the surfactant function of Ki-67, which might be sufficient to promote chromosome clustering. However, we also considered the possibility that Ki-67 actively contributes to chromosome clustering. To investigate this idea, we aimed to compare chromosome adhesion in wild-type cells and Ki-67-knockout cells. As Ki-67-knockout cells do not individualize chromosomes during early mitosis[8] (Fig. 3e), it is impossible to analyse their chromosome clustering during mitotic exit. Therefore, to evaluate the role of Ki-67 in clustering, we established conditions in which prometaphase chromosomes can form separate bodies in the absence of Ki-67. We previously showed that high-level overexpression of core histones restores chromosome separation in prometaphase cells that lack Ki-67, possibly through the addition of positive electrical charge[8]. Therefore, we imaged Ki-67-knockout cells[8] that overexpress H2B–mNeonGreen to sufficiently high levels for chromosome separation to occur. Upon mitotic exit, these cells completely failed to cluster chromosomes. By contrast, wild-type cells overexpressing similarly high levels of H2B–mNeonGreen still clustered chromosomes efficiently during mitotic exit (Fig. 3f, g), indicating that overexpression of H2B is not sufficient to prevent clustering. In addition, expression of transgenic eGFP–Ki-67 restored chromosome clustering in Ki-67-knockout cells that overexpress high levels of histones (Extended Data Fig. 7a–c). Thus, Ki-67 appears to promote chromosome clustering during mitotic exit—in contrast to its chromosome-repelling activity in prometaphase cells.

As the overexpression of H2B to high levels might have unknown side effects on chromosome organization, we established an alternative method to individualize chromosomes in Ki-67-knockout cells. Hypothesizing that electrical charge might be relevant[8], we tested the effect of global chromosome hyperacetylation resulting from the inhibition of histone deacetylases by trichostatin A[17], and indeed observed individualized chromosomes in Ki-67-knockout cells (Extended Data Fig. 7d–f). Treatment with flavopiridol induced chromosome clustering in trichostatin-A-treated wild-type cells, but not in Ki-67-knockout cells. Furthermore, expression of transgenic eGFP–Ki-67 restored chromosome clustering in Ki-67-knockout cells (Extended Data Fig. 7f, g). These observations provide further evidence that Ki-67 actively contributes to chromosome clustering during mitotic exit.

Ki-67 might promote chromosome clustering by recruiting protein phosphatase 1 (PP1) during anaphase[18]. However, mutating the Ki-67 RVSF motif—which is required for PP1 binding[18]—to RASA did not prevent chromosome clustering during mitotic exit (Extended Data Fig. 8a–d). Furthermore, mutant Ki-67(RASA) protein tagged by red and green fluorophores at opposite termini formed intact molecular brushes in prometaphase cells that collapsed during mitotic exit (Extended Data Fig. 8e). Moreover, Ki-67-knockout cells exhibited efficient dephosphorylation of serine 10 on histone 3 during mitotic exit (Extended Data Fig. 8f, g) and chromosome decondensation at normal rates (Extended Data Fig. 10d). Thus, Ki-67 promotes chromosome clustering through intrinsic properties rather than through recruitment of PP1.

Our model predicts that increasing surface adhesion should be sufficient to induce chromosome clustering. To test this hypothesis, we engineered a system to acutely increase adhesion between chromosomes. We therefore coexpressed H2B fused to either the FKBP protein or the FKBP rapamycin-binding domain (FRB) of mammalian target of rapamycin (mTOR), such that contacts between these chromosome-bound proteins can be chemically stabilized by the addition of rapamycin[19]. The expression of H2B–FRB and H2B–FKBP had no detectable effect on chromosome organization in prometaphase, but the addition of rapamycin caused clustering within a few minutes (Extended Data Fig. 9a–c, Supplementary Video 4). In control cells that express only H2B–FKBP, chromosome organization did not change after addition of rapamycin (Extended Data Fig. 9b, c, Supplementary Video 4), validating the specificity of the phenotype. Thus, increasing chromosome adhesion is sufficient to induce chromosome clustering, even in the absence of any other mitotic-exit-specific activities.

Chromosome clustering removes cytoplasm

Clustering-deficient Ki-67-knockout cells that overexpress high levels of histones enable us to investigate how chromosome clustering contributes to nucleo-cytoplasmic segregation. To first verify that cells that are deficient in chromosome clustering assemble a transport-competent nuclear envelope, we imaged the import substrate IBB–eGFP. We found that IBB–eGFP was efficiently imported after the induction of mitotic exit, with only a very slight delay compared to clustering-competent control cells (Extended Data Fig. 10a, b; compare with Extended Data Fig. 3e, f). Chromosome clustering is not therefore required for nucleo-cytoplasmic targeting through nuclear-pore-mediated transport.

To determine whether chromosome clustering is required for the exclusion of large cytoplasmic components during nuclear assembly, we first imaged GEMs. GEMs were not excluded from interchromosomal regions during mitotic exit in clustering-deficient Ki-67-knockout cells, in contrast to control cells that overexpress H2B–mCherry to similar levels (Fig. 4a–c, Extended Data Fig. 10c, d, Supplementary Video 5). Thus, suppression of chromosome clustering leads to contamination of the nucleus with large cytoplasmic components.

An analysis of L10–eGFP localization during mitotic exit in clustering-deficient cells revealed that ribosomes behave in a similar manner to GEMs. Clustering-proficient wild-type cells that overexpress H2B–mCherry efficiently excluded L10–eGFP from chromosome clusters during mitotic exit (Fig. 4d, f, Extended Data Fig. 10g, h), even when exportin-1 was inhibited by leptomycin B (Extended Data Fig. 10e, f). By contrast, L10–eGFP was not excluded from the reassembling nucleus in clustering-deficient Ki-67-knockout cells (Fig. 4e, f; Extended Data Fig. 10g, h). Thus, chromosome clustering is required for the exclusion of mature ribosomes from the nucleus.

Conclusions

Our study reveals that chromosome interactions during mitotic exit contribute to nucleo-cytoplasmic compartmentalization in vertebrate cells. Our data support a model in which chromosomes are first moved into proximity by the anaphase spindle and then tightly clustered by Ki-67-regulated surface adhesion, such that bulk cytoplasm is displaced before the nuclear envelope seals the nuclear compartment (Fig. 4g). Chromosome clustering prevents the contamination of the nucleus with soluble particles that are too large for export through nuclear pores, thus enabling the efficient separation of cytoplasmic and nuclear processes.

Our findings raise the question of how large components that need to be retargeted to the nucleus after mitosis avoid exclusion. Nuclear inclusion might be achieved by tight association with chromosomes. In line with this, many nucleolar proteins and pre-ribosomal RNAs remain associated with chromosomes throughout mitosis[20] in a dense peripheral layer that occupies almost half of the chromosome volume[21]. Nucleo-cytoplasmic compartmentalization might therefore involve an interplay between the retention of chromosome-associated factors and the exclusion of bulk cytoplasm.

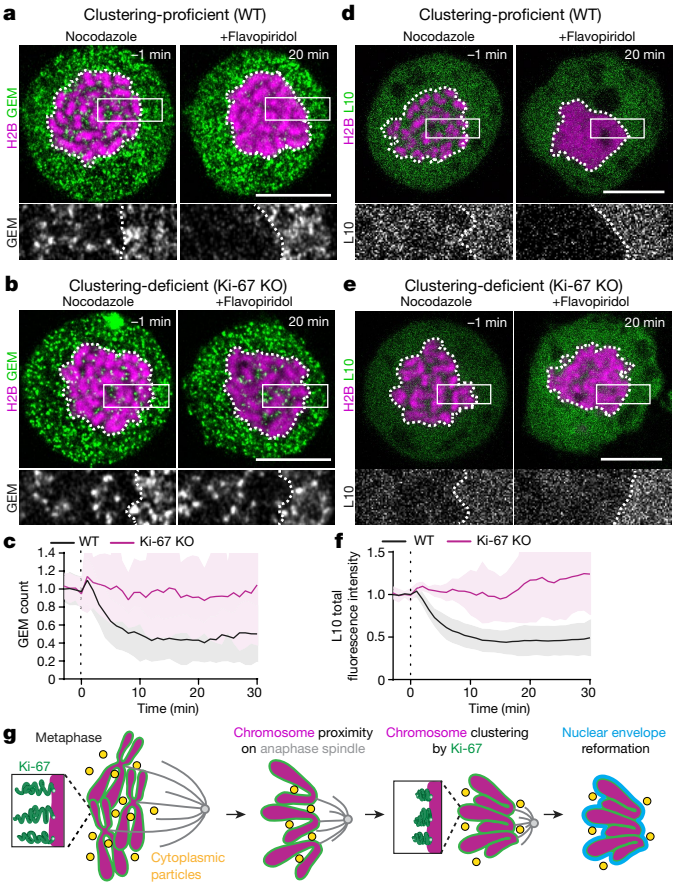

Fig. 4 | Ki-67-regulated chromosome clustering removes cytoplasm from the reassembling nucleus. a, **b**, Time-lapse microscopy of spindle-less mitotic exit in clustering-proficient wild-type HeLa cells (**a**) and clustering-deficient Ki-67-knockout HeLa cells (**b**). Cells stably expressed GEMs and transiently expressed H2B–mCherry; images show time point 1 minute before and 20 minutes after flavopiridol-induced mitotic exit in the presence of nocodazole. **c**, Quantification of GEM localization in 46 clustering-proficient wild-type and 29 clustering-deficient Ki-67-knockout cells as in **a**, **b**. Particle numbers were quantified within chromosomal area as in Fig. 2c, d. Analysed cells expressed H2B–mCherry at similar levels in both genetic backgrounds (Extended Data Fig. 10c). **d**, **e**, Time-lapse microscopy of clustering-proficient wild-type cells (**d**) and clustering-deficient Ki-67-knockout cells (**e**) that stably express L10–eGFP and transiently express H2B–mCherry, before and after the induction of mitotic exit in the presence of nocodazole. **f**, Quantification of L10–eGFP total fluorescence intensity within chromosomal area for the conditions shown in **d**, **e**. Analysed cells expressed H2B–mCherry at similar levels in both conditions (Extended Data Fig. 10g). $n = 23$ cells (wild-type); $n = 8$ cells (Ki-67-knockout). Individual Ki-67-knockout curves are shown in Supplementary Fig. 2. **g**, Model of nuclear assembly during mitotic exit. In **c**, **f**, lines and shaded areas represent mean ± s.d., dashed vertical lines indicate flavopiridol addition ($t = 0$ min) and data are normalized to average values before flavopiridol addition. Single *z*-slices are shown. Scale bars, 10 µm.

Online content

Any methods, additional references, Nature Research reporting summaries, source data, extended data, supplementary information, acknowledgements, peer review information; details of author contributions

and competing interests; and statements of data and code availability are available at https://doi.org/10.1038/s41586-020-2672-3.

1. Maniatis, T. & Reed, R. An extensive network of coupling among gene expression machines. *Nature* **416**, 499–506 (2002).
2. Görlich, D. & Kutay, U. Transport between the cell nucleus and the cytoplasm. *Annu. Rev. Cell Dev. Biol.* **15**, 607–660 (1999).
3. Ungricht, R. & Kutay, U. Mechanisms and functions of nuclear envelope remodelling. *Nat. Rev. Mol. Cell Biol.* **18**, 229–245 (2017).
4. Panté, N. & Kann, M. Nuclear pore complex is able to transport macromolecules with diameters of about 39 nm. *Mol. Biol. Cell* **13**, 425–434 (2002).
5. Bui, K. H. et al. Integrated structural analysis of the human nuclear pore complex scaffold. *Cell* **155**, 1233–1243 (2013).
6. Eibauer, M. et al. Structure and gating of the nuclear pore complex. *Nat. Commun.* **6**, 7532–7539 (2015).
7. Beck, M. & Hurt, E. The nuclear pore complex: understanding its function through structural insight. *Nat. Rev. Mol. Cell Biol.* **18**, 73–89 (2017).
8. Cuylen, S. et al. Ki-67 acts as a biological surfactant to disperse mitotic chromosomes. *Nature* **535**, 308–312 (2016).
9. Delarue, M. et al. mTORC1 controls phase separation and the biophysical properties of the cytoplasm by tuning crowding. *Cell* **174**, 338–3490 (2018).
10. Deryło, K. et al. The uL10 protein, a component of the ribosomal P-stalk, is released from the ribosome in nucleolar stress. *Biochim. Biophys. Acta Mol. Cell Res.* **1865**, 34–47 (2018).
11. Görlich, D., Henklein, P., Laskey, R. A. & Hartmann, E. A 41 amino acid motif in importin-α confers binding to importin-β and hence transit into the nucleus. *EMBO J.* **15**, 1810–1817 (1996).
12. Thomas, F. & Kutay, U. Biogenesis and nuclear export of ribosomal subunits in higher eukaryotes depend on the CRM1 export pathway. *J. Cell Sci.* **116**, 2409–2419 (2003).
13. Kudo, N. et al. Leptomycin B inactivates CRM1/exportin 1 by covalent modification at a cysteine residue in the central conserved region. *Proc. Natl Acad. Sci. USA* **96**, 9112–9117 (1999).
14. Potapova, T. A. et al. The reversibility of mitotic exit in vertebrate cells. *Nature* **440**, 954–958 (2006).
15. Samwer, M. et al. DNA cross-bridging shapes a single nucleus from a set of mitotic chromosomes. *Cell* **170**, 956–972 (2017).
16. Rosen, M. J. & Kunjappu, J. T. *Surfactants and Interfacial Phenomena* (John Wiley & Sons, 2012).
17. Cimini, D., Mattiuzzo, M., Torosantucci, L. & Degrassi, F. Histone hyperacetylation in mitosis prevents sister chromatid separation and produces chromosome segregation defects. *Mol. Biol. Cell* **14**, 3821–3833 (2003).
18. Booth, D. G. et al. Ki-67 is a PP1-interacting protein that organises the mitotic chromosome periphery. *eLife* **3**, e01641 (2014).
19. Rivera, V. M. et al. A humanized system for pharmacologic control of gene expression. *Nat. Med.* **2**, 1028–1032 (1996).
20. Gautier, T., Robert-Nicoud, M., Guilly, M. N. & Hernandez-Verdun, D. Relocation of nucleolar proteins around chromosomes at mitosis. A study by confocal laser scanning microscopy. *J. Cell Sci.* **102**, 729–737 (1992).
21. Booth, D. G. et al. 3D-CLEM reveals that a major portion of mitotic chromosomes is not chromatin. *Mol. Cell* **64**, 790–802 (2016).

Methods

Cell lines and cell culture

All of the cell lines used in this study have been regularly verified as negative for mycoplasm contamination. Their sources and authentication are summarized in Supplementary Table 1. All HeLa cell lines were derived from a HeLa 'Kyoto' cell line that has been previously described[22]. Cells were cultured in Dulbecco's modified medium (DMEM; Sigma-Aldrich, D5648) containing 10% (v/v) fetal bovine serum (FBS; Gibco, 10270), 1% (v/v) penicillin–streptomycin (Sigma-Aldrich), 1% (v/v) GlutaMAX (Gibco; 35050038) and selected antibiotics according to the expression constructs: blasticidin (6 μg ml^{-1}, Thermo Fisher Scientific), puromycin (0.5 μg ml^{-1}, Calbiochem), hygromycin B (0.3 mg ml^{-1}, Roche) and G418 (1 mg ml^{-1}, Invitrogen). Chromatin visualization was achieved through stable (Figs. 1, 2, Extended Data Figs. 2–5, 6a–f, 7a, b) or transient (Figs. 3e–g, 4, Extended Data Fig. 10) expression of histone H2B labelled with mCherry, mRFP or mNeonGreen or alternatively by labelling with 100 nM SiR-Hoechst[23] (Extended Data Figs. 6g–j, 7f, g, 8c, d) or with Hoechst 33342 (1 μg ml^{-1}, Invitrogen) (Extended Data Fig. 8f, g). All cytoplasmic markers were visualized through stable expression of eGFP-fused constructs, except for GFP–NES (Extended Data Fig. 2c, d), which was transiently transfected into cells. Live-cell imaging was performed in DMEM containing 10% (v/v) FBS, 1% (v/v) penicillin–streptomycin and 1% (v/v) GlutaMAX (Gibco, 35050038) but omitting riboflavin and phenol red to reduce autofluorescence[22]. Cells were grown in plastic-bottom 96-well plates (μClear; Greiner Bio-One), on LabTek chambered coverglass (Thermo Fisher Scientific), or in 8-well glass bottom μ-slides (Ibidi).

Generation of stable cell lines

For generation of cell lines that stably express fluorescently labelled marker proteins, we used random plasmid integration (for transfection conditions see below) or a lentiviral vector system pseudotyped with a mouse ecotropic envelope that is rodent-restricted (RIEP receptor system). Construction of RIEP receptor parental cell lines and subsequent generation of stable cell lines that express fluorescent marker proteins was performed as described previously[15]. Genome editing was performed using a CRISPR–Cas9 nickase strategy. Single-guide RNAs (sgRNAs) were cloned into pSPCas9n(BB)-2A-GFP (pX461, Zhang laboratory[24]). For mutation of the PP1-binding motif RVSF to RASA in Ki-67, a repair template with 750-bp homology flanks on each site was designed (see scheme in Extended Data Fig. 8a). The repair template contained an additional silent mutation at the protospacer adjacent motif (PAM) site of one of the two sgRNAs and was cloned in plasmid pCR2.1 (Life Technologies). The plasmid mix of guide RNA plasmids and the repair template was transfected into HeLa cells using X-tremeGENE 9 DNA transfection reagent (Roche). Two days after transfection cells were sorted for the presence of Cas9 (GFP-positive) and another six days later for the absence of Cas9 (GFP-negative) using fluorescence-activated cell sorting (FACS) into 96-well plates. Genotyping was performed as in a previous study[15].

Plasmid and small interfering RNA transfections

For both transient and stable expression of fluorescently labelled markers, the genes were cloned into IRES vectors with antibiotic resistance genes that allow the protein of interest and the resistance gene to be expressed from the same transcript (see Supplementary Table 2). For transient expression, plasmids were transfected using X-tremeGENE 9 DNA transfection reagent (Roche) following the manufacturer's instructions or PEI transfection reagent (1 mg ml^{-1} stock, Polysciences, 4 μg of transfection reagent per 1 μg of plasmid) with a 48-h incubation before imaging. DNA amounts were optimized for each assay and varied between 0.25 μg and 2 μg per 3 μl transfection reagent and 100 μl Opti-MEM. For stable expression, plasmids were transfected using PEI transfection, and incubated for 48 h before antibiotic selection.

Small interfering RNAs (siRNAs) were delivered with lipofectamine RNAiMax (Invitrogen) according to the manufacturer's instructions. *BAF* (also known as *BANF1*) was targeted using 18 nM s16808 (AGAUUGCUAUUGUCGUACUtt, Thermo Fisher Silencer Select, including a 3′ overhanging tt dinucleotide for increased efficiency) and analysed after 72 h; XWNeg9 (UACGACCGGUCUAUCGUAGtt, Thermo Fisher Silencer Select, custom, including a 3′ overhanging tt dinucleotide for increased efficiency) was used as a non-targeting siRNA control. *MAD2* (also known as *MAD2L1*) was targeted by 10 nM siRNA with the target sequence AAGAGTCGGGACCACAGTTTA (custom siRNA, Qiagen) for 28 h.

Inhibitors and stains

To arrest cells in prometaphase, cells were incubated for 2–4 h in 200 ng ml^{-1} nocodazole (Sigma-Aldrich). Acute spindle depolymerization was induced with 3 μg ml^{-1} nocodazole. To arrest cells in metaphase, cells were incubated for 30 min in 10 μM MG132 (Sigma-Aldrich). Mitotic exit was induced by the addition of flavopiridol (Tocris Bioscience) to a final concentration of 20 μM, or reversine (Sigma-Aldrich) to a final concentration of 1 μM. Exportin-1 (CRM1) was inhibited by a 2-h incubation in leptomycin B (Sigma-Aldrich); final concentration 1 μg ml^{-1}. Actin was depolymerized by a 2-h incubation in 1 μM latrunculin B (Sigma-Aldrich). For viability measurements TO-PRO-3 iodide (Molecular Probes) was used at a final concentration of 1 μM. Rapamycin (Calbiochem 5S3210) was used at a final concentration of 500 nM. Trichostatin A (TSA) (Sigma-Aldrich, T8552) was added 2 h before imaging at a final concentration of 0.5 μM.

Western blotting

Ribosome samples were separated on NuPage 4–12% gradient Bis–Tris gels (Invitrogen), and transferred to a nitrocellulose membrane (Bio-Rad) by wet blotting. Fluorescently labelled RPL10 was probed by a monoclonal mouse anti-RPL10 antibody (Thermo Fisher Scientific, MA526901, 1:2,000). H2B was probed by a polyclonal anti-H2B antibody (Abcam, ab1790). Horseradish peroxidase-conjugated anti-mouse or anti-rabbit secondary antibodies (Bio-Rad, 1:5,000) were visualized using ECL Plus Western Blotting Substrate (Thermo Fisher Scientific) on a Bio-Rad ChemiDoc Imager. BAF-depleted samples were immunoblotted as previously described[15].

Ribosome fractionation

A total of 50 million cells stably expressing eGFP-tagged ribosomal protein L10 were lysed for 5 min on ice (lysis buffer: 15 mM HEPES, 6 mM $MgCl_2$, 300 mM NaCl, 0.5% NP40 with one tablet of mini cOmplete protease inhibitor (Roche) and 40 U μl^{-1} RNaseOUT (Thermo Fisher Scientific)). A 200-μl sample of the lysate was separated on a 10–50% sucrose gradient via ultracentrifugation at 35,000*g* for 2.5 h at 4 °C (SW 40 Ti rotor) and then fractionated into 40 fractions using a customized fraction collector. Ribosome fractions were precipitated using 100% (w/v) trichloroacetic acid at 4 °C overnight. The precipitate was washed twice in cold acetone and dissolved in 2× SDS loading buffer. Fractions that specifically correspond to peaks of absorbance were blotted (as indicated with dashed lines in Extended Data Fig. 1d).

Live-cell microscopy

Cell proliferation, mitotic duration and apoptotic index was scored in images recorded with an ImageXpressMicro XL screening microscope (Molecular Devices) using a ×10, 0.5 NA S Fluor dry objective (Nikon), operated by in-house developed Metamorph macros. Time-lapse imaging was performed on a customized confocal Zeiss LSM780 microscope, using ×40 or ×63, 1.4 NA Oil DIC Plan–Apochromat objective (Zeiss), operated by ZEN 2011 software. Time-lapse videos with GEM particle counts (Figs. 1a–e, 2c, d, 4a–c, Extended Data Fig. 6a–c, Supplementary Videos 1, 5) were in addition recorded on an Airyscan confocal Zeiss LSM880 microscope, using a ×63, 1.4 NA Oil DIC Plan–Apochromat

objective (Zeiss) combined with the Airyscan detector, operated by ZEN 2011. Datasets from both microscopes were combined in Figs. 2d, 4c, Extended Data Fig. 6b, c. For all confocal microscopes, an incubator chamber (EMBL) provided a humidified atmosphere and a constant 37 °C temperature with 5% CO_2.

Immunofluorescence

Dephosphorylation kinetics in Extended Data Fig. 3a–d were quantified by imaging live single-cell unperturbed and spindle-less mitosis, and retrieving positions after fixation and staining. Dephosphorylation kinetics in Extended Data Fig. 8f–g were quantified by imaging fields of cells fixed after the indicated time relative to flavopiridol addition. To enrich for prometaphase arrested cells, a 2-h nocodazole incubation was performed in flasks and then mitotic cells were collected by shake-off and reseeded into imaging dishes in nocodazole. To reduce variability caused by background noise, cells from both genetic backgrounds were mixed and seeded together. Wild-type cells were distinguished from Ki-67-knockout cells by an eGFP-labelled membrane myristylation-palmitoylation marker (more than 97% of cells expressed the marker in the wild-type cell population). The levels of acetylated H3 in Extended Data Fig. 7d, e were quantified from cells fixed after 2 h of nocodazole or nocodazole/TSA incubation in imaging dishes.

In all immunofluorescence experiments cells were fixed with 4% formaldehyde (Thermo Fisher Scientific) in PTEM buffer (50 mM PIPES (Sigma-Aldrich) pH 6.8, 10 mM EGTA (Sigma-Aldrich), 1 mM MgCl2, 0.2% Triton X-100 (Sigma-Aldrich)) for 5 min. The fixation reaction was quenched with 10 mM Tris in phosphate-buffered saline (PBS), washed again with PBS and blocked in 2% BSA (Sigma-Aldrich) in PBS for 1 h. H3 phosphorylated at serine 10 (H3(pS10)) was probed using a monoclonal mouse antibody (Millipore, 05-806, 1:5,000) and visualized using a goat anti-mouse Alexa Fluor 488 secondary antibody (Molecular Probes, A11001, 1:1,000) (Extended Data Fig. 3a–d) or a goat anti-mouse Alexa Fluor 568 secondary antibody (Molecular Probes, A11004. 1:1,000) (Extended Data Fig. 8f, g). Acetylated H3 was probed using a rabbit polyclonal antibody (Millipore, 06-599, 1:200) and visualized using a goat anti-rabbit Alexa Fluor 594 secondary antibody (Molecular Probes, A-11037, 1:500) (Extended Data Fig. 7d, e).

Image analysis

Cell viability, proliferation and mitotic duration. To quantify cell viability, the number of live cells (negative for TO-PRO-3 iodide) was manually counted. Cell proliferation was measured as the fold change in the number of live cells within 24 h. Mitotic duration from prophase to anaphase onset was determined on the basis of manual identification of corresponding chromatin morphologies during the course of a video.

Chromosomal area measurements by active contours. In Fig. 1d, e, the chromosomal area was measured in a central *z*-section (9 *z*-sections recorded with 1-µm spacing; section selected on the basis of a visual inspection). The chromatin channel was denoised using a Gaussian blur filter ($\sigma = 2$) and thresholded using the Huang method in ImageJ[25]. Next, the ensemble chromatin mass was converted to a region of interest (ROI) by using the 'Analyze Particles' function in Fiji. An ellipse was fitted to each ROI using the build in 'Fit Ellipse' function in ImageJ and enlarged by 2 µm. The ellipses surrounding chromatin masses were then used as seeding points for applying the 'Level sets' plug-in in ImageJ using the active contours method. Acquired ROIs were then additionally shrunk by 0.8 µm using the 'Enlarge' function in ImageJ. At anaphase onset, one of the two ensembles of chromosomes was randomly selected for measurements. All data points were normalized to the average area of all values before anaphase onset.

Quantifications of cytoplasmic probes. In Fig. 1b, c, ROIs were drawn manually around the nucleus (−2 min before nuclear envelope breakdown (NEBD); prophase) and the entire set of chromosomes (6 min after NEBD; prometaphase) in manually determined central *z*-sections (5 *z*-sections recorded with 1.5-µm spacing). The number of GEM particles within ROIs was determined using the 'Find Maxima' function in ImageJ. The GEM density (number of particles per area) within the ROI was normalized to the GEM density within an arbitrary cytoplasmic region.

In Fig. 1d, e, chromosomal ROIs were determined by active contour area measurements (see above). For normalization, cytoplasmic ROIs were generated by subtracting the chromosomal ROI from a 3-µm enlarged chromosomal ROI (using the 'Enlarge' in ImageJ) to yield a rim ROI around the chromosome ensemble. The number of GEM particles was measured as described above.

In Fig. 1f–i and Extended Data Fig. 2a–d, the central *z*-section was determined using a custom ImageJ script that tracks 3D segmented chromatin mass for each time point and extracts the slice with the largest chromatin area in xy. Chromosomal ROIs were determined by active contour area measurements (see above) and IBB, L10 or NES mean fluorescence intensity was measured within these ROIs. Background signal in a circular ROI outside the cell was subtracted and values were normalized to mean fluorescence intensity in cytoplasmic regions measured in a rim ROI around the chromosome ensemble (Fig. 1f, g, Extended Data Fig. 2a, b; see above) or to pre-anaphase frames (Fig. 1h, i, Extended Data Fig. 2c, d).

In Figs. 2, 4 and Extended Data Figs. 6a–c, 10a, b, the central *z*-slice was determined using a custom ImageJ script described above (9 *z*-sections recorded with 1.5-µm spacing). Chromosomal ROIs were determined by active contour area measurements (see above), except that instead of an ellipse, a circle was fitted to the thresholded chromatin, using the 'Fit Circle' function in ImageJ. The total background fluorescence subtracted was determined as a product of mean fluorescence intensity outside of the cell and the active contour area within the cell. Measured fluorescence intensities and particle counts were normalized to the average fluorescence intensity and particle counts before flavopiridol addition.

At anaphase onset, one of the two chromosome ensembles was randomly selected for quantification. When using 'Level sets' or 'Find maxima' functions in Fiji, the parameters were adjusted by visual determination in one cell and applied to all cells within the experiment. Normalizations were calculated using Microsoft Excel and graphs were generated in GraphPad Prism.

Chromosome convex hull area measurements. Chromosomal area was segmented in maximum intensity *z*-projections of H2B–mCherry or SiR-Hoechst images (5-9 *z*-sections with 0.5–1.5 µm spacing), except in Extended Data Fig. 5, in which the segmentation was obtained in single central *z*-slice determined using a custom ImageJ script described above. If substantial bleaching was observed, a bleach correction by frame-wise exponential fitting using the Image J plug-in 'Bleach correction' (http://fiji.sc/Bleach_Correction) was performed before segmentation. The (bleach-corrected) maximum intensity projection was denoised using a Gaussian blur filter ($\sigma = 2$), then thresholded using ImageJ's default automated method (a variation of the IsoData algorithm) or the Otsu threshold and converted to a binary image. To calculate the area occupied by chromosomes, a convex hull algorithm (Convex hull plus plug-in for Fiji; https://blog.bham.ac.uk/intellimic/g-landini-software/) was applied to the resulting binary image. All data points were normalized to the average chromosome convex hull area before flavopiridol addition for each cell.

Interchromosomal space analysis. The interchromosomal space analysis was performed on a single *z*-section. The *z*-section with the highest H2B fluorescence intensity corresponded to the centre section and was automatically extracted by a custom ImageJ script. Chromosomes were then segmented and convex hull analysis was performed as described above. Next, the area of the segmented chromosomes was calculated using the build in 'Analyze Particles' function in Fiji. All areas

of segmented chromosomes per time point were summed up using a custom R script and subtracted from the convex hull (see above) area to yield the interchromosomal space. All data points were normalized to the average interchromosomal space of all values before flavopiridol addition for each cell using R.

Histone fluorescence intensity measurements. Histone fluorescence was quantified 3 min before flavopiridol addition. For this, the convex hull area around chromosomes was determined in average intensity projections of H2B–mCherry images (9 *z*-sections with 1.5-µm spacing) as described above. The resulting ROI was applied to the average projection image of H2B–mCherry and the total fluorescence intensity was measured within this ROI. Measurements from all experimental conditions were normalized to the mean of all cell measurements in the wild-type background using Microsoft Excel.

H3(pS10) and acetylated H3 fluorescence intensity measurements. The mean fluorescence intensity of H3(pS10) was measured within a mask obtained by thresholding the chromatin channel using the Huang method in ImageJ[25]. Background signal was subtracted by measuring a circular ROI outside of cell. Acetylated H3 mean fluorescence intensity was measured in maximum projections using a primary segmentation mask in the chromatin channel defined by local adaptive threshold using CellCognition Explorer[26]. The primary mask was dilated by 5 pixels and used for intensity measurement in the acetylated H3 (Alexa Fluor 594) channel.

Quantification of LAP2β and BAF in a rim around the ensemble of chromosomes. Quantification of LAP2β was performed in Fiji on a single central *z*-section that was manually chosen for each cell (6 *z*-sections with 2-µm spacing recorded). First, to segment the ensemble of chromosomes a Gaussian blur filter ($\sigma = 2$) was applied to the H2B–mRFP fluorescence, the image was thresholded using ImageJ's default method (a variation of the IsoData algorithm) or the Otsu threshold, converted to a binary image and the 'Fill Holes' operation performed. If substantial bleaching was observed, a bleach correction by frame-wise exponential fitting using the Image J plug-in 'Bleach correction' (http://fiji.sc/Bleach_Correction) was performed. Next, the ensemble chromatin mass was converted to a ROI by using the 'Analyze Particles' function in Fiji. To generate a ROI that constitutes a rim around the ensemble chromatin mass, a 10-pixel shrunk ROI was subtracted from a 10-pixel enlarged ROI (1 pixel = 83 nm). The resulting rim ROI was transferred to the eGFP channel and the LAP2β–GFP signal inside this ROI was measured. For measuring eGFP–BAF enrichment, the ROI around the ensemble chromatin mass was generated as above except with 15-pixel shrunk and 5-pixel enlarged ROIs. Background signal was subtracted by measuring a rectangle ROI outside the cell. Using R, the signals were normalized to the mean value measured before flavopiridol addition for each cell.

Quantification of Ki-67 levels on chromosomes. Quantification of eGFP–Ki-67 fluorescence in flavopiridol-induced mitotic exit (Extended Data Fig. 6i, j) was performed in Fiji on a maximum projection of 6 slices with 1.5-µm spacing. Chromosome convex hull area was calculated as described above, added to the ROI manager and the ROI was transferred to the eGFP signal to measure eGFP–Ki-67 inside the convex hull. Using R, the signals were normalized to the mean value measured before flavopiridol addition for each cell.

For quantification of Ki-67 during the metaphase-to-anaphase transition (Extended Data Fig. 6g, h), cells expressing Ki-67–eGFP were automatically imaged and subsequently analysed using CellCognition Explorer[26] as follows. A supervised machine learning program was used to systematically search low-resolution images online for metaphase cells, return the position to an Autofocuscreen macro (Autofocuscreen, https://www-ellenberg.embl.de/resources/microscopyautomation, provided by the Ellenberg laboratory (EMBL)) and trigger the acquisition of a high-resolution time-lapse recording with a 1-min timelapse and 5 *z*-slices (2-µm spacing). For the intensity measurements in the maximum projection of the eGFP channel, a primary segmentation mask in the chromatin channel was defined by applying a local adaptive threshold using CellCognition Explorer. This primary mask was dilated by 6 pixels and used for intensity measurements in the eGFP channel. For tracking the chromosome ensembles over time, a nearest-neighbour tracking approach that also recognized split and merge events of cell trajectories was used. Trajectories that did not contain a split event or that contained a split event caused by segmentation errors or linking errors caused by the tracking algorithm were excluded from the analysis. Using R, the signals were normalized to the mean value measured before anaphase onset for each cell.

Kinetochore tracking. Three-dimensional confocal time-lapse images with 9 *z*-sections with a spacing of 500 nm were recorded every 10 s and Fiji (ImageJ 1.47m) was used for the following bleaching and movement corrections. After a maximum intensity projection of all *z*-sections, a bleach correction by exponential fitting using the 'Bleach Correction' plug-in (http://fiji.sc/Bleach_Correction) was performed. Kinetochore videos were registered using the 'StackReg' Fiji plug-in[27] to correct for translation and rotation of the entire set of chromosomes (rigid body transformation). Kinetochore spot detection and tracking was performed using Imaris software (Bitplane) with the following parameters: Brownian motion, maximal distance 0.8 µm, maximal gap size 2, track length >5 frames. Data from Imaris were imported into MATLAB using a custom MATLAB script. Tracks were split into tracks before flavopiridol (−240–0 s) and after flavopiridol (400–640 s). Mean square displacement (MSD) analyses and computation of the diffusion coefficient were performed using MSDANALYZER script[28] with 'centroid drift correction', which derives the drift by computing the centre of mass of all particles at each time point. The MSD was calculated separately for the tracks before and after flavopiridol addition for each individual kinetochore trajectory at any given delay. After this, the weighted average across all MSD curves from one cell was computed. The diffusion coefficient (D) was estimated from the weighted mean MSD curve by fitting a linear function using the first quarter of the curve and calculating D from the following equation: $MSD = 2dDt$, in which d = dimensionality and t = time.

Measuring the molecular extension of Ki-67 after flavopiridol-induced mitotic exit. We treated live cells expressing mCherry–Ki-67–eGFP with the microtubule-stabilizing drug taxol to keep chromosomes apart after the induction of mitotic exit, thereby facilitating analysis of Ki-67 conformation at individual chromosome surfaces. To measure average distances between N- and C-terminal labels with different fluorescence spectra, we fitted Gaussian functions to line profiles. We previously demonstrated that we can measure the distance between two 500-nm TetraSpeck fluorescent beads (Invitrogen, T14792) with an accuracy of 2.9 ± 2.2 nm (mean ± s.d.)[8], as the translational shift between colour channels can be largely corrected by separately measuring peak-to-peak distances between two beads in the x/y plane.

To measure the average distance between the N and the C termini of Ki-67, taxol-arrested cells expressing mCherry–Ki-67–eGFP or eGFP–Ki-67–mCherry with or without the RASA mutation were recorded (×63 objective, 100-nm pixel size and linescan mode) before and 3–10 min after flavopiridol addition. Only chromosomes that had their arms oriented perpendicular to the imaging plane were analysed. From those chromosomes, we measured line profiles of the red and green channel that sectioned a single sister chromatid. After background subtraction and normalization to total fluorescence intensity, we fitted the sum of two Gaussian functions and measured the distance between the Gaussian centre positions separately for green and red fluorescence channels using R. The derived distance represents the sum of both

chromatic shifts perpendicular to the chromosome surface, and the molecular extension of Ki-67 along this axis can thus be derived by dividing this value by two. Imaging Ki-67 constructs with inverted positions for mCherry and eGFP yielded the expected inverted peak-to-peak distance, thus validating that the detected shift between fluorophore positions cannot be attributed to chromatic aberrations of the imaging system.

Airyscan data processing

Raw images recorded using the Airyscan detector were processed using ZEN 2011 software.

Statistical analyses and data reporting

No statistical methods were used to predetermine sample size. Data were tested for normality and equal variances with Shapiro–Wilk and D'Agostino–Pearson and Levene's tests ($\alpha = 0.05$), respectively. The appropriate statistical test was chosen as follows: unpaired normally distributed data were tested with a two-tailed *t*-test (in the case of similar variances) or with a two-tailed *t*-test with Welch's correction (in the case of different variances). Unpaired not-normally distributed data were tested with a two-tailed Mann–Whitney test (in the case of similar variances) or with a two-tailed Kolmogorov–Smirnov test (in the case of different variances). Paired normally distributed data were tested with two-tailed *t*-test and paired not-normally distributed data were tested with a Wilcoxon matched-pairs signed rank test. All tests were performed with Prism 7, except for Levene's test, which was performed in R. To minimize potential human bias, most experiments were automatically analysed by Fiji or MATLAB scripts. When manual annotation was required, blinding precautions were made. In Fig. 3b–d line profiles were drawn without knowledge of which construct was transfected.

Sample numbers

Fig. 1b, c: representative example and quantification of 19 cells. Fig. 1d, e: representative example and quantification of 22 cells. Fig. 1f, g: representative example and quantification of 30 cells. Fig. 1h, i: representative example and quantification of 12 cells. Fig. 2a, b: representative example and quantification of 16 cells. Fig. 2c, d: representative example and quantification of 35 cells. Fig. 3 a–c: chromosome numbers: R-Ki-67-G pre-flavo ($n = 34$), R-Ki-67-G post-flavo ($n = 46$), G-Ki-67-R pre-flavo ($n = 40$), G-Ki-67-R post-flavo ($n = 39$). Fig. 3f, g: cell numbers: wild-type ($n = 24$), Ki-67-KO ($n = 22$). Fig. 4a–c, Extended Data Fig. 10c, d: cell numbers: wild-type ($n = 46$), Ki-67-KO ($n = 29$). Fig. 4d–f, Extended Data Fig. 10e–h: cell numbers: wild-type ($n = 23$), leptomycin-B-treated ($n = 22$), Ki-67-KO ($n = 8$). Extended Data Fig. 1a–c: cell viability: wild-type ($n = 754$ cells), GEMs ($n = 930$ cells), L10–eGFP ($n = 603$ cells); cell proliferation: wild-type ($n = 2{,}001$ cells), GEMs ($n = 2{,}283$ cells), L10–eGFP ($n = 2{,}178$ cells); mitotic duration ($n = 320$ cells per cell line). Extended Data Fig. 2a, b: representative example and quantification of 16 cells. Extended Data Fig. 2c, d: cell numbers: wild-type ($n = 18$), leptomycin-B-treated ($n = 15$). Extended Data Fig. 3a–d: representative examples and quantification: metaphase ($n = 9$ cells), 3–6 min after anaphase onset ($n = 14$ cells), more than 8 min after anaphase onset ($n = 8$ cells), prometaphase ($n = 11$ cells), 10 min after flavopiridol addition ($n = 12$ cells), 20 min after flavopiridol addition ($n = 13$ cells). Extended Data Fig. 3e, f: representative example and quantification of 20 cells. Extended Data Fig. 3g, h: representative example and quantification of 11 cells. Extended Data Fig. 3i: representative example of 14 cells. Extended Data Fig. 4a, b: cell numbers: wild-type ($n = 13$), latrunculin-B-treated ($n = 22$). Extended Data Fig. 4c, d: representative example and quantification of 21 cells. Extended Data Fig. 4e–h: representative example and quantification of 13 cells. Extended Data Fig. 5a, b: representative examples and quantification. Cell numbers: DMSO control ($n = 24$), flavopiridol-treated ($n = 25$). Extended Data Fig. 5c, d: representative examples and quantification. Sample numbers: nocodazole-treated ($n = 27$ cells), nocodazole-and-flavopiridol-treated ($n = 23$ cells). Extended Data Fig. 6a–c: representative example and quantification of 23 control and 23 siBAF-treated cells. Extended Data Fig. 6e, f: sample number: $n = 21$ cells. Extended Data Fig. 6g, h: representative example and quantification of 41 cells. Extended Data Fig. 6i, j: representative example and quantification of 27 cells. Extended Data Fig. 7a, b: representative examples and quantification. Cell numbers: Ki-67-KO ($n = 29$), Ki-67-KO + eGFP–Ki-67 ($n = 28$). Extended Data Fig. 7c: representative example of two experiments. Extended Data Fig. 7d, e: representative examples and quantification. Cell numbers: Ki-67-KO ($n = 115$), Ki-67-KO + TSA ($n = 111$). Extended Data Fig. 7f, g: representative examples and quantification. Cell numbers: Ki-67-KO ($n = 21$), Ki-67 wild-type ($n = 31$), Ki-67-KO + eGFP–Ki-67 ($n = 32$). Extended Data Fig. 8c, d: cell numbers: wild-type ($n = 22$), RASA ($n = 23$). Extended Data Fig. 8e: cell numbers: R-Ki-67(RASA)-G pre-flavo ($n = 32$), R-Ki-67(RASA)-G post-flavo ($n = 28$), G-Ki-67(RASA)-R pre-flavo ($n = 37$), G-Ki-67(RASA)-R post-flavo ($n = 34$). Extended Data Fig. 8f, g: representative examples and quantification of two experiments. Cell numbers: wild-type pre-flavo ($n = 38$), wild-type 5 min post-flavo ($n = 61$), wild-type 10 min post-flavo ($n = 72$), wild-type 20 min post-flavo ($n = 73$), Ki-67-KO pre-flavo ($n = 23$), Ki-67-KO 5 min post-flavo ($n = 61$), Ki-67-KO 10 min post-flavo ($n = 65$), Ki-67-KO 20 min post-flavo ($n = 55$). Extended Data Fig. 9b, c: cell numbers H2B–FKBP + H2B–FRB ($n = 23$), H2B–FKBP ($n = 12$). Extended Data Fig. 10a, b: representative example and quantification of 15 cells.

Processing of figures and videos

In all figures the contrast was linearly adjusted for visual representation. In all videos as well as figures showing GEM particles the channel displaying the cytoplasmic marker was additionally processed with the 'subtract background' function in ImageJ, using a 50-pixel rolling ball radius.

Reporting summary

Further information on research design is available in the Nature Research Reporting Summary linked to this paper.

Data availability

Raw microscopy data are available from the corresponding authors upon request, given the large file sizes that are involved. Source data are provided with this paper.

Code availability

All of the steps of the image analyses that were performed in this study are described in detail to allow reproduction of the results. We will provide the code upon request.

22. Schmitz, M. H. A. et al. Live-cell imaging RNAi screen identifies PP2A-B55α and importin-β1 as key mitotic exit regulators in human cells. *Nat. Cell Biol.* **12**, 886–893 (2010).
23. Lukinavičius, G. et al. SiR-Hoechst is a far-red DNA stain for live-cell nanoscopy. *Nat. Commun.* **6**, 8497 (2015).
24. Ran, F. A. et al. Double nicking by RNA-guided CRISPR Cas9 for enhanced genome editing specificity. *Cell* **154**, 1380–1389 (2013).
25. Huang, L.-K. & Wang, M.-J. J. Image thresholding by minimizing the measures of fuzziness. *Pattern Recognit.* **28**, 41–51 (1995).
26. Sommer, C., Hoefler, R., Samwer, M. & Gerlich, D. W. A deep learning and novelty detection framework for rapid phenotyping in high-content screening. *Mol. Biol. Cell* **28**, 3428–3436 (2017).
27. Thévenaz, P., Ruttimann, U. E. & Unser, M. A pyramid approach to subpixel registration based on intensity. *IEEE Trans. Image Process.* **7**, 27–41 (1998).
28. Tarantino, N. et al. TNF and IL-1 exhibit distinct ubiquitin requirements for inducing NEMO-IKK supramolecular structures. *J. Cell Biol.* **204**, 231–245 (2014).

Acknowledgements The authors thank S. Tietscher for histone-level verification, K. F. Leesch and the IMBA/IMP/GMI BioOptics and Molecular Biology Service facilities for technical support, M. Tchórzewski for the L10-eGFP plasmid and I. Patten and Life Science Editors (https://www.lifescienceeditors.com) for comments on the manuscript. Research in the laboratory of D.W.G. was supported by the Austrian Academy of Sciences, by an ERC Starting (Consolidator) Grant (number 281198), by the Wiener Wissenschafts-, Forschungs- und Technologiefonds (WWTF; project numbers LS14-009 and LS17-003) and by the Austrian

Science Fund (FWF special research program 'Chromosome Dynamics' SFB F34-06, Doktoratskolleg 'Chromosome Dynamics' DK W1238); research in the laboratory of S.C.-H. was supported by the German Research Foundation (DFG, project number 402723784); M.P., A.H.-A. and M.W.G.S. have received PhD fellowships from the Boehringer Ingelheim Fonds; S.C.-H. has received funding from a Human Frontier Science Program (LTF000996/2013 and CDA00045/2019); and L.J.H. was supported by the National Institutes of Health (R01GM132447) and by the Whitman Fellows programme of the Woods Hole Marine Biology laboratory.

Author contributions D.W.G. and S.C.-H. conceived the project. M.P. designed, performed and analysed experiments investigating nucleo-cytoplasmic compartmentalization during anaphase and during chromosome clustering in spindle-less mitotic exit, as well as experiments addressing the role of actin and H3 phosphorylation at Ser10. S.C.-H. designed, performed and analysed experiments addressing the localization, conformation and mechanism of Ki-67 in chromosome clustering, chromosome motility in the clustered state and the inducible H2B–H2B interaction system. A.H.-A. performed and analysed experiments probing chromosome clustering in Ki-67-knockout cells and phenotype rescue by expression of transgenic Ki-67. M.W.G.S. performed initial experiments on GEM localization during mitosis and the effect of trichostatin A on chromosome clustering. M.S. designed, performed and analysed experiments addressing the localization and function of BAF in chromosome clustering, with help from M.P. C.B. characterized the cell lines stably expressing L10–eGFP and GEMs. L.J.H. generated GEM expression constructs. D.W.G. and S.C.-H. acquired funding and supervised the project. D.W.G. and S.C.-H. wrote the manuscript, with help from M.P.

Competing interests The authors declare no competing interests.

Additional information

Supplementary information is available for this paper at https://doi.org/10.1038/s41586-020-2672-3.

Correspondence and requests for materials should be addressed to S.C.-H. or D.W.G.

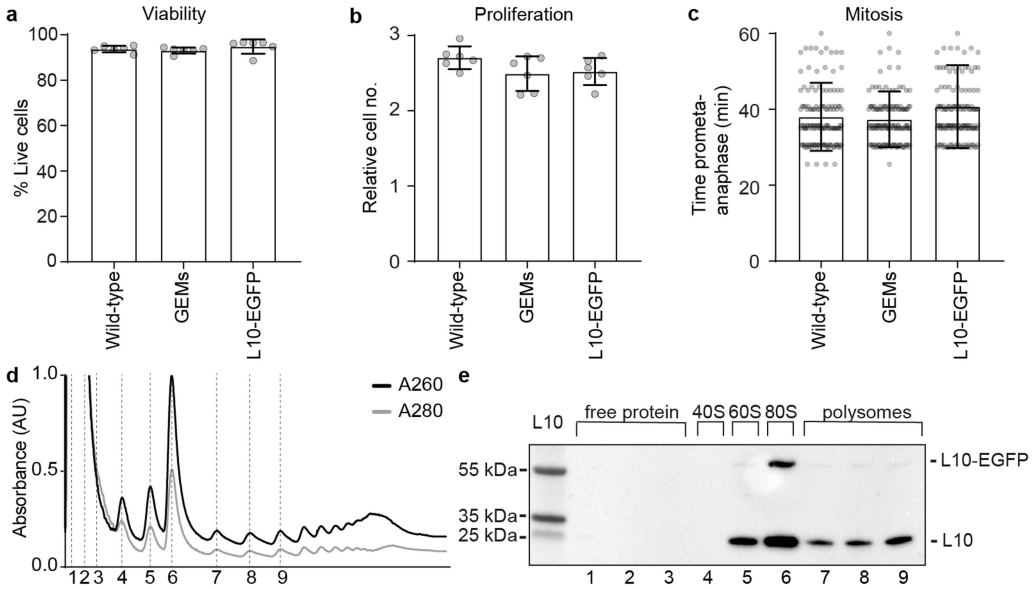

Extended Data Fig. 1 | Characterization of GEM- and L10-expressing stable cell lines. a, Viability of HeLa cell lines stably expressing markers as indicated, measured by counting Hoechst-stained cell nuclei that were negative for the cell death marker TO-PRO-3. Cell numbers: $n = 754$ (wild-type), $n = 930$ (GEMs), $n = 603$ (L10–eGFP). **b**, Proliferation of HeLa cell lines stably expressing markers as indicated, quantified as fold-change of live cells between 0 and 24 h in time-lapse microscopy videos. Cell number at 24 h: $n = 2{,}001$ (wild-type), $n = 2{,}178$ (L10–eGFP), $n = 2{,}283$ (GEMs). **c**, Mitotic duration in HeLa cell lines stably expressing markers as indicated, scored by manual measurement of the time from prometaphase to anaphase onset. Cell numbers: $n = 320$ (wild-type), $n = 320$ (GEMs), $n = 320$ (L10–eGFP). **d**, **e**, Validation of L10–eGFP incorporation into ribosomes. **d**, Cell lysate fractions separated on a sucrose gradient. Dashed lines indicate fractions loaded on the gel blotted in **e**. **e**, Immunoblot analysis of ribosomal protein L10 in cell lysate fractions, isolated from cells stably expressing L10–eGFP. Annotations of endogenous L10 and L10–eGFP are based on predicted molecular weights. For gel source data, see Supplementary Fig. 1. Bars indicate mean and error bars represent ± s.d.

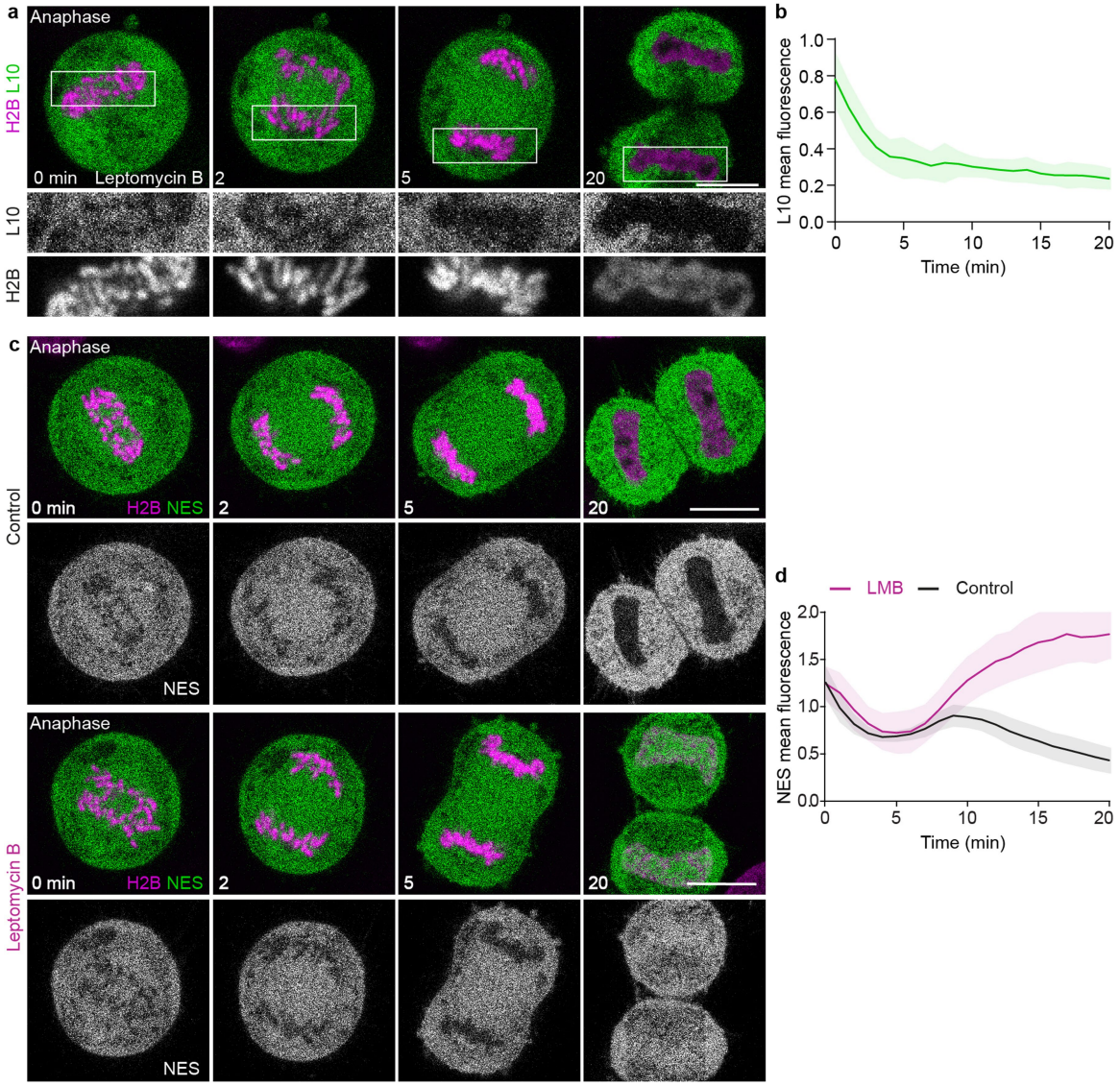

Extended Data Fig. 2 | Ribosomes are excluded from the nucleus in the absence of nuclear envelope transport. a, HeLa cell expressing the mature ribosome marker L10–eGFP and H2B–mCherry progressing through anaphase in the presence of leptomycin B. **b**, Quantification of L10–eGFP mean fluorescence intensity within the chromosomal region normalized to surrounding cytoplasm, in anaphase cells as in **a**. $n = 16$ cells. **c**, **d**, Validation of Exportin-1 inhibition by leptomycin B. **c**, Live HeLa cells expressing fluorescently labelled H2B and GFP–NES were imaged during mitotic progression by time-lapse microscopy, either untreated (control) or in presence of leptomycin B. Time point 0 min refers to anaphase onset. **d**, Quantification of GFP–NES mean fluorescence intensity within the chromosomal region normalized to pre-anaphase in control and leptomycin B treated cells, as in **c**. $n = 18$ cells (control), $n = 15$ cells (leptomycin B). Lines indicate mean and shaded areas represent ± s.d. Scale bars, 10 µm.

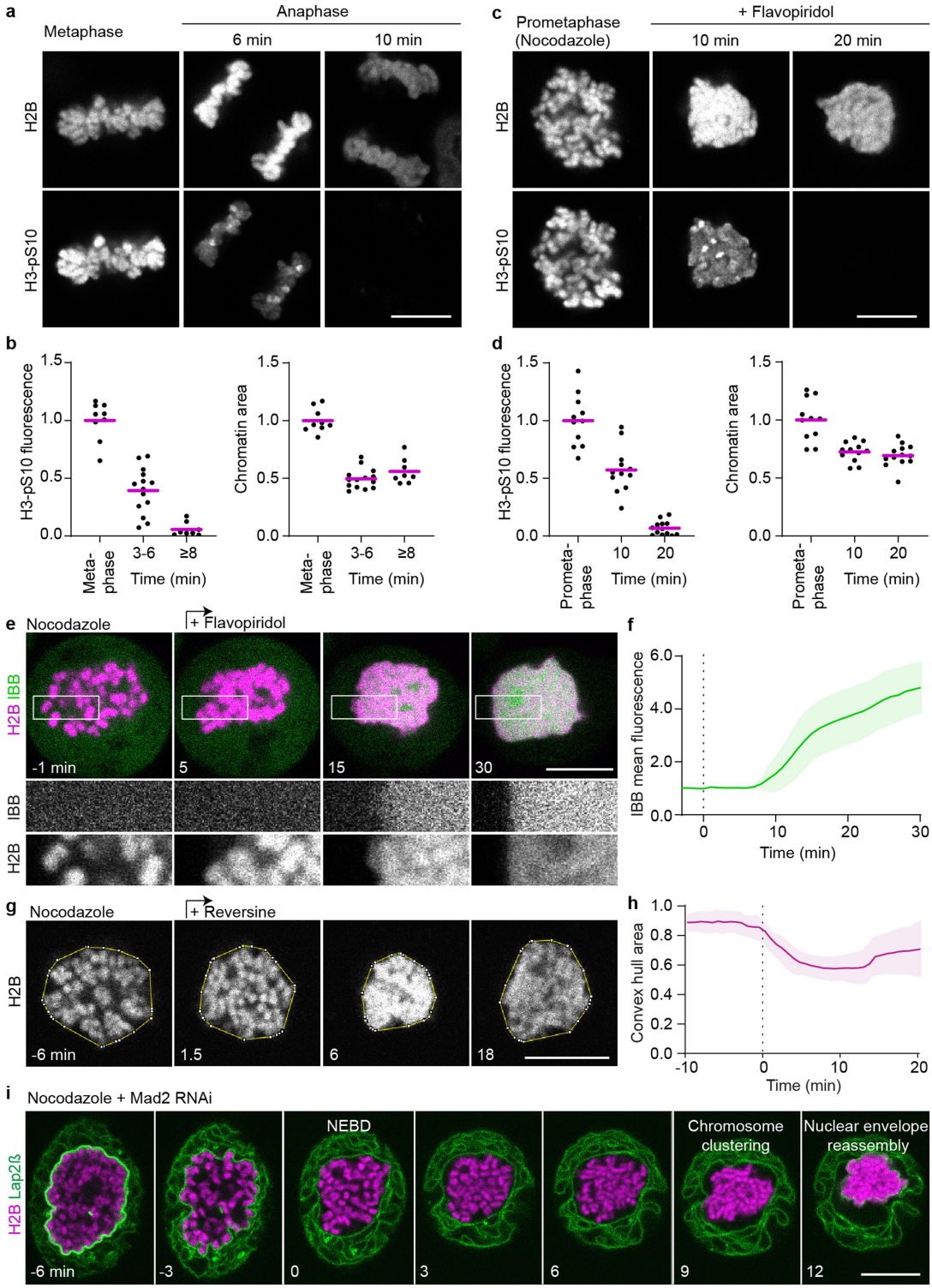

Extended Data Fig. 3 | See next page for caption.

Extended Data Fig. 3 | Chromosomes cluster and the nucleus reassembles in spindle-less cells after the induction of mitotic exit by different experimental procedures. a–**d**, Validation of mitotic exit in spindle-less cells by comparing H3(S10) dephosphorylation kinetics during unperturbed anaphase and spindle-less mitotic exit. **a**, Example images of wild-type HeLa cells during unperturbed anaphase fixed after time-lapse imaging, in metaphase, 6 min (maximally clustered) and 10 min after anaphase onset. Upper panel: chromatin labelled with H2B–mCherry, lower panel: H3(pS10) immunofluorescence. Single *z*-slice shown. **b**, Quantification of H3(pS10) mean fluorescence intensity and chromatin area in unperturbed mitosis, as shown in **a**. Cell numbers: $n = 9$ (metaphase), $n = 14$ (3-6 min after anaphase onset), $n = 8$ (≥8 min after anaphase onset). Normalization to average value of metaphase time point. **c**, Example images of wild-type HeLa cells during spindle-less mitosis fixed after time-lapse imaging, in prometaphase (no flavopiridol), 10 min (maximally clustered) and 20 min after flavopiridol addition. Imaging as in **a**. **d**, Quantification of H3(pS10) mean fluorescence intensity and chromatin area in spindle-less mitosis, as shown in (**c**), demonstrates that histone 3-serine 10 was efficiently dephosphorylated in flavopiridol-induced mitotic exit and chromosomes cluster to a degree comparable to that of normal late anaphase. Cell numbers: $n = 11$ (nocodazole arrested pro-metaphase), $n = 12$ (10 min after flavopiridol addition), $n = 13$ (20 min after flavopiridol addition). Normalization to average value of prometaphase time point. **e**, Time-lapse microscopy of HeLa cell expressing IBB–eGFP and H2B–mCherry incubated in nocodazole; flavopiridol was added ($t = 0$ min) to induce mitotic exit. **f**, Quantification of IBB–eGFP mean fluorescence intensity within the chromosomal region, normalized to pre-flavopiridol time points, during spindle-less mitotic exit as in **e**. $n = 20$ cells. **g**, Time-lapse microscopy of a HeLa cell expressing H2B–mCherry, progressing through reversine-induced mitotic exit in the absence of spindle. Yellow line indicates convex hull around chromosomes, single *z*-slice shown. Time is relative to onset of clustering. **h**, Quantification of chromosome convex hull area of 11 cells as in **g**. Individual cell curves were aligned based on half-maximum value of convex hull area. Normalization to average of first 4 time points. **i**, Live HeLa cell undergoing mitosis upon RNAi-mediated depletion of the spindle checkpoint protein MAD2 in the absence of a spindle. The cell line stably expresses H2B–mCherry and membrane marker AcGFP–LAP2β. Time relative to nuclear envelope breakdown (NEBD), single *z*-slice shown. Representative example of 14 cells shown. Bars indicate mean in **b**, **d**; lines and shaded areas indicate mean ± s.d. in **f**, **h**. Scale bars, 10 µm.

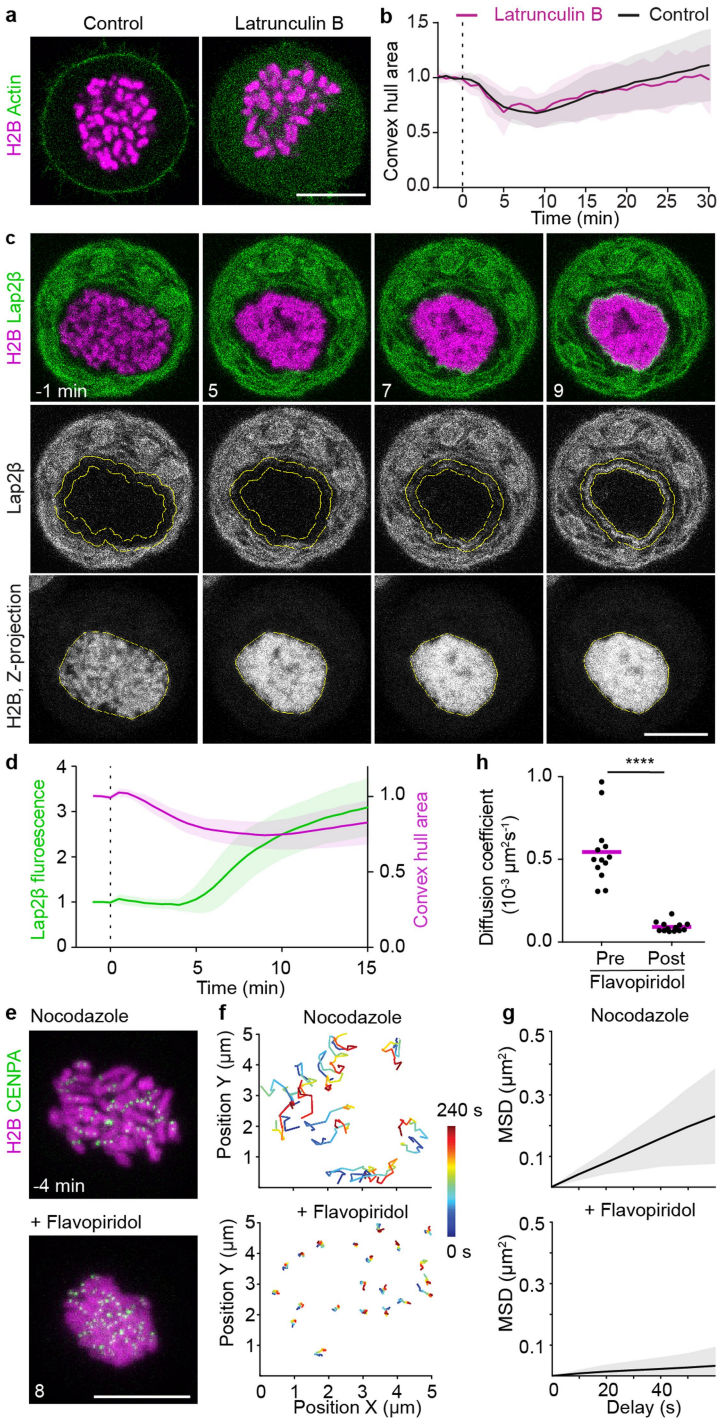

Extended Data Fig. 4 | Chromosome clustering is independent of F-actin, precedes enwrapment by the nuclear envelope and suppresses chromosome mobility. a, **b**, Effect of actin depolymerization on chromosome clustering. **a**, Live HeLa cells stably expressing actin–eGFP and H2B–mCherry were imaged in the absence (control) or presence of latrunculin B. Nocodazole was present in both conditions. **b**, Quantification of chromosome convex hull area during a flavopiridol induced mitotic exit in the presence of nocodazole, in the absence (control) and presence of latrunculin B as shown in **a**, normalized to average area pre-flavopiridol addition. Cell numbers: $n = 13$ (control), $n = 22$ (latrunculin B). **c**, Timing of chromosome clustering relative to nuclear envelopment. Live mitotic HeLa cell expressing H2B–mCherry and the inner nuclear envelope protein AcGFP–LAP2β were imaged in presence of nocodazole; flavopiridol was added at $t = 0$ min to induce mitotic exit. **d**, Quantification of chromosomal area by convex hull (yellow line in H2B channel in **c**) and quantification of AcGFP–LAP2β accumulation at the surface of the chromatin region, within a rim of 1.6 µm width (yellow ROI in LAP2β channel in (**c**)). $n = 21$ cells. **e**–**h**, Kinetochore tracking in cells progressing through spindle-less mitotic exit. **e**, Live mitotic HeLa cell stably expressing H2B–mCherry and CENP-A–eGFP imaged in the presence of nocodazole before and after flavopiridol addition, time-lapse = 10 s; *z*-projection. **f**, Kinetochore trajectories (total length: 240 s) starting 240 s before and at 400 after flavopiridol addition. **g**, Representative MSD analyses of kinetochore tracks (CENP-A–eGFP) of nocodazole-treated mitotic HeLa cells before and after flavopiridol addition. **h**, Diffusion coefficients derived from mean square displacement (MSD) analyses of trajectories as in **f**. Significance was tested by a two-tailed ratio paired *t*-test (****$P = 2.9 \times 10^{-11}$). $n = 13$ cells. Bars and lines indicate mean, shaded areas indicate ± s.d., dashed vertical lines refer to flavopiridol addition. Scale bars, 10 µm.

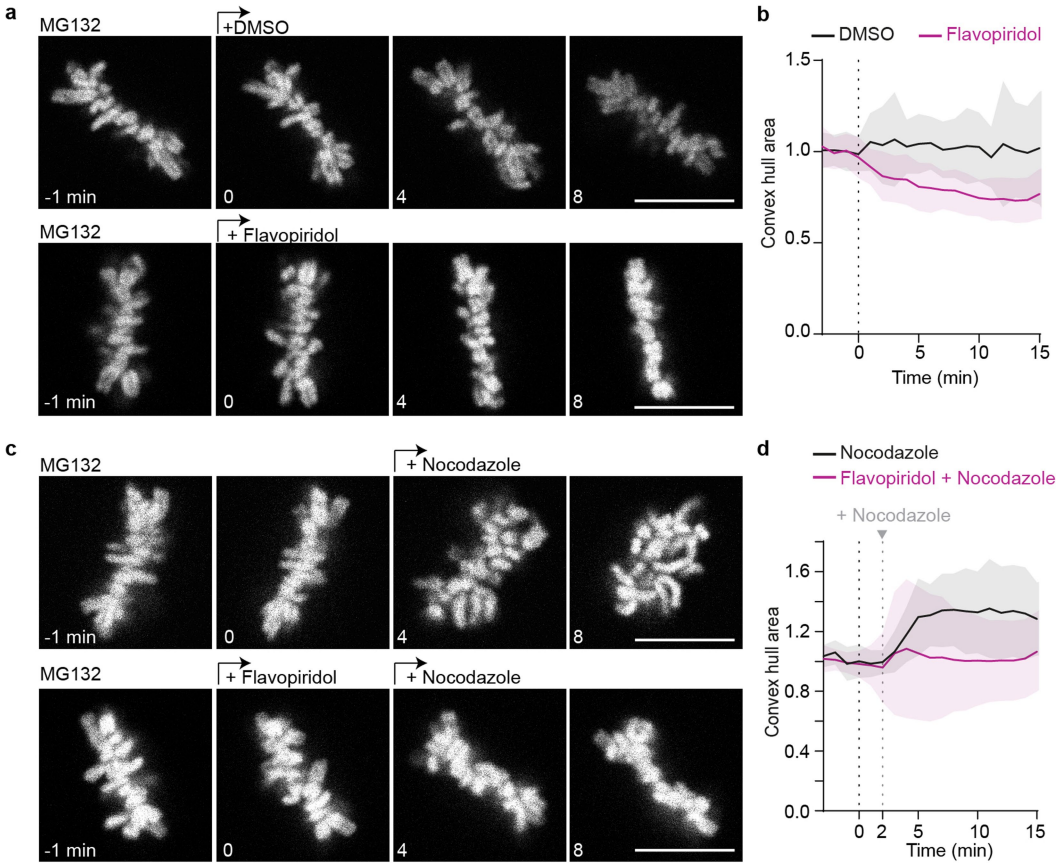

Extended Data Fig. 5 | Chromosomes cluster in the presence of a mitotic spindle after flavopiridol-mediated induction of mitotic exit. Live-cell microscopy of wild-type HeLa cells stably expressing H2B–mCherry synchronized to metaphase by MG132 treatment. **a**, Upper panel: negative control treated with dimethyl sulfoxide (DMSO) solvent, lower panel: mitotic exit induced through acute flavopiridol addition at $t = 0$ min. Chromosome arms extend out of the metaphase plate before flavopiridol addition, but densely cluster on the metaphase plate 8 min after flavopiridol addition. **b**, Quantification of chromosome convex hull area of 24 control and 25 flavopiridol treated cells, as in **a**. **c**, Top, acute mitotic spindle depolymerization by addition of nocodazole at $t = 2$ min leads to chromosome movement out of the metaphase plate; bottom, mitotic exit was induced by flavopiridol (0 min), briefly before nocodazole-mediated spindle disassembly (2 min), preventing movement of chromosomes out of the metaphase plate. **d**, Chromosome convex hull area measurements of 27 nocodazole and 23 flavopiridol and nocodazole treated cells, as shown in **c**. Values normalized to average of all frames before first drug treatment. Showing single *z*-slices, lines and shaded areas indicate mean ± s.d., dashed vertical lines indicate drug addition, scale bars, 10 µm.

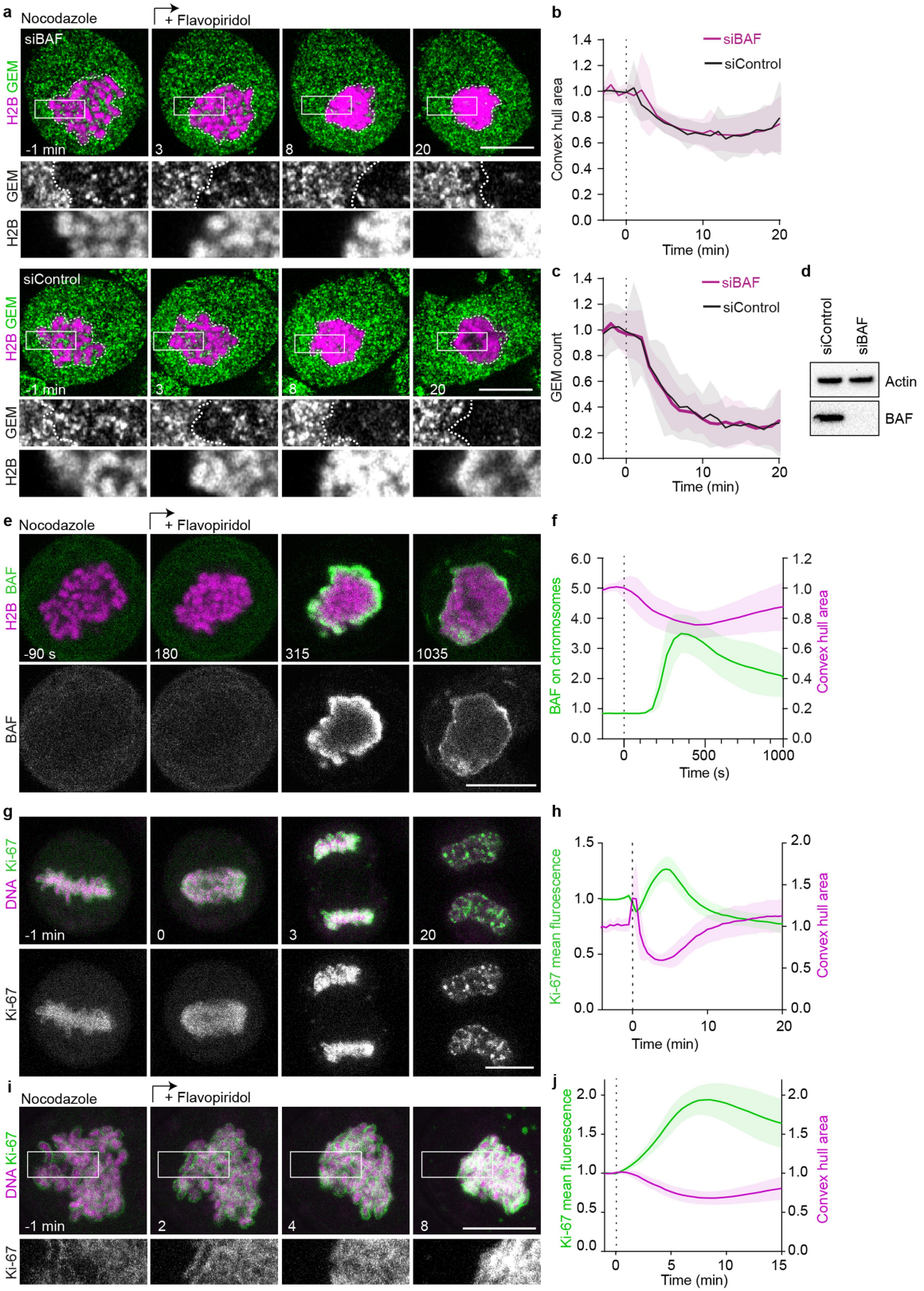

Extended Data Fig. 6 | See next page for caption.

Extended Data Fig. 6 | Chromosome clustering is not mediated by association with BAF or removal of Ki-67. a–**c**, Effect of BAF depletion on chromosome clustering. **a**, Live mitotic HeLa cells stably expressing H2B–mCherry and GEMs were imaged 72 h after siRNA transfection, in the presence of nocodazole; flavopiridol was added at $t = 0$ min to induce mitotic exit. White dashed lines indicate chromosomal areas, single *z*-slice shown. **b**, Quantification of chromosome convex hull area, normalized to pre-flavopiridol addition. **c**, GEM particle count within chromosomal area normalized to pre-flavopiridol addition. $n = 23$ cells (siBAF), $n = 23$ cells (siControl). **d**, Immunoblot analysis of BAF and actin 72 h after siRNA transfection, showing one of two biological replicates. For gel source data, see Supplementary Fig. 1. **e**, Localization of BAF–eGFP in live mitotic HeLa cell imaged in the presence of nocodazole; flavopiridol was added at $t = 0$ s to induce mitotic exit. **f**, Quantification of chromosome convex hull area and BAF–eGFP accumulation at the surface of the chromatin region as in **e**, normalized to pre-flavopiridol. $n = 21$ cells. **g**, Localization of Ki-67, eGFP tagged on endogenous loci in live HeLa cell progressing from metaphase to anaphase (anaphase onset = 0 min), DNA was stained with SiR-Hoechst, z-projection. **h**, Quantification of chromosome convex hull area and eGFP–Ki-67 mean fluorescence intensity on chromosomes, normalized to pre-anaphase, for 41 cells as in **g**. **i**, Localization of Ki-67 during spindle-less mitotic exit. Time-lapse microscopy of mitotic HeLa cell as in **g**, in the presence of nocodazole; flavopiridol was added ($t = 0$ min) to induce mitotic exit. Z-projection. **j**, Quantification of chromosome convex hull area and eGFP–Ki-67 mean fluorescence intensity on chromosomes of 27 cells as in **i**. Lines and shaded areas indicate mean ± s.d., scale bars, 10 µm.

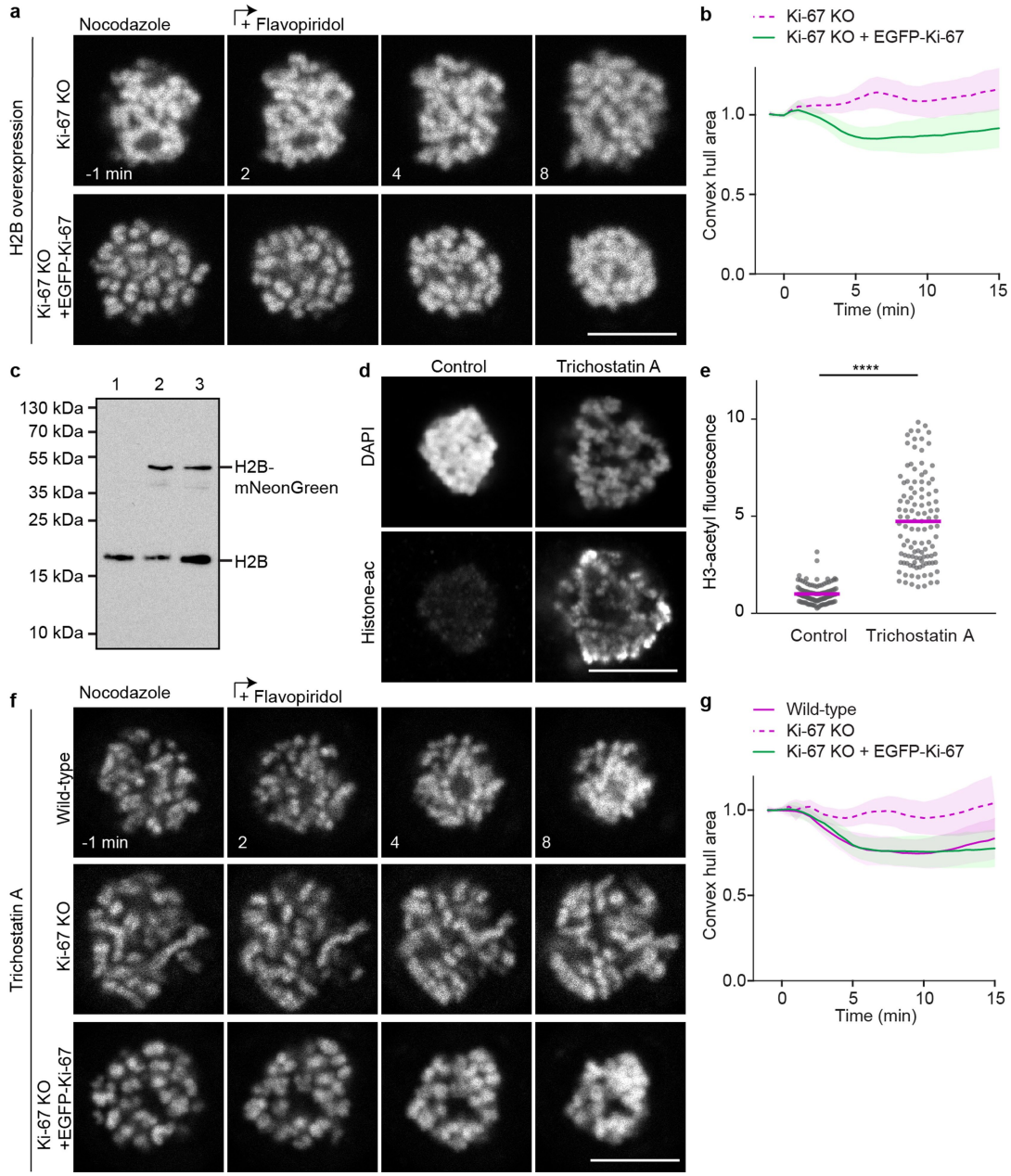

Extended Data Fig. 7 | Ki-67 is required for chromosome clustering in Ki-67-knockout cells after histone overexpression or histone hyperacetylation. a, Time-lapse microscopy of clustering-deficient HeLa Ki-67-KO cell stably expressing H2B–mCherry to high levels during a flavopiridol-induced mitotic exit in the presence of nocodazole. Transient expression of eGFP–Ki-67 to levels at least matching Ki-67 endogenous levels (lower panel). Single z-slice shown. **b**, Chromosome convex hull area quantification, normalized to pre-flavopiridol time points, of 29 Ki-67-KO and 28 Ki-67-KO + eGFP–Ki-67cells as in **a**. **c**, Immunoblot analysis of H2B from cell lysates, isolated from wild-type cells (1) or cells transiently expressing H2B–mNeonGreen (2, 3). Sample 3 was lysed after 48 h, whereas sample 2 was additionally FACS sorted for the 10% brightest cells which we estimated to represent the population of cells that suppress the Ki-67-knockout individualization failure phenotype. For gel source data, see Supplementary Fig. 1. $n = 2$ biological repeats. **d**, **e**, Immunofluorescence of acetylated H3 of Ki-67-KO cells arrested in nocodazole with or without trichostatin A. **d**, Representative examples. Single *z*-slices shown. **e**, Quantification of acetylated H3 mean fluorescence intensity in Ki-67-KO cells arrested in nocodazole with and without trichostatin A. Bars represent mean, significance was tested with a two-tailed Kolmogorov–Smirnov test. (****$P = 2.22 \times 10^{-16}$). $n = 115$ cells (Ki-67-KO), $n = 111$ cells (Ki-67-KO + TSA). **f**, Time-lapse microscopy of HeLa wild-type or clustering-deficient Ki-67-KO cells with or without transient re-expression of Ki-67 during a flavopiridol-induced mitotic exit in the presence of nocodazole. Cells were treated with trichostatin A 2 h before imaging to rescue the Ki-67-knockout individualization failure phenotype in Ki-67-KO cells. Representative examples stained with SiR-Hoechst, single *z*-slices shown. **g**, Chromosome convex hull area, normalized to pre-flavopiridol time points, quantification of 21 Ki-67-KO, 31 wild-type and 32 Ki-67-KO + eGFP–Ki-67 cells as in **f**. Lines and shaded areas indicate mean ± s.d. (**b**, **g**), scale bars, 10 µm.

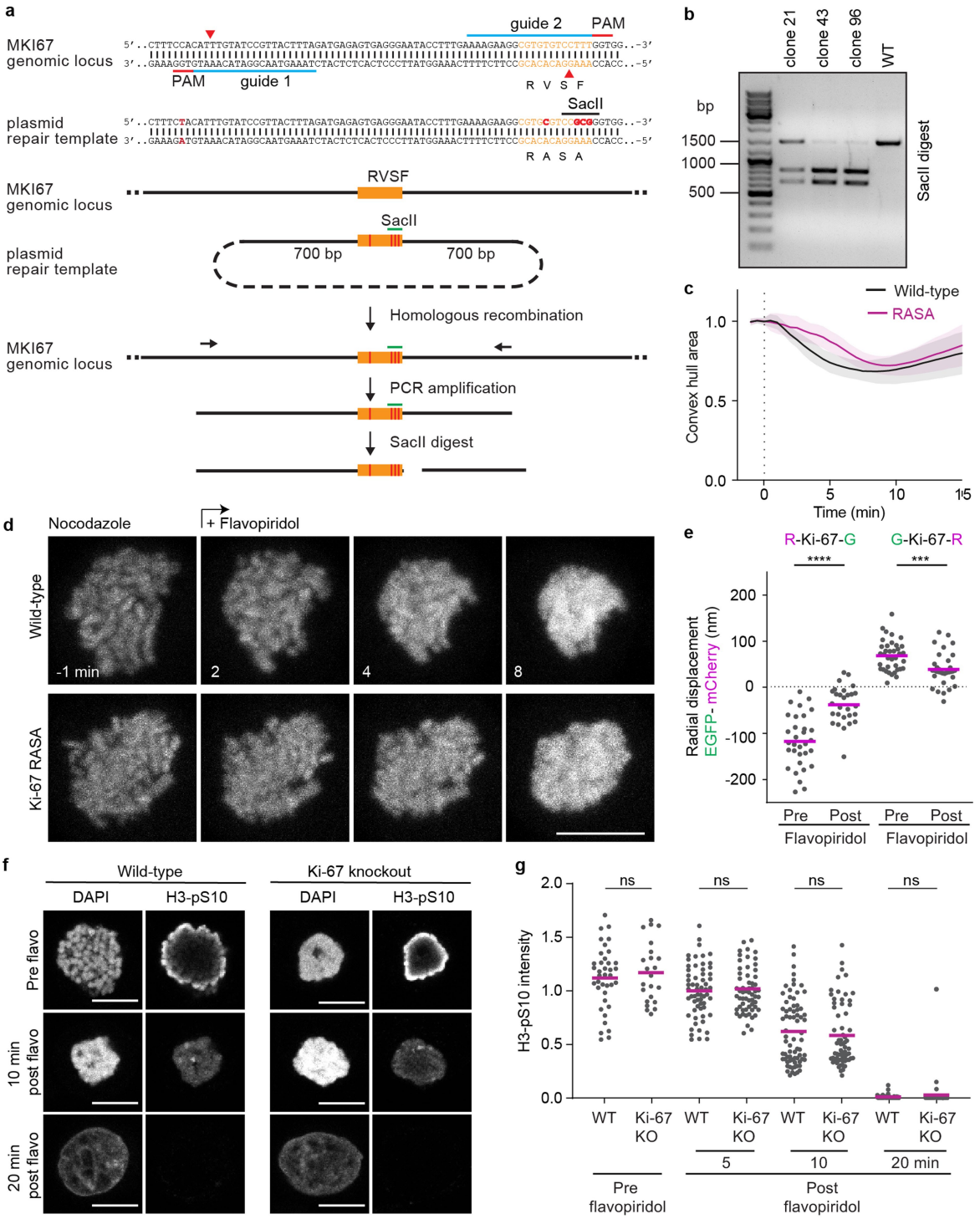

Extended Data Fig. 8 | See next page for caption.

Extended Data Fig. 8 | Ki-67 does not mediate chromosome clustering through PP1 recruitment or through H3(S10) dephosphorylation. **a**, Schematic of genotyping strategy to endogenously mutate Ki-67's PP1-binding motif RVSF to RASA. A newly generated SacII restriction site generated by CRISPR–Cas9 nickase as depicted was used to detect correctly mutated alleles. **b**, SacII restriction fragments were detected by gel electrophoresis following the assay depicted in **a**, showing successful recombination of all three Ki-67 alleles present in HeLa cells for clone 43 and 96. Showing one example of two biological replicates. **c**, **d**, Spindle-less mitotic exit in wild-type cells and in homozygous Ki-67(RASA)-mutant cells. Live cells were imaged in the presence of nocodazole; flavopiridol was added ($t = 0$ min) to induce mitotic exit. Quantification of chromosome convex hull area, normalized to pre-flavopiridol time points (**c**) and representative examples stained with SiR-Hoechst (**d**). *Z*-projection. Lines and shaded areas indicate mean ± s.d. $n = 22$ cells (wild-type), $n = 23$ cells (RASA). **e**, Molecular organization of the Ki-67 RASA mutant on the surface of mitotic chromosomes before and after flavopiridol addition to taxol treated cells. Ki-67(RASA) was tagged by mCherry and eGFP on either protein end, respectively, and expressed in HeLa cells bearing the endogenous RASA mutation in all three copies of Ki-67. Bars represent mean, significance was tested by a two-tailed unpaired *t*-test (****$P = 8.3 \times 10^{-8}$, ***$P = 0.00049$). Chromosome numbers: $n = 32$ (R-Ki-67-G, pre), $n = 28$ (R-Ki-67-G, post), $n = 37$ (G-Ki-67-R, pre), $n = 34$ (G-Ki-67-R, post). **f**, **g**, Immunofluorescence of H3(pS10) during spindle-less mitotic exit in wild-type and Ki-67-KO cells. **f**, Representative examples of wild-type and Ki-67-KO cells before, 10 and 20 min after flavopiridol addition. Single *z*-slice is shown. **g**, Quantification of H3(pS10) mean fluorescence intensity before (wild-type $n = 38$ cells, Ki-67-KO $n = 23$ cells) and 5 min (wild-type $n = 61$ cells, Ki-67-KO $n = 61$ cells), 10 min (wild-type $n = 72$ cells, Ki-67-KO $n = 65$ cells) and 20 min (wild-type $n = 73$ cells, Ki-67-KO $n = 55$ cells) after mitotic exit induction with flavopiridol in wild-type and Ki-67-KO cells. Values normalized to average of wild-type 5 min time point. Showing combined data of two independent biological replicates. Bars represent mean, significance was tested with a two-tailed Mann–Whitney test ($P = 0.72$ for pre-flavopiridol time point, $P = 0.96$ for 5 min time point, $P = 0.71$ for 10 min time point and $P = 0.26$ for 20 min time point). Scale bars, 10 µm.

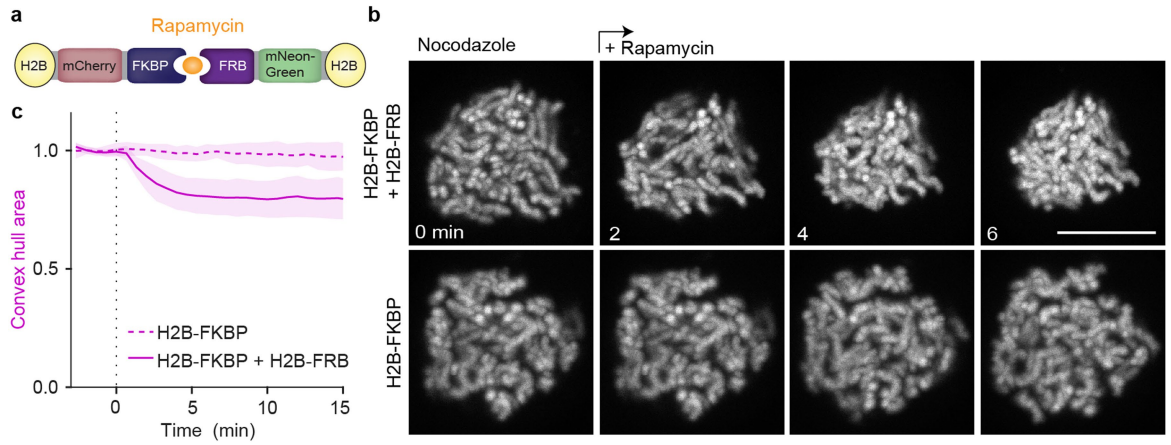

Extended Data Fig. 9 | Chromosome clustering can be artificially induced through increased adhesion between chromosomes. a, Design of an inducible H2B–H2B interaction system. **b**, Live HeLa cells expressing H2B–mCherry–FKBP and H2B–mNeonGreen–FRB or only H2B–mCherry–FKBP were imaged before and after rapamycin addition. *Z*-projection; scale bar, 10 µm. **c**, Normalized chromosome convex hull area quantification as in **b** of 23 cells coexpressing H2B–mCherry–FKBP and H2B–mNeonGreen–FRB, versus 12 negative control cells expressing H2B–mCherry–FKBP alone. Lines and shaded areas indicate mean ± s.d.

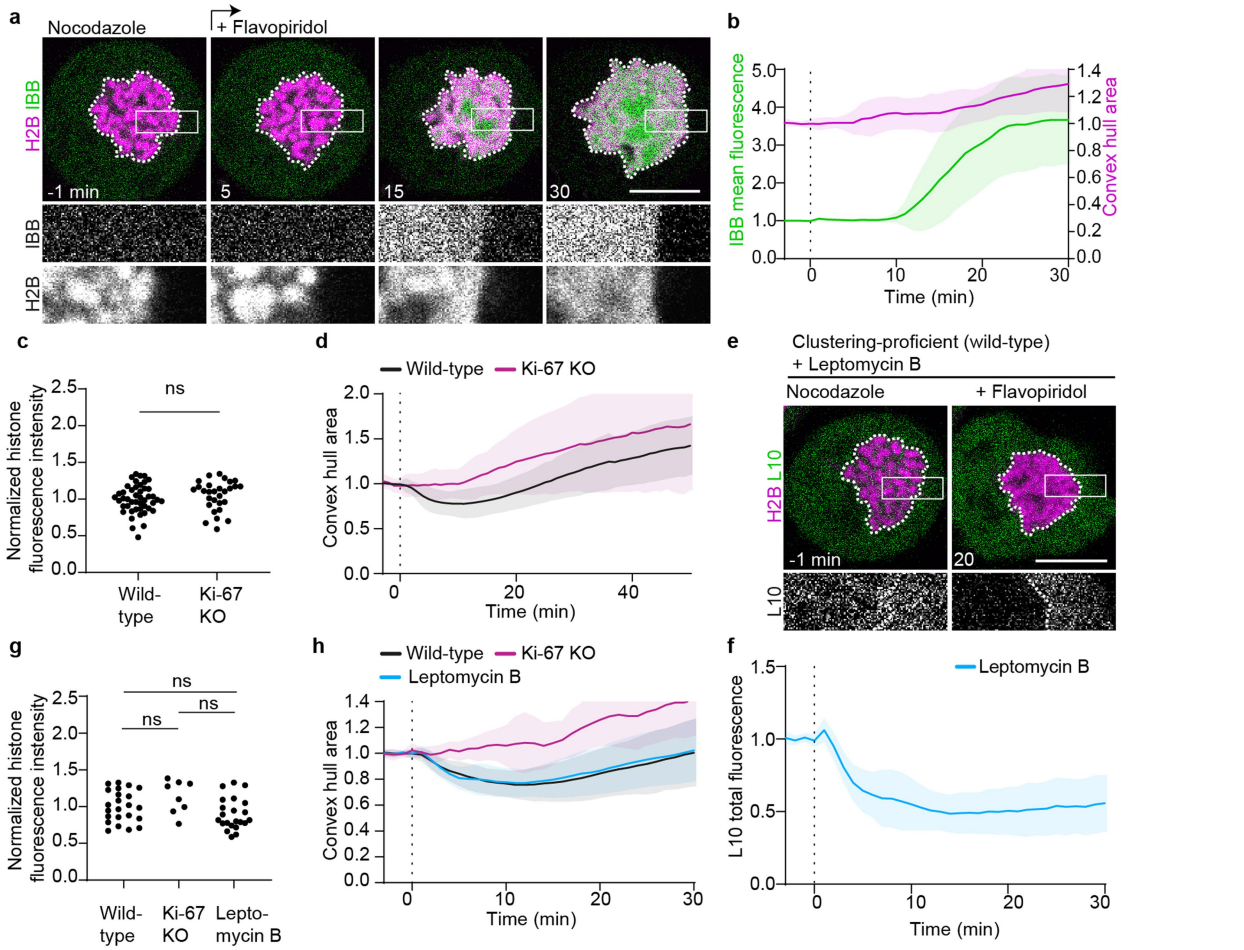

Extended Data Fig. 10 | Clustering-deficient cells assemble a transport-competent nuclear envelope. a, Time-lapse microscopy of clustering-deficient HeLa Ki-67-KO cells transiently expressing H2B–mCherry to high levels, and stably expressing IBB–eGFP, during a flavopiridol-induced mitotic exit in the presence of nocodazole. **b**, Quantification of IBB–eGFP mean fluorescence intensity within the chromosomal area (green) and quantification of chromosome convex hull area (magenta) in clustering-deficient cells as in **a**, normalized to pre-flavopiridol. $n = 15$ cells. **c**, **d**, H2B–mCherry expression levels and chromosomal area measurements for cells shown in Fig. 4a–c. **c**, Quantification of H2B–mCherry total fluorescence for cells analysed in Fig. 4c (all data points normalized to mean of wild-type dataset). **d**, Chromosome convex hull area quantification (normalized to pre-flavopiridol area) for cells quantified in Fig. 4c. $n = 46$ cells (wild-type), $n = 29$ cells (Ki-67-KO). **e**, Clustering-proficient HeLa cell imaged as in Fig. 4d, but treated with leptomycin B. **f**, Quantification of total L10 fluorescence in nuclear regions as shown in **e**, normalized to average of pre-flavopiridol addition. $n = 22$. **g**, **h**, Quantification of H2B–mCherry total fluorescence and chromosome convex hull area for cells analysed in Fig. 4f and in **f**. Normalizations as in **c**, **d**, cell numbers: $n = 23$ wild-type, $n = 8$ Ki-67-KO, $n = 22$ leptomycin B. Individual Ki-67-KO curves shown in Supplementary Fig. 2. Significance was tested with two-sided unpaired *t*-test ($P = 0.28$ in GEM cell lines wild-type versus Ki-67-KO, $P = 0.12$ in L10 cell lines wild-type versus LMB-treated and $P = 0.13$ in L10 cell lines wild-type versus Ki-67-KO). Lines and shaded areas indicate mean ± s.d., dashed vertical lines indicate flavopiridol addition. Scale bars, 10 µm. Single *z*-slices are shown.

nature research

Corresponding author(s): Daniel Gerlich, Sara Cuylen-Haering

Last updated by author(s): May 23, 2020

Reporting Summary

Nature Research wishes to improve the reproducibility of the work that we publish. This form provides structure for consistency and transparency in reporting. For further information on Nature Research policies, see Authors & Referees and the Editorial Policy Checklist.

Statistics

For all statistical analyses, confirm that the following items are present in the figure legend, table legend, main text, or Methods section.

n/a	Confirmed
☐	☒ The exact sample size (*n*) for each experimental group/condition, given as a discrete number and unit of measurement
☐	☒ A statement on whether measurements were taken from distinct samples or whether the same sample was measured repeatedly
☐	☒ The statistical test(s) used AND whether they are one- or two-sided *Only common tests should be described solely by name; describe more complex techniques in the Methods section.*
☒	☐ A description of all covariates tested
☐	☒ A description of any assumptions or corrections, such as tests of normality and adjustment for multiple comparisons
☐	☒ A full description of the statistical parameters including central tendency (e.g. means) or other basic estimates (e.g. regression coefficient) AND variation (e.g. standard deviation) or associated estimates of uncertainty (e.g. confidence intervals)
☐	☒ For null hypothesis testing, the test statistic (e.g. *F*, *t*, *r*) with confidence intervals, effect sizes, degrees of freedom and *P* value noted *Give P values as exact values whenever suitable.*
☒	☐ For Bayesian analysis, information on the choice of priors and Markov chain Monte Carlo settings
☒	☐ For hierarchical and complex designs, identification of the appropriate level for tests and full reporting of outcomes
☒	☐ Estimates of effect sizes (e.g. Cohen's *d*, Pearson's *r*), indicating how they were calculated

Our web collection on statistics for biologists contains articles on many of the points above.

Software and code

Policy information about availability of computer code

Data collection	- Images/Movies: LSM780 / 880 operated by ZEN 2011 software, ImageXpressMicro XL screening microscope operated by MetaXpress software (version 5.3.05) using custom made Metamorph Macros. - Western blotting: BioRad Imager operated by Image Lab - Ribosome fractions: BioComp fraction collector operated by Triax software (version 1.28)
Data analysis	- Image analysis: Image J / FiJI (version 1.47n, 2.0.0-rc-69/1.52p and version 1.52h, 2.0.0-rc-65/1.52h), Imaris (Biplane), MATLAB, Cellcognition Explorer 1.0.5 - Data compiling, processing and normalization: Microsoft Excel (15.37 and 16.0.), R Studio (1.1.383 with R version 3.6.1) - Plots: Graph Pad Prism 7 and 8.1., R Studio (1.1.383 with R version 3.6.1)

For manuscripts utilizing custom algorithms or software that are central to the research but not yet described in published literature, software must be made available to editors/reviewers. We strongly encourage code deposition in a community repository (e.g. GitHub). See the Nature Research guidelines for submitting code & software for further information.

Data

Policy information about availability of data

All manuscripts must include a data availability statement. This statement should provide the following information, where applicable:

- Accession codes, unique identifiers, or web links for publicly available datasets
- A list of figures that have associated raw data
- A description of any restrictions on data availability

The datasets generated in this study are available from the corresponding authors upon request.

Field-specific reporting

Please select the one below that is the best fit for your research. If you are not sure, read the appropriate sections before making your selection.

☒ Life sciences ☐ Behavioural & social sciences ☐ Ecological, evolutionary & environmental sciences

For a reference copy of the document with all sections, see nature.com/documents/nr-reporting-summary-flat.pdf

Life sciences study design

All studies must disclose on these points even when the disclosure is negative.

Sample size	No sample-size calculations were performed. Sample sizes were chosen as large as possible while taking into account the experimental effort required to generate the respective data. Adequate statistics has been applied throughout the manuscript in order to make sure that the observed effects are significant given the reported sample size.
Data exclusions	These two criteria were pre-established before any analyses: - Cells that die or move out of the field of view during movie acquisition. - Cells that obviously missegregate chromosomes during movie acquisition. These two criteria were established after analyses: - Fig. 2g-i: Cells in which segmentation of kinetochores failed due to weak kinetochore signal - Fig. 4: Cells were excluded based on histone expression levels to select for a range that would allow clustering in WT and appropriate rescue in Ki-67 KO cells.
Replication	Reported experiments were repeated at least 2 times with comparable result. Unless otherwise noted, in all analyses the biological replicates have been combined.
Randomization	Not relevant as grouping was not applied.
Blinding	To minimize potential human bias, most experiments were automatically analyzed by Fiji/Matlab scripts. When manual annotation was required, blinding precautions were made. In Fig. 3c-e line profiles were drawn without knowledge of which construct was transfected.

Reporting for specific materials, systems and methods

We require information from authors about some types of materials, experimental systems and methods used in many studies. Here, indicate whether each material, system or method listed is relevant to your study. If you are not sure if a list item applies to your research, read the appropriate section before selecting a response.

Materials & experimental systems

n/a	Involved in the study
☐	☒ Antibodies
☐	☒ Eukaryotic cell lines
☒	☐ Palaeontology
☒	☐ Animals and other organisms
☒	☐ Human research participants
☒	☐ Clinical data

Methods

n/a	Involved in the study
☒	☐ ChIP-seq
☒	☐ Flow cytometry
☒	☐ MRI-based neuroimaging

Antibodies

Antibodies used	Primary antibodies: - anti-RPL10, Thermo Fisher Scientific, cat. number MA526901, clone OTI6B11, lot UD2757922A, dilution 1:2000 - BAF (A-11), Santa Cruz Biotechnology sc-166324, dilution 1:250 - anti-H3-pS10, Millipore, cat. number 05-806, lot 3236356, dilution 1:5000 - anti-acetylated H3, Millipore, cat. number 06-599, lot 3260200, dilution 1:200 - anti-H2B, Abcam, cat. number ab1790, dilution 1:1000 Secondary antibodies: - Horseradish peroxidase goat anti-mouse, Biorad, cat. number 1706516, dilution 1:5000 - Horseradish peroxidase goat anti-rabbit, Biorad, cat. number 1706515, dilution 1:5000 - goat anti-mouse Alexa Fluor 488, Molecular Probes, cat. number A11001, lot 1787787, dilution 1:1000 - goat anti-mouse Alexa Fluor 568, Molecular Probes, cat. number A11004, lot 1862187, dilution 1:1000

- anti-rabbit Alexa Fluor 594, Molecular Probes, cat. number A-11037, lot 3179197, dilution 1:500

Validation

We verified the molecular weight of the target protein by immunoblotting with extracts from HeLa cells. In addition for anti-RPL10, extracts from HeLa cells expressing a GFP-tagged transgene showed an additional band at the expected molecular weight. In addition for BAF, knocking down the protein caused loss of the band.

Eukaryotic cell lines

Policy information about cell lines

Cell line source(s)	All cells lines were derived from a HeLa Kyoto cell line obtained from S. Narumiya (Kyoto University, Japan).
Authentication	Wild-type HeLa Kyoto cells were validated by a Multiplex human Cell line Authentication test (MCA), 21.04.16
Mycoplasma contamination	Routine mycoplasma tested showed all cell lines were free of mycoplasma contamination.
Commonly misidentified lines (See ICLAC register)	HeLa cells are not in the list of commonly misidentified cell lines.

3.2. A chromatin phase transition protects mitotic chromosomes against microtubule perforation

Authors: Maximilian W. G. Schneider, Bryan A. Gibson*, Shotaro Otsuka*, Maximilian F.D. Spicer**, Mina Petrovic**, Claudia Blaukopf, Christoph Langer, Lynda K. Doolittle, Michael K. Rosen and Daniel W. Gerlich

*these authors contributed equally to this work

Status: Submitted for publishing; July, 2021

BioRxiv: https://www.biorxiv.org/content/10.1101/2021.07.05.450834v1

My contributions:

-designed, performed and analyzed experiments investigating fluorescent protein partitioning relative to mitotic chromosomes

-reading and commenting on the finished manuscript prior to submission

A chromatin phase transition protects mitotic chromosomes against microtubule perforation

Maximilian W. G. Schneider[1#], Bryan A. Gibson[2*], Shotaro Otsuka[3*], Maximilian F.D. Spicer[1], Mina Petrovic[1], Claudia Blaukopf[1], Christoph C. H. Langer[1], Lynda K. Doolittle[2], Michael K. Rosen[2], and Daniel W. Gerlich[1#]

[1]Institute of Molecular Biotechnology of the Austrian Academy of Sciences, Vienna BioCenter, Vienna, Austria
[2]Department of Biophysics and Howard Hughes Medical Institute, University of Texas Southwestern Medical Center, Dallas, USA
[3]Max Perutz Labs, a joint venture of the University of Vienna and the Medical University of Vienna, Vienna BioCenter, Vienna, Austria

*Equal contribution
#Correspondence to: maximilian.schneider@imba.oeaw.ac.at and daniel.gerlich@imba.oeaw.ac.at

Dividing eukaryotic cells package extremely long chromosomal DNA molecules into discrete bodies to enable microtubule-mediated transport of one genome copy to each of the newly forming daughter cells[1–3]. Assembly of mitotic chromosomes involves DNA looping by condensin[4–8] and chromatin compaction by global histone deacetylation[9–13]. While condensin confers mechanical resistance towards spindle pulling forces[14–16], it is not known how histone deacetylation affects material properties and segregation mechanics of mitotic chromosomes. Here, we show how global histone deacetylation at the onset of mitosis induces a chromatin-intrinsic phase transition that endows chromosomes with specific characteristics necessary for their precise movement during cellular division. Deacetylation-mediated compaction of chromatin forms a structure dense in negative charge and allows mitotic chromosomes to resist perforation by microtubules as they are pushed to the metaphase plate. Hyperacetylated mitotic chromosomes lack a defined surface boundary, are frequently perforated by microtubules, and are prone to missegregation. Our study highlights the different contributions of DNA loop formation and chromatin-intrinsic phase separation to genome segregation in dividing cells.

The material properties of individual cell components play a key role in the dynamic organization and reorganization of cellular structure. In mitotic vertebrate cells, chromosomes must acquire material properties that enable microtubules to move them, first to the spindle center during prometaphase and then to the spindle poles during anaphase[1,17]. Pulling forces are generated by microtubules that attach to small chromosomal regions termed kinetochores[18], whereas pushing forces, known as polar ejection forces, are produced by microtubules contacting chromosome arms[19–23]. Condensin confers mitotic chromosomes with the mechanical stability required to withstand pulling forces[14–16], but it remains unclear how chromosomes resist pushing forces. These material properties must also provide chromosome arms with resistance to penetration by polymerizing microtubule tips, since entanglements occurring due to growth of microtubules into the mass of chromatin would lead to impaired segregation.

Acetylation-regulated chromatin compaction prevents microtubule perforation.

To investigate the relationship between the material properties of chromosomes and the forces exerted upon them by the mitotic spindle, we first sought to uncouple the mechanisms responsible for providing resistance to pushing and pulling forces. Given its well described role in resisting pulling forces[14–16], we first investigated the effect of condensin depletion on the morphology and movement of mitotic chromosomes in live HeLa cells. To deplete condensin, we modified all endogenous alleles of its essential SMC4 subunit with a C-terminal auxin−inducible degron (mAID) and HaloTag for visualization and added the auxin analog 5-PhIAA[24] 2.5 h prior to mitotic entry to induce efficient degradation (Extended Data Fig. 1a-c). We visualized the spindle with silicon-rhodamine (SiR)-tubulin[25] and stained DNA with Hoechst to determine the position of chromosomes. In condensin-depleted cells, we observed an unstructured mass of compact chromatin forming a plate between the spindle poles (Fig. 1a, b), indicating that polar ejection forces efficiently push bulk chromatin towards the spindle center. Immunofluorescence staining of the kinetochore marker CENP-A and the spindle pole component pericentrin further showed that many kinetochores were detached from the bulk mass of chromatin and displaced towards the spindle poles, whereas in control cells all kinetochores were closely linked with chromosomes at the metaphase plate (Extended Data Fig. 1d). The movement of loosely connected kinetochores towards the spindle poles confirms that condensin is required for chromosomes to resist pulling forces. Thus, condensin depletion allows the mechanisms responsible for the resistance to pushing and pulling forces to be uncoupled.

The observation that bulk chromatin remains responsive to polar ejection forces following depletion of condensin suggests that under these conditions resistance to pushing forces might arise from nucleosome-mediated interactions in the chromatin fiber. Nucleosomal interactions are thought to increase when histones are deacetylated during mitotic entry (Extended Data Fig. 2a, b), contributing to global chromatin compaction[9–11,26]. To investigate how acetylation affects the

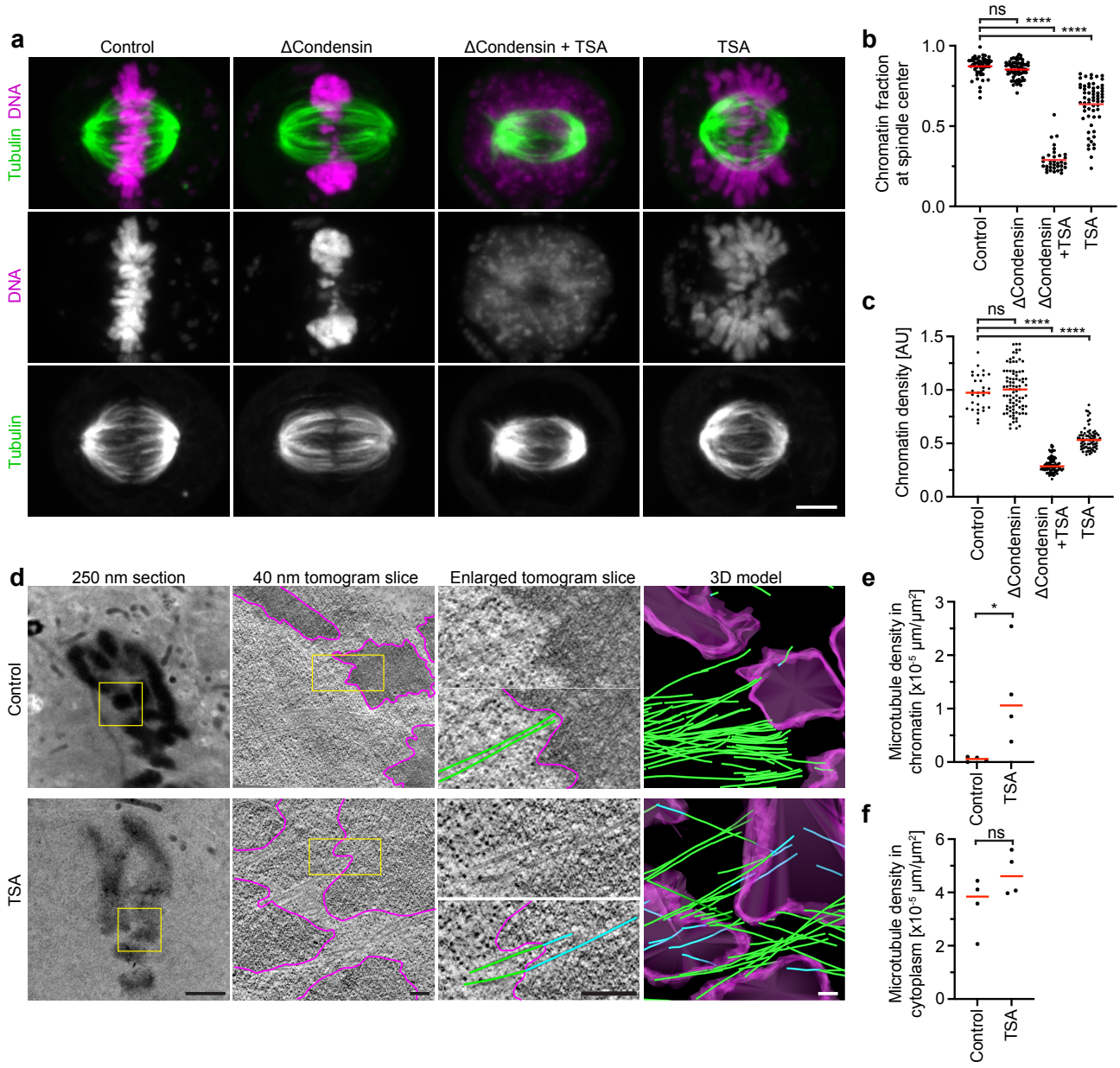

Figure 1. Acetylation-regulated chromatin compaction prevents microtubule perforation in mitosis. **a**, Contribution of condensin and histone deacetylases to mitotic chromosome compaction and congression to the spindle center. HeLa cells with homozygously mAID-tagged SMC4 were treated with 5-PhIAA to deplete condensin (ΔCondensin) or with TSA to suppress mitotic histone deacetylation as indicated. Live cell images with microtubules stained by SiR-tubulin; DNA stained by Hoechst. Projection of 5 Z-sections. **b**, Quantification of chromosome congression by the fraction of chromatin localizing to the central spindle region. *n*=51 cells for control, *n*=65 for ΔCondensin, *n*=34 for ΔCondensin+TSA, *n*=61 for TSA. Bars indicate mean; significance was tested by an unpaired, two-tailed *t*-test (ΔCondensin, *P*=0.06) or a two-tailed Mann-Whitney test (ΔCondensin+TSA, $P<10^{-15}$); TSA, $P<10^{-15}$). **c**, Quantification of chromatin density in cells treated as in **a**. *n*=31 cells for control, *n*=89 for ΔCondensin, *n*=99 for ΔCondensin+TSA, *n*=74 for TSA. Bars indicate mean; significance was tested by an unpaired, two-tailed *t*-test (ΔCondensin, *P*=0.816) or a Kolmogorov-Smirnov test (ΔCondensin+TSA, $P<10^{-15}$; TSA, $P<10^{-15}$). **d**, Electron tomography of wildtype prometaphase HeLa cells in the absence or presence of TSA. **e, f**, Quantification of microtubule density in chromatin and cytoplasmic regions as shown in **d**. *n*=4 tomograms from 3 cells for each condition. Bars indicate mean; significances were tested by a two-tailed Mann-Whitney test (**e,** *P*=0.029; *P*=0.343). Scale bars, **a**, 5 µm, **d**, 250 nm section, 2 µm, tomogram slices, 200 nm.

movement of bulk chromatin, we treated condensin-depleted cells with the pan histone deacetylase inhibitor trichostatin A (TSA)[27] to induce broad hyperacetylation of histone lysine residues (Extended Data Fig. 2c, d). The hyperacetylated chromatin of condensin-depleted mitotic cells did not compact or concentrate at the spindle center but instead dispersed throughout the cytoplasm, such that spindle pole regions were no longer clear of chromatin (Fig. 1a, b; Extended Data Fig. 1d; 2e, f). A complementary approach to induce histone hyperacetylation by overexpressing the histone acetyltransferase p300[28] resulted in consistent chromatin decompaction and congression phenotypes (Extended Data Fig. 3). Thus, histone deacetylation appears to be important for spindle-mediated pushing of bulk chromatin towards the spindle center.

The chromatin decompaction induced by TSA in condensin-depleted cells appeared much more pronounced than previously observed in wildtype cells[9,10]. We hypothesized that this might be due to condensin-mediated linkages that counteract the dispersion of chromatin fibers. To

investigate this, we analyzed how TSA affects chromatin density in the presence or absence of condensin. In condensin-depleted mitotic cells, TSA reduced chromatin density to 29% compared to cells that were not treated with TSA, whereas in the presence of condensin it reduced chromatin density only to 53% (Fig. 1a, c). Condensin depletion alone did not reduce mitotic chromatin density (Fig. 1a, c), consistent with previous observations[14,29,30]. Thus, histone deacetylation is necessary and sufficient for complete compaction of mitotic chromatin even in the absence of condensin. In contrast, condensin is neither necessary nor sufficient for complete chromatin compaction during mitosis, yet it can concentrate chromatin to some extent even when histones are hyperacetylated. These observations support a model describing mitotic chromosomes as a hydrogel[31–34], in which a flexible chromatin fiber is linked by condensin to form a network, wherein the degree of compaction is controlled by acetylation-regulated interactions between nucleosomes, resulting in changes in fiber solubility.

The hydrogel model explains how condensin linkages confer resistance to pulling forces[14–16]. Histone deacetylation appears to be dispensable for resistance against pulling forces[35], yet a potential role in facilitating microtubule-based pushing has not been investigated. We hypothesized that resistance to pushing forces depends first on the ability to prevent microtubules penetrating chromosomes, which might require compaction of a swollen interphase chromatin hydrogel via histone deacetylation during mitotic entry. To test how acetylation affects access of microtubules to chromosomes, we performed electron tomography of mitotic HeLa cells. Chromosomes of unperturbed cells appeared as homogeneously compacted bodies with a sharp surface boundary, and 3D segmentation showed that they were almost never penetrated by microtubules (Fig. 1d, e). In contrast, chromosomes of TSA-treated cells appeared less compact, particularly towards the periphery, and microtubules grew extensively through the chromatin (Fig. 1d-f). Thus, active histone deacetylases are required to keep microtubules out of chromosome bodies, providing a basis for resistance towards pushing forces.

Microtubule perforation into mitotic chromosomes is expected to cause entanglements between chromatin fiber loops and spindle microtubules that impair chromosome segregation. To investigate how TSA-induced hyperacetylation affects chromosome movements in mitosis, we recorded time-lapse movies of HeLa cells expressing H2B-mCherry. TSA severely delayed chromosome congression and initiation of anaphase and caused a high incidence of lagging chromosomes (Extended Data Fig. 1e-g). Active histone deacetylases are thus essential for faithful chromosome segregation.

Acetylation controls chromatin solubility in cytoplasm

To elucidate the mechanism underlying microtubule exclusion from mitotic chromosomes, we investigated how histone acetylation affects the material properties of chromatin. Both intact mitotic chromosomes[9,11] and intrinsic chromatin condensates formed from small fragments of chromatin[13] exhibit structural sensitivity to histone hyperacetylation. We reasoned, in accordance with principles from polymer chemistry[36], that the hydrogel material of mitotic chromosomes that resists microtubule perforation might arise as a consequence of intrinsic chromatin phase separation at the very long length scale of human chromosomes.

To investigate the phase separation behavior of mitotic chromatin at smaller length scales, we fragmented chromosomes in live mitotic HeLa cells by microinjecting the restriction enzyme AluI. Shortly after microinjection of AluI, chromosomes lost their elongated shape, forming round condensates that fused to one another, indicating a liquid state (Fig. 2a). Remarkably, the digestion of chromatin did not decrease chromatin density (Fig. 2b), demonstrating that integrity of the chromatin fiber is not required for full compaction of mitotic chromatin. At macroscopic scales, phase-separating systems become less dynamic when composed of long molecules due to steric effects and length-dependent changes in valency. Consistent with this intrinsic behavior, without AluI digestion H2B-mCherry fluorescence recovers very little after photobleaching, whereas mitotic chromatin condensates that form following AluI digestion recover rapidly from photobleaching (Fig. 2c, d). Thus, mitotic chromatin is insoluble in cytoplasm, and when the long-range constraints of the fiber are eliminated, the short-range dynamics manifest in liquid-like behavior.

Intrinsic chromatin condensates dissolve following hyperacetylation[13]. To test whether acetylation also suppresses phase separation of mitotic chromosomes, we treated cells with TSA prior to mitotic entry and then microinjected AluI. This resulted in homogeneously dispersed chromatin fragments with almost no local condensates (Fig. 2e, f). In contrast, degradation of SMC4 had no effect on chromatin droplet formation after AluI-mediated fragmentation, indicating that condensins are not required to form an insoluble chromatin phase (Extended Data Fig. 4a, b). Thus, deacetylation is a major factor in establishing an immiscible chromatin phase in mitotic cells.

The observed differences in chromatin solubility might be due to variable efficiency of AluI-mediated DNA digestion in interphase or mitotic cells. To address this possibility, we used time-lapse microscopy to investigate whether chromatin fragments generated in interphase nuclei undergo a solubility phase transition upon progression to mitosis. To monitor cell cycle stages, we used a fluorescence resonance energy transfer (FRET) biosensor for a key mitotic kinase, Aurora B[37]. As chromosome fragmentation blocks mitotic entry owing to DNA damage signaling, we applied chemical inhibitors to induce an interphase-to-mitosis transition: we first synchronized cells to G2 using the Cdk1 inhibitor RO3306[38] and then induced a mitosis-like state by removing RO3306 for Cdk1 activation and simultaneously inhibiting counteracting PP2A and PP1 phosphatases using Okadaic acid. Mitotic entry was demonstrated by the Aurora B FRET biosensor signal (Fig. 2g, h). Injection of AluI into G2 cell nuclei resulted in homogeneously distributed chromatin, consistent with a soluble state (Fig. 2h, i). Upon induction of mitosis, chromatin fragments formed spherical condensates that were as dense as intact chromosomes (Fig. 2h-j), whereas control cells in which RO3306 was not replaced by Okadaic acid maintained homogeneously dissolved chromatin fragments (Extended Data Fig. 4c d). These observations support a model in which a global reduction in chromatin solubility drives volume compaction at the interphase-to-mitosis transition.

To determine whether the loss of chromatin solubility upon mitotic entry depends on deacetylation, we inhibited histone deacetylases using TSA before injecting AluI into G2-synchronized cells. As in control cells, chromatin fragments homogeneously distributed throughout the nucleus in G2, but mitotic induction did not lead to the formation of condensed foci (Fig. 2k, l). Thus, active histone deacetylases are essential

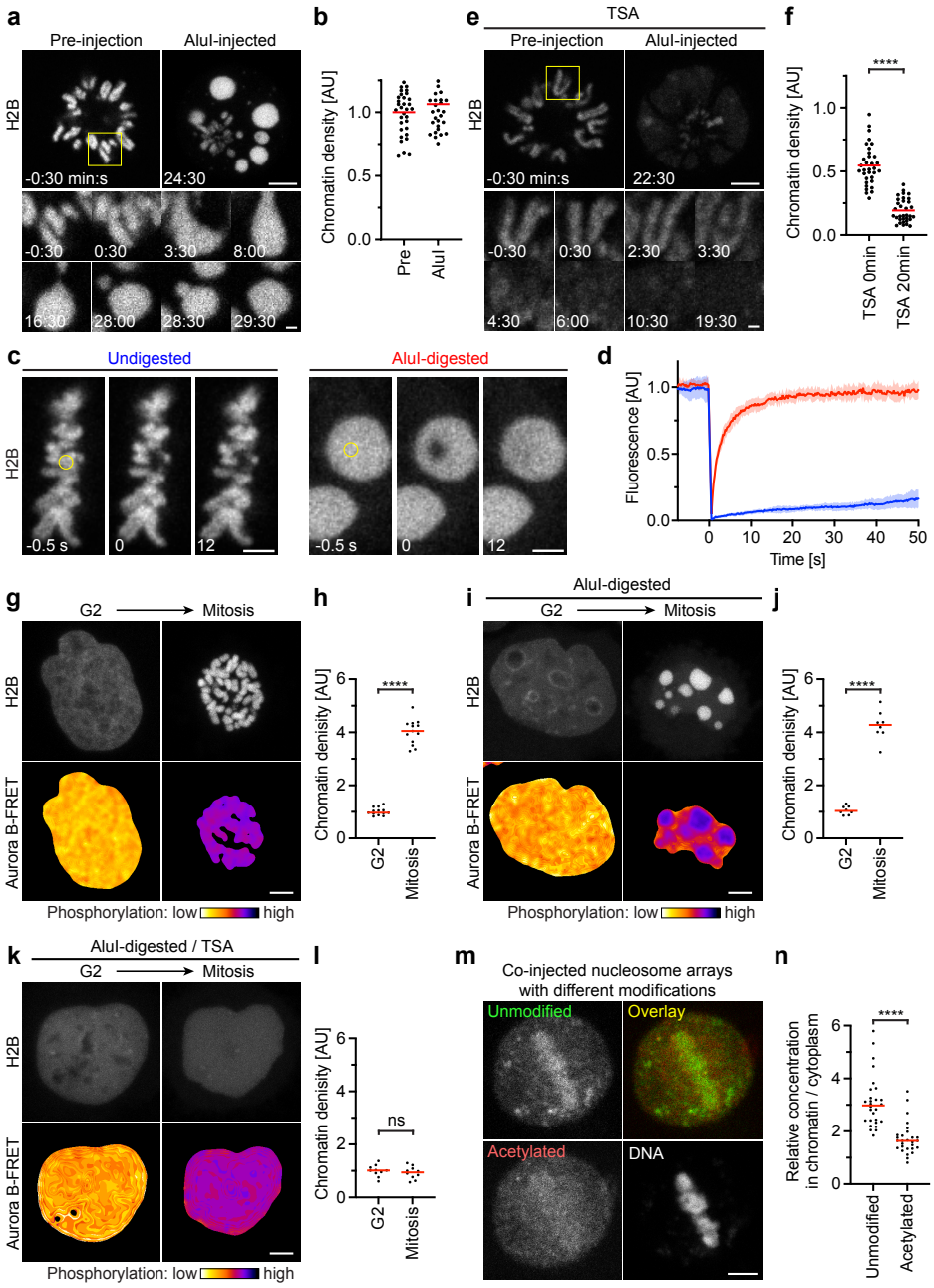

Figure 2. Acetylation regulates chromatin solubility in mitotic cytoplasm. a, Chromosome fragmentation in live mitotic HeLa cell by AluI injection during time-lapse microscopy. Chromatin was visualized with H2B-mCherry. AluI was injected at t=0 min. Projection of 3 Z-sections. **b**, Quantification of chromatin density before and after injection of AluI as in **a**. *n*=11 cells, 3 ROIs each. Significance tested by a paired, two-tailed *t*-test (*P*=0.013). **c**, Chromatin mobility in undigested metaphase chromosomes and after AluI injection, measured by fluorescence recovery after photobleaching in live metaphase cells expressing H2B-mCherry. Circles indicate photobleaching region at t=0 s. **d**, Quantification of fluorescence before and after photobleaching in *n*=8 (undigested) or *n*=10 (AluI-digested) cells as in **c**. **e**, AluI injection (t=0 min) during time-lapse microscopy as in **a**, but for a TSA-treated mitotic cell. **f**, Quantification of chromatin density as in **b,** normalized to the mean of untreated pre-injection cells shown in **b**. *n*=11 cells, 3 ROIs each. **g**, Chemical induction of G2-to-mitosis transition. HeLa cell expressing Aurora B-FRET biosensor was synchronized to G2 by RO3306 and then induced to enter mitosis by removing RO3306 and adding okadaic acid (OA). Mitotic entry was detected by chromosome compaction and FRET signal. Projection of 9 Z-sections. **h**, Quantification of chromatin density in G2 and mitosis as in **g** for *n*=13 cells. Bars indicate mean; significance was tested by a paired, two-tailed *t*-test ($P=5.535\times10^{-12}$). **i**, Chromatin was fragmented in G2 cells by injection of AluI and mitosis was subsequently induced as in **g**. Projection of 9 Z-sections. **j**, Quantification of chromatin density in G2 and mitosis as in **i** for *n*=8 cells. Bars indicate mean; significance was tested by a paired, two-tailed *t*-test ($P=1.766\times10^{-7}$). **k**, Chromatin was fragmented in TSA-treated G2 cells by injection of AluI and mitosis was subsequently induced as in **g**. Projection of 9 Z-sections. **l.** Quantification of chromatin density in G2 and mitosis as in **k** for *n*=10 cells. Bars indicate mean; significance was tested by a paired, two-tailed *t*-test (*P*=0.093). **m**, Microinjection of synthetic nucleosome arrays that were either untreated or pre-incubated with p300 acetyltransferase into live mitotic cells, for *n*=28 cells. Unmodified and acetylated nucleosome arrays were labelled by distinct fluorescent dyes. DNA was counterstained with DAPI. Bars indicate mean; significance was tested by a two-tailed Mann-Whitney test ($P=1.645\times10^{-9}$). Scale bars, **a**,**e**,**g**,**l**,**k**,**m**, 5 µm, insert 1 µm; **c**, 3 µm.

to form an immiscible chromatin phase upon mitotic entry.

Acetylation of chromatin might regulate solubility in cytoplasm directly or via other chromatin-associated components. To assess the effect of histone acetylation on chromatin solubility more specifically, we used synthetic nucleosome arrays[13] as probes. We generated fluorescently labelled arrays of 12 unmodified naive nucleosomes as well as similar arrays that were labelled with a distinct fluorophore and acetylated *in vitro* with recombinant p300 acetyltransferase. In vitro, the unmodified nucleosome arrays form liquid condensates under physiological salt concentrations, in contrast to the acetylated nucleosome arrays (Extended Data Fig. 4e, f)[13]. Following co-injection of these nucleosome arrays into live mitotic cells, unmodified arrays almost completely partitioned into the mitotic chromatin phase, whereas acetylated nucleosome arrays predominantly dissolved in the cytoplasm (Fig. 2m, n). Thus, histone acetylation is a direct regulator of chromatin solubility in cytoplasm. Overall, these results indicate that mitotic chromatin is a hydrogel in which condensin connects DNA loops and acetylation regulates chromatin solubility to mediate global compaction and formation of a sharp surface boundary.

Chromatin condensates exclude negatively charged macromolecules

One explanation for how the immiscible mitotic chromatin phase acts as a barrier to microtubule penetration could be that it excludes cytoplasmic tubulin dimers and thereby limits microtubule growth at the cytoplasm-chromosome boundary. To investigate how soluble tubulin partitions relative to mitotic chromatin, we therefore microinjected fluorescently labelled tubulin into live mitotic cells and applied nocodazole to suppress microtubule polymerization (Fig. 3a). Soluble tubulin was much less concentrated inside mitotic chromosomes compared to the surrounding cytoplasm (Fig. 3a, b). In contrast, soluble tubulin was not excluded from hyperacetylated chromosomes in TSA-treated cells (Fig. 3a, b). Thus, the immiscible chromatin compartment formed by deacetylated mitotic chromatin excludes soluble tubulin.

To determine whether exclusion of tubulin is due to a limiting pore size in chromosomes, we expressed DsRed, a fluorescent protein that forms tetramers slightly larger than tubulin dimers[39,40]. In stark contrast to tubulin, DsRed distributed evenly across chromatin and cytoplasm (Fig. 3c, d). Thus, macromolecules in the size range of tubulin are not generally excluded from mitotic chromatin.

The selective exclusion of tubulin but not DsRed from mitotic chromatin suggests that specific molecular features control access. Tubulin is highly negatively charged at physiological pH (7.2), in contrast to near-neutrally charged DsRed, raising the possibility that macromolecular access is governed by electrostatic interactions. A high concentration of an overall negative electrical charge of chromatin[41] in an immiscible condensate might therefore repel negatively charged cytoplasmic proteins. To investigate how electrical charge affects macromolecular access to mitotic chromatin, we fused charged polypeptides to the N-terminus of DsRed. DsRed fused to a negatively charged polypeptide (overall predicted charge on tetramer: -7e) was excluded from mitotic chromatin, whereas DsRed fused to a positively charged polypeptide (overall charge on tetramer: +9e) concentrated inside chromatin (Fig. 3c, d). Consistent with this observation, we found negatively charged mEGFP or dextrans were also excluded from mitotic chromosomes, whereas a positively charged surface mutant scGFP (super-charged GFP, +7e)[42] or positively charged dextrans concentrated in mitotic chromosomes (Extended Data. Fig. 5a-d). Thus, electrical charge is a key determinant of macromolecular access to mitotic chromatin.

The exclusion of negatively charged macromolecules from mitotic chromosomes might be mediated by insoluble nucleosome fibers alone or it might involve other chromosome-associated factors. To investigate how tubulin interacts with pure chromatin condensates, we reconstituted droplets of recombinant nucleosome arrays *in vitro*[13] and then added rhodamine-labelled tubulin in the presence of nocodazole. Soluble tubulin was indeed efficiently excluded from nucleosome array condensates (Fig. 3e, f). Consistent with this observation, negatively charged mEGFP or dextrans were also excluded from nucleosome array condensates, whereas a positively charged scGFP mutant or positively charged dextrans concentrated in nucleosome array condensates (Extended Data Fig. 5e-h). The exclusion of negatively charged macromolecules, including tubulin, is thus an intrinsic property of condensed nucleosome fibers.

The efficient exclusion of free tubulin suggests that weak affinity interactions in liquid chromatin condensates might be sufficient to limit microtubule polymerization. To investigate how microtubules interact with reconstituted chromatin droplets *in vitro*, we added purified tubulin and then induced microtubule polymerization by increasing the temperature. Microtubules formed a dense microtubule network, yet they almost never grew into chromatin condensates (Fig. 3e, f). Thus, chromatin-intrinsic material properties impose a highly impermeable barrier to microtubule polymerization independently of condensin or other chromosome-associated factors.

Microtubules push liquid chromatin condensates

Microtubule polymerization exerts substantial pushing forces upon contact with stiff surfaces[43]. If the surface tension of the immiscible chromatin phase were strong enough to resist microtubule polymerization, then droplets of digested chromosomes should be pushed away by growing astral microtubules. To test this hypothesis, we injected AluI into mitotic cells treated with nocodazole and then washed out nocodazole to induce microtubule polymerization. We further applied S-trityl-L-cysteine (STLC)[44] to maintain a monopolar astral spindle geometry. Time-lapse imaging showed that initially all chromatin resided in a single droplet at the cell center, but soon after nocodazole washout the chromatin split into several droplets that moved away from growing microtubule asters (Extended Data Fig. 6a, b). Thus, liquid chromatin condensates can be pushed by polymerizing astral microtubules.

Astral microtubules might directly push on chromatin droplets by polymerizing against the chromatin phase boundary or they might couple to chromatin via chromokinesins[19–21,45–47,23,22,48]. To investigate how the spindle moves chromatin droplets, we used RNAi to co-deplete two chromokinesins that are major contributors to the polar ejection force, Kid and Kif4a[45,47,23,22,48] (Extended Data Fig. 6c-e). Following AluI-injection and nocodazole washout in the presence of STLC, chromosome droplets moved to the chromosome periphery as efficiently as in control cells (Extended Data Fig. 6c, d). Thus, spindle asters can move liquid chromatin independently of chromokinesins Kid and Kif4a, potentially by polymerizing microtubules pushing against the chromatin phase boundary.

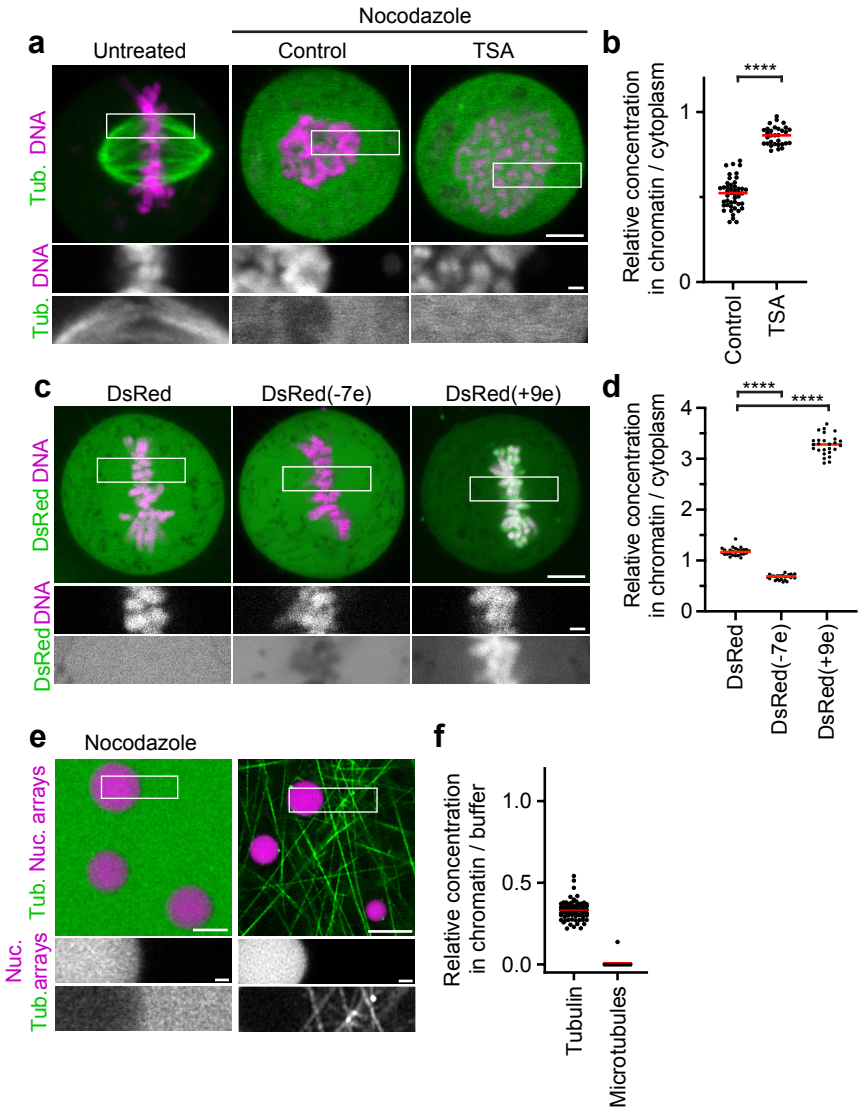

Figure 3. Chromatin condensates limit access of tubulin and other negatively charged macromolecules. a, Localization of tubulin relative to mitotic chromosomes. Rhodamine-labelled tubulin was injected into live mitotic cells that were either untreated, treated with nocodazole alone (Control) or in combination with TSA. **b**, Quantification of tubulin concentration for data shown in **a**. *n*=27 cells. Bars indicate mean; significance was tested by a two-tailed Welch *t*-test ($P<1x10^{-15}$). **c**, Live cell images of HeLa cell expressing DsRed or DsRed fused at its N-terminus to electrically charged polypeptides. DNA stained with Hoechst. Numbers in brackets indicate predicted elementary charge of tetramers formed by DsRed fusion constructs. **d**, Quantification of DsRed concentration for data shown in **c**. *n*=26 cells (DsRed), *n*=26 (DsRed-7e), *n*=26 (DsRed+9e). Bars indicate mean; significances were tested by a two-tailed Welch *t*-test (DsRed(-7e), $P<1x10^{-15}$; DsRed(+9e) $P<1x10^{-15}$). **e**, Localization of tubulin relative to reconstituted nucleosome array droplets. Nucleosome array droplets were formed by incubation in phase separation buffer and fluorescently labelled tubulin was then added in the presence of nocodazole, or in the absence of nocodazole with subsequent temperature increase to 20 degrees to induce microtubule polymerization. **f**, Quantification of tubulin concentration or microtubule density in nucleosome array condensates relative to buffer for data shown in **e**. *n*=94 droplets, *n*=13 field of polymerized microtubules. Bars indicate mean. Scale bars, 5 µm, insert 1 µm.

Microtubule pushing on chromosome arms is counteracted by microtubule pulling at centromeres. To investigate how liquified chromatin responds to pulling forces at kinetochores, we injected AluI into cells expressing EGFP-tagged centromere-specific histone 3 variant CENP-A together with H2B-mCherry, in the presence of nocodazole. We then removed nocodazole to induce monopolar spindle assembly in the presence of STLC. The bulk mass of chromatin, visualized with H2B-mCherry, rapidly moved towards the cell periphery, while several much smaller chromatin condensates enriched in EGFP-CENP-A remained close to the spindle monopole (Fig. 4a, b). Thus, bulk chromatin is pushed by microtubules, while centromeres are transported towards the spindle pole. In cells after chromatin digestion, where the continuous connection between centromere and the remaining chromosome is lost, bulk chromatin and centromeric chromatin physically separate according to the locally dominating forces.

Conclusions

Here, we show that a sharp global reduction in chromatin solubility converts chromosomes into phase-separated bodies during mitosis (Fig. 4c). The immiscible mitotic chromatin forms a surface dense in negative charge that prevents microtubule perforation and provides resistance to pushing

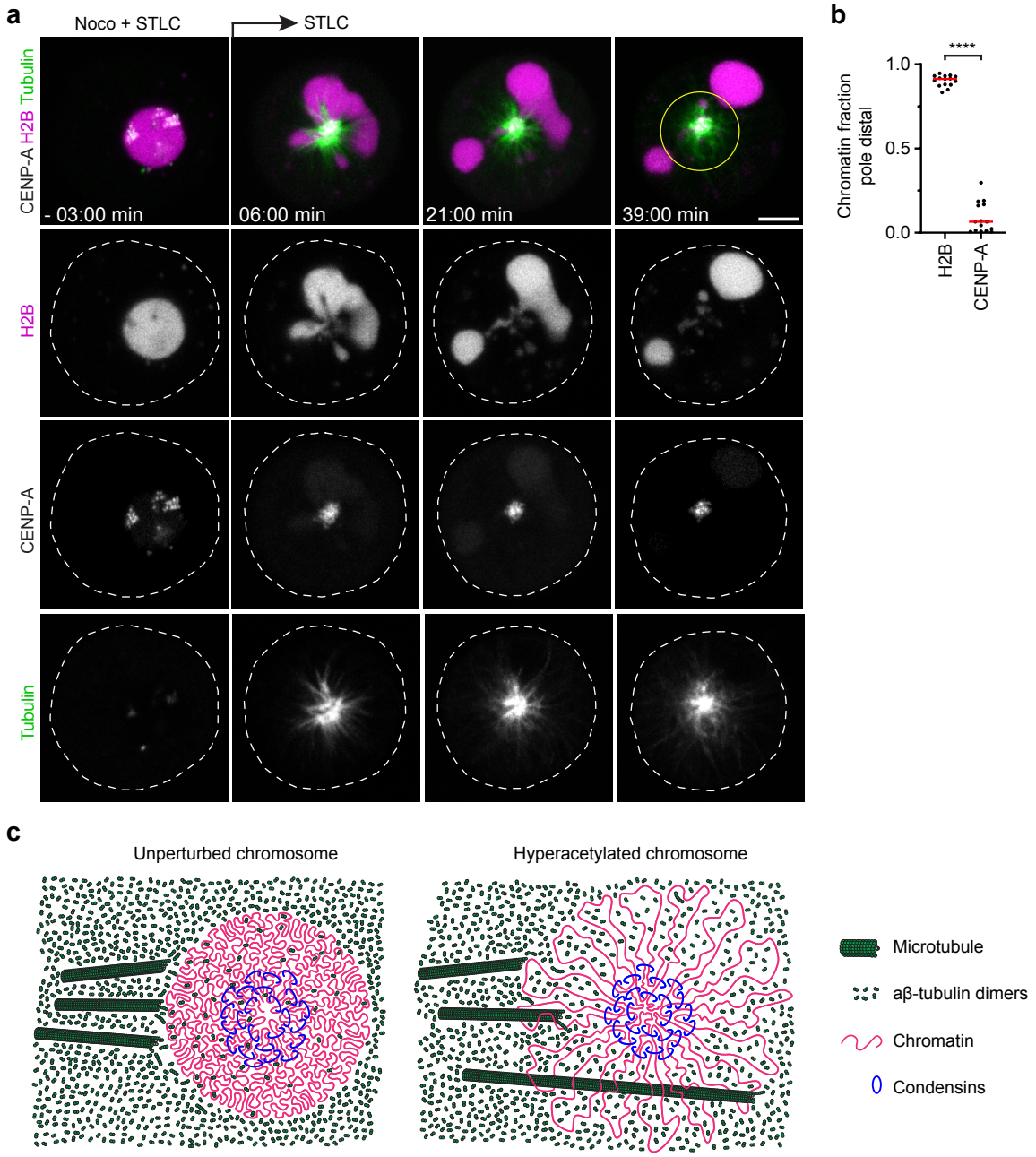

Figure 4. Microtubules push liquified chromatin away from the spindle pole. a, Time-lapse microscopy of liquified chromatin during monopolar spindle assembly. AluI was injected into live mitotic HeLa cells expressing H2B-mCherry and mEGFP-CENP-A, stained with SiR-tubulin, in the presence of nocodazole and STLC. Nocodazole was then removed at t=0 min during time-lapse imaging to induce monopolar spindle assembly. Projection of 5 Z-sections. **b**, Quantification of bulk chromatin (H2B-mCherry) and centromeric chromatin (mEGFP-CENP-A) localizing at the cell periphery relative to the region around the spindle monopole at t=36 min. *n*=15 cells. Bars indicate mean; significance was tested by a two-tailed Welch *t*-test ($P<1x10^{-15}$). **c**, Model of chromatin compaction and condensin-mediated DNA looping in mitotic chromosome and spindle assembly. Scale bars, 5 µm.

forces while allowing chromatin fiber sliding internally, as required for continuous dynamic loop formation by condensin[6,14,49]. In parallel, condensin-mediated linkages establish a hydrogel that withstands pulling forces[14–16]. Jointly, these molecular activities shape discrete chromosome bodies with a defined surface despite continuous internal remodeling of the chromatin fiber.

Our results show that mitotic cells contain three principal domains with distinct microtubule polymerization propensity: the centrosome matrix, which concentrates soluble tubulin to promote nucleation at the poles[50]; the cytoplasm, which is highly permissive for microtubule growth and amplification; and a chromatin compartment that resists microtubule growth by exclusion of soluble tubulin and formation of a mechanical barrier towards polymerization. Our study thus provides a unified view of how chromatin looping by condensin and compaction through a volume phase transition contribute to the material properties and mechanical functions of mitotic chromosomes.

References

1. Batty, P. & Gerlich, D. W. Mitotic Chromosome Mechanics: How Cells Segregate Their Genome. *Trends in Cell Biology* **29**, 717–726 (2019).
2. Kschonsak, M. & Haering, C. H. Shaping mitotic chromosomes: From classical concepts to molecular mechanisms. *BioEssays : news and reviews in molecular, cellular and developmental biology* **37**, 755–766 (2015).
3. Ohta, S., Wood, L., Bukowski-Wills, J.-C., Rappsilber, J. & Earnshaw, W. C. Building mitotic chromosomes. *Current Opinion In Cell Biology* **23**, 114–121 (2011).
4. Hirano, T. & Kobayashi, R. Condensins, Chromosome Condensation Protein Complexes Containing XCAP-C, XCAP-E and a Xenopus Homolog of the Drosophila Barren Protein. *Cell* **89**, 511–521 (1997).
5. Shintomi, K., Takahashi, T. S. & Hirano, T. Reconstitution of mitotic chromatids with a minimum set of purified factors. *Nature Cell Biology* **17**, 1014–1023 (2015).
6. Ganji, M. *et al.* Real-time imaging of DNA loop extrusion by condensin. *Science (New York, NY)* eaar7831 (2018).
7. Gibcus, J. H. *et al.* A pathway for mitotic chromosome formation. *Science* **359**, eaao6135 (2018).
8. Yatskevich, S., Rhodes, J. & Nasmyth, K. Organization of Chromosomal DNA by SMC Complexes. *Annual Review of Genetics* **53**, annurev-genet-112618-043633 (2019).
9. Cimini, D., Mattiuzzo, M., Torosantucci, L. & Degrassi, F. Histone hyperacetylation in mitosis prevents sister chromatid separation and produces chromosome segregation defects. *Molecular biology of the cell* **14**, 3821–3833 (2003).
10. Kruhlak, M. J. *et al.* Regulation of global acetylation in mitosis through loss of histone acetyltransferases and deacetylases from chromatin. *The Journal of biological chemistry* **276**, 38307–38319 (2001).
11. Wilkins, B. J. *et al.* A cascade of histone modifications induces chromatin condensation in mitosis. *Science (New York, NY)* **343**, 77–80 (2014).
12. Zhiteneva, A. *et al.* Mitotic post-translational modifications of histones promote chromatin compaction in vitro. *Open biology* **7**, 170076 (2017).
13. Gibson, B. A. *et al.* Organization of Chromatin by Intrinsic and Regulated Phase Separation. *Cell* **179**, 470-484.e21 (2019).
14. Gerlich, D., Hirota, T., Koch, B., Peters, J. M. & Ellenberg, J. Condensin I stabilizes chromosomes mechanically through a dynamic interaction in live cells. *Current Biology* **16**, 333–344 (2006).
15. Houlard, M. *et al.* Condensin confers the longitudinal rigidity of chromosomes. *Nature Cell Biology* **17**, 771–781 (2015).
16. Sun, M., Biggs, R., Hornick, J. & Marko, J. F. Condensin controls mitotic chromosome stiffness and stability without forming a structurally contiguous scaffold. *Chromosome research : an international journal on the molecular, supramolecular and evolutionary aspects of chromosome biology* **26**, 277–295 (2018).
17. Oriola, D., Needleman, D. J. & Brugués, J. The Physics of the Metaphase Spindle. *Annual Reviews of Biophysics* **47**, 655–673 (2018).
18. Monda, J. K. & Cheeseman, I. M. The kinetochore-microtubule interface at a glance. *Journal Of Cell Science* **131**, jcs214577 (2018).
19. Rieder, C. L., Davison, E. A., Jensen, L. C., Cassimeris, L. & Salmon, E. D. Oscillatory movements of monooriented chromosomes and their position relative to the spindle pole result from the ejection properties of the aster and half-spindle. *The Journal of cell biology* **103**, 581–591 (1986).
20. Ault, J. G., DeMarco, A. J., Salmon, E. D. & Rieder, C. L. Studies on the ejection properties of asters: astral microtubule turnover influences the oscillatory behavior and positioning of mono-oriented chromosomes. *J Cell Sci* **99 (Pt 4)**, 701–710 (1991).
21. Rieder, C. L. & Salmon, E. D. Motile kinetochores and polar ejection forces dictate chromosome position on the vertebrate mitotic spindle. *The Journal of cell biology* **124**, 223–233 (1994).
22. Maiato, H., Gomes, A. M., Sousa, F. & Barisic, M. Mechanisms of Chromosome Congression during Mitosis. *Biology* **6**, 13 (2017).
23. Barisic, M., Aguiar, P., Geley, S. & Maiato, H. Kinetochore motors drive congression of peripheral polar chromosomes by overcoming random arm-ejection forces. *Nature Cell Biology* **16**, 1249–1256 (2014).
24. Yesbolatova, A. *et al.* The auxin-inducible degron 2 technology provides sharp degradation control in yeast, mammalian cells, and mice. *Nature Communications* **11**, 5701 (2020).
25. Lukinavičius, G. *et al.* Fluorogenic probes for live-cell imaging of the cytoskeleton. *Nature Methods* **11**, 731–733 (2014).
26. Ginno, P. A., Burger, L., Seebacher, J., Iesmantavicius, V. & Schübeler, D. Cell cycle-resolved chromatin proteomics reveals the extent of mitotic preservation of the genomic regulatory landscape. *Nature communications* **9**, 4012–4048 (2018).
27. Yoshida, M., Kijima, M., Akita, M. & Beppu, T. Potent and specific inhibition of mammalian histone deacetylase both in vivo and in vitro by trichostatin A. *The Journal of biological chemistry* **265**, 17174–17179 (1990).
28. Ogryzko, V. V., Schiltz, R. L., Russanova, V., Howard, B. H. & Nakatani, Y. The Transcriptional Coactivators p300 and CBP Are Histone Acetyltransferases. *Cell* **87**, 953–959 (1996).
29. Hudson, D. F., Vagnarelli, P., Gassmann, R. & Earnshaw, W. C. Condensin is required for nonhistone protein assembly and structural integrity of vertebrate mitotic chromosomes. *Developmental cell* **5**, 323–336 (2003).
30. Samejima, K. *et al.* Functional analysis after rapid degradation of condensins and 3D-EM reveals chromatin volume is uncoupled from chromosome architecture in mitosis. *Journal Of Cell Science* **131**, jcs210187 (2018).
31. Marko, J. F. & Siggia, E. D. Polymer models of meiotic and mitotic chromosomes. *Molecular biology of the cell* **8**, 2217–2231 (1997).
32. Poirier, M. G. & Marko, J. F. Mitotic chromosomes are chromatin networks without a mechanically contiguous protein scaffold. *Proceedings of the National Academy of Sciences of the United States of America* **99**, 15393–15397 (2002).
33. Poirier, M. G., Monhait, T. & Marko, J. F. Reversible hypercondensation and decondensation of mitotic chromosomes studied using combined chemical–micromechanical techniques. *Journal of cellular biochemistry* **85**, 422–434 (2002).
34. Cuylen, S., Metz, J. & Haering, C. H. Condensin structures chromosomal DNA through topological links. *Nature structural & molecular biology* **18**, 894–901 (2011).
35. Biggs, R., Liu, P. Z., Stephens, A. D. & Marko, J. F. Effects of altering histone posttranslational modifications on mitotic chromosome structure and mechanics. *Molecular biology of the cell* **30**, 820–827 (2019).
36. Rubinstein, M. & Colby, R. H. *Polymer Physics*. (Oxford University Press, 2003).
37. Fuller, B. G. *et al.* Midzone activation of aurora B in anaphase produces an intracellular phosphorylation gradient. *Nature* **453**, 1132–1136 (2008).
38. Vassilev, L. T. *et al.* Selective small-molecule inhibitor reveals critical mitotic functions of human CDK1. *Proceedings of the National Academy of Sciences of the United States of America* **103**, 10660–10665 (2006).
39. Mershin, A., Kolomenski, A. A., Schuessler, H. A. & Nanopoulos, D. V. Tubulin dipole moment, dielectric constant and quantum behavior: computer simulations, experimental results and suggestions. *Biosystems* **77**, 73–85 (2004).
40. Wall, M. A., Socolich, M. & Ranganathan, R. The structural basis for red fluorescence in the tetrameric GFP homolog DsRed. *Nature Structural Biology* **7**, 1133–1138 (2000).

41. Gebala, M., Johnson, S. L., Narlikar, G. J. & Herschlag, D. Ion counting demonstrates a high electrostatic field generated by the nucleosome. *eLife* **8**, (2019).

42. McNaughton, B. R., Cronican, J. J., Thompson, D. B. & Liu, D. R. Mammalian cell penetration, siRNA transfection, and DNA transfection by supercharged proteins. *Proceedings of the National Academy of Sciences* **106**, 6111–6116 (2009).

43. Dogterom, M. & Yurke, B. Measurement of the Force-Velocity Relation for Growing Microtubules. *Science* **278**, 856–860 (1997).

44. Skoufias, D. A. *et al.* S-Trityl-L-cysteine Is a Reversible, Tight Binding Inhibitor of the Human Kinesin Eg5 That Specifically Blocks Mitotic Progression*,. *Journal of Biological Chemistry* **281**, 17559–17569 (2006).

45. Levesque, A. A. & Compton, D. A. The chromokinesin Kid is necessary for chromosome arm orientation and oscillation, but not congression, on mitotic spindles. *The Journal of cell biology* **154**, 1135–1146 (2001).

46. Brouhard, G. J. & Hunt, A. J. Microtubule movements on the arms of mitotic chromosomes: Polar ejection forces quantified in vitro. *PNAS* **102**, 13903–13908 (2005).

47. Wandke, C. *et al.* Human chromokinesins promote chromosome congression and spindle microtubule dynamics during mitosis. *The Journal of cell biology* **198**, 847–863 (2012).

48. Almeida, A. C. & Maiato, H. Chromokinesins. *Curr Biol* **28**, R1131–R1135 (2018).

49. Walther, N. *et al.* A quantitative map of human Condensins provides new insights into mitotic chromosome architecture. *The Journal of cell biology* **217**, 2309–2328 (2018).

50. Woodruff, J. B. *et al.* The Centrosome Is a Selective Condensate that Nucleates Microtubules by Concentrating Tubulin. *Cell* **169**, 1066-1077.e10 (2017).

Methods

Cell lines and cell culture

All cell lines used in this study have been regularly tested negative for mycoplasm contamination. All cell lines in this study were derived from a HeLa "Kyoto" cell line previously described in [51]. Cells were cultured in Dulbecco's modified eagle medium (DMEM) (IMP/IMBA/GMI Molecular Biology Service/Media Kitchen) containing 10% (v/v) fetal bovine serum (FBS; Gibco, 10270-106, 2078432), 1% (v/v) penicillin-streptomycin (Sigma-Aldrich), 1% (v/v) GlutaMAX (Gibco; 35050038) and selected antibiotics according to the respective expression constructs: blasticidin S (6 µg mL^{-1}, Thermo Fisher Scientific), puromycin (0.5 µg mL^{-1}, Calbiochem), hygromycin B (0.25 mg mL^{-1}) and G418 (1 mg mL−1, Invitrogen). HeLa cells were cultured at 37°C in a 5% CO_2-containing atmosphere. Chromatin was visualized by stable expression of histone 2B labelled with mCherry (H2B-mCherry; Figs. 2a-f, 4, Extended Data Figs. 4a, b, 6a−d) or with Aurora B-FRET sensor (CFP/YFP) (Fig. 2g-l, Extended Data Fig. 4) or alternatively by labelling with Hoechst 33342 (1.62 µM, Invitrogen) (Figs. 1a-c, 2m, 3a-d, Extended Data Figs. 1a, 3c, 5a,c). Tubulin was visualized by stable expression of an N-terminally tagged eGFP-α-Tubulin fusion (Extended Data Figs. a, c) or by labeling with SiR-Tubulin (100 nM) (Figs. 1a, 4a, Extended Data Fig. 3c)[25]. Centromeres were visualized by stable expression of an N-terminally tagged eGFP-CENP-A fusion (Fig. 4a). Live-cell imaging was performed in DMEM containing 10% (v/v) FBS (Gibco, 10270-106, 2078432), 1% (v/v) penicillin-streptomycin (Sigma-Aldrich), and 1% (v/v) GlutaMAX (Gibco; 35050038) but omitting phenol red and riboflavin to reduce autofluorescence (imaging medium, short "IM")[51]. Cells were grown in 10 cm or 15 cm CELLSTAR® (Greiner) dishes, in 75 cm^2 or 175 cm^2 Nunc™ EasYFlask™ cell culture flasks (Thermo Fisher Scientific) or in 96-well, 48-well, 12-well or 6-well Nunclon™ Delta Surface multi well plates (Thermo Fisher Scientific). For live-cell imaging, cells were cultivated on Nunc™ LabTek™ II chambered cover glass (Thermo Fisher Scientific), on µ-Slide 8 well covered coverslips (ibidi), in µ-Dish 35 mm, high, imaging dishes with polymer or glass bottom (ibidi).

Generation of stable fluorescent reporter and genetically engineered cell lines

Cell lines stably expressing fluorescently labelled marker proteins were generated by random plasmid integration (for transfection conditions, see below) or by a lentiviral vector system pseudotyped with a mouse ecotropic envelope that is rodent-restricted (RIEP receptor system). Construction of RIEP receptor parental cell lines and subsequent generation of stable cell lines that express fluorescent marker proteins was performed as described previously[52].

HeLa genome editing was performed using CRISPR-Cas9 mediated integration approach, using the chimeric Cas9-human Geminin fusion (Cas9-hGem) modification for enhanced editing efficiency[53]. Single-guide RNA (sgRNA) was cloned into pX330-U6-Chimeric_BB-CBh-hSpCas9-hGem-P2A-mCherry*aBpil (kind gift from Stefan Ameres). For tagging of endogenous Smc4 genes with an auxin-inducible degron tag, a repair template for targeting the C-terminus of the protein was designed, with homology flanks of 800 and 901 bp length for the 5' and 3' flanks, respectively. The repair template containing the coding sequence for a C-terminal mAID-HaloTag, including mutations of the protospacer adjacent motif (PAM), was synthesized as a gBlock® (IDT) and cloned into plasmid pCR2.1 for amplification. sgRNA/Cas9 and homology repair template plasmids were co-transfected using the Neon™ transfection system (Thermo Fisher Scientific). Transfection was performed according to the manufacturer's guidelines (for HeLa cells: Pulse voltage, 1.005 V, pulse width, 35 ms, pulse number, 2), using the 100 µl tip cuvette, with 10 µg homology repair template and 10 µg gRNA/Cas9-hGEM for $1x10^6$ cells. 9 days after electroporation, cell pools were stained with Oregon Green® HaloTag (Promega, G2801) ligand and single clones isolated using fluorescence-activated cell sorting (FACS) and sorted into 96-well plates. Genotyping was performed as in a previous study[52].

Integration of the OsTIR1(F74G) ligase into the adeno-associated virus integration site (AAVS1, designated "safe harbor") locus for establishment of AID2 auxin-inducible degradation of Smc4 was achieved using a sgRNA and homology repair template strategy described in [54]. Single-guide RNA was cloned into pX330-U6-Chimeric_BB-CBh-hSpCas9-hGem-P2A-mCherry*aBpil. For integration of the OsTIR1(F74G), a homology template containing an OsTIR1(F74G)-SnapTAG-MycA1-NLS and homology flanks of 804 and 837 bp length for the 5' and 3' flanks, respectively, was generated. Co-transfection of sgRNA/Cas9 and homology repair template plasmids was performed as described above. 8 days after electroporation, transfected cells were selected with 6µg/ml Blasticidin. Single clones were isolated from the stable pool by single cell dilution into 96-well plates. To identify clones which depleted SMC4-mAID-Halo, clones were treated for 90min with 1µM 5-Ph-IAA24, stained with Oregon Green® HaloTag (Promega, G2801) ligand and then analyzed by flow cytometry using an iQue Screener Plus.

Transfection of plasmids and small interfering RNA

For expression of fluorescently labelled markers, the respective genes were cloned into bicistronic vectors containing an IRES or a 2A "self-cleaving" peptide sequence with antibiotic resistance genes that allow the protein of interest and the resistance gene to be expressed from the same transcript. For transient transfection or transfection for subsequent selection and colony picking, plasmids were transfected using X-tremeGENE 9 DNA transfection reagent (Roche, 6365787001) following the manufacturer's protocol (1 µg plasmid, 4.5 µl X-tremeGENE 9 in 100 µl serum-free OptiMEM) or PEI transfection reagent (1 mg ml^{-1} stock, Polyscience 24765-2, 4 µg of transfection reagent per 1 µg of plasmid). For stable expression, plasmids were transfected using PEI, 10 µg plasmid for one ~70 confluent 15 cm dish and incubated for 48 h before antibiotic selection.

Small interfering RNAs (siRNAs) were delivered with lipofectamine RNAiMax (Invitrogen) according to the manufacturer's instructions. hKid (Kif22) was targeted using 16 nM custom silencer select siRNA (sense strand CAAGCUCACUCGCCUAUUGtt, Thermo Fisher Scientific, including a 3' overhang tt dinucleotide for increased efficiency). Kif4A was targeted using 16 nM custom silencer select siRNA (sense strand GCAAGAUCCUGAAAGAGAUtt, Thermo Fisher Scientific, including a 3' overhang tt dinucleotide for increased efficiency). Custom silencer select siXWNeg (sense strand UACGACCGGUCUAUCGUAGtt, Thermo Fisher Scientific, including a 3′ overhanging tt dinucleotide for increased efficiency) was used as a non-targeting siRNA control. Cells

were imaged 30 h after siRNA transfection. Co-transfection of hKid and Kif4a siRNAs was performed using 16 nM final concentration each. Both hKid and Kif4a siRNAs were described in [23].

Inhibitors and small molecules

To degrade Smc4-mAID-Halotag, cells were incubated in 1 µM 5-Phenylindole-3-acetic acid (5-PhIAA) (Bio Academia, 30-003) for 2.5-3h. To induce histone hyperacetylation, cells were incubated with 5 µM Trichostatin A (TSA) (Sigma-Aldrich, T8552). To arrest cells in prometaphase with monopolar spindle configuration, cells were incubated in 5 µM S−Trityl−L−cysteine (STLC) (Enzo Life Sciences, ALX-105-011-M500) for 2-3h. To arrest cells in prometaphase, cells were incubated for 2-3h in nocodazole (200 ng ml^{-1} for live-cell imaging only)or 100 ng ml^{-1} for microinjection and/or subsequent washout; Sigma-Aldrich, M1404). Nocodazole washout was by washing cells 5 times with prewarmed imaging medium on the microscope. To arrest cells in metaphase for microinjection, cells were incubated with 12 µM proTAME (R&D systems, I-440-01M) for 2 h. To synchronize cells to the G2-M boundary, cells were first synchronized with a double thymidine block followed by a single RO3306 block. One day after seeding, cells were transferred into medium containing 2 mM thymidine (Sigma-Aldrich, T1895). 16 h later, cells were washed three times with prewarmed medium and released for 8 h. The thymidine block was repeated once. 6 h after the second thymidine release cells were transferred into medium containing 8 µM RO3306 (Sigma-Aldrich, SML0569) for 4 h. Following G2 arrest, RO3306 was removed and cells were washed three times with imaging medium containing 1.5 µM okadaic acid (LC laboratories, O-5857).

Immunofluorescence

For all immunofluorescence experiments, cells were grown on sterilized 18 mm round Menzel cover glasses in 24-well multi-well plates, except immunofluorescence against acetylated histones, which was performed on Nunc™ LabTek™ II chambered cover glass. For co-staining spindle poles and centromeres, cells were fixed and extracted at the same time with 1XPHEM (60 mM K-PIPES (Sigma-Aldrich), pH 6.9, 25 mM K-HEPES (Sigma-Aldrich), pH 7.4, 10 mM EGTA (Merck, 324626), 4 mM $MgSO_4•7H_2O$ (Sigma-Aldrich)) containing 0.5% Tween-20 (Sigma-Aldrich) and 4% methanol-free formaldehyde (Thermo Fisher Scientific) for 10 min. The fixation reaction was quenched with 10 mM Tris-HCl (Sigma-Aldrich), pH 7.4, in phosphate-buffered saline (PBS), washed again with PBS and blocked in 10% normal goat serum (Abcam), 0.1%Tween-20 (Sigma-Aldrich) for 1 h.

For staining of acetylated histone tails or CyclinB1, cells were fixed in PBS containing 4% methanol-free formaldehyde (Thermo Fisher Scientific, 28906) for 10 min. The fixation was quenched with 10 mM Tris-HCl (Sigma-Aldrich) pH 7.4 in PBS for 5 min, and cells permeabilized with PBS containing 0.5% Triton-X100 for 15 min, washed again with PBS and blocked using 2% bovine serum albumin (BSA) (Sigma-Aldrich, A7030) in PBS, containing 0.2% Tween-20 (Sigma-Aldrich), for 1 h. Antibody dilution buffer was composed of PBS with 2% BSA (Sigma-Aldrich, A7030), containing 0.1% Tween-20 (Sigma-Aldrich). After primary and secondary antibody incubations, samples were washed with PBS containing 0.1% Tween-20 (Sigma-Aldrich), three times for 10 min each time. CENP-A was detected with a monoclonal mouse antibody (Enzo Life Sciences, ADI-KAM-CC006-E, 10161910, 1:1000) and visualized using a goat anti-mouse Alexa Fluor 488 secondary antibody (Molecular Probes, A11001, 1:1000) (Extended Data Fig. 1d). Pericentrin was detected with a recombinant rabbit antibody (Abcam, ab220784, GR3284309-1, 1:2000) and visualized using a goat anti-rabbit Alexa Fluor 633 secondary antibody (Molecular Probes, A21071, 1:1000) (Extended Data Fig. 1d). Acetylated histone2B was detected using a polyclonal rabbit antibody (Millipore, 07-373, 3092508, 1:500) and visualized using a donkey anti-rabbit Alexa Fluor 488 secondary antibody (Molecular Probes, A21206, 1:1000) (Extended Data Figs. 2a, c, 3a). Acetylated histone 3 was detected using a polyclonal rabbit antibody (Merck, 06-599, 3260200, 1:500) and visualized using a donkey anti-rabbit Alexa Fluor 488 secondary antibody (Molecular Probes, A21206, 1:1000) (Extended Data Fig. 2a, c). Acetylated Histone 4K16 was detected using a recombinant rabbit antibody (Abcam, ab177191, GR284778-8, 1:400) and visualized using a donkey anti-rabbit Alexa Fluor 488 secondary antibody (Molecular Probes, A21206, 1:1000) (Extended Data Figs. 2a, c). Cyclin B1 was detected with a monoclonal rabbit antibody (Cell Signaling, 12231S, 7, 1:800) and visualized using a donkey anti-rabbit Alexa Fluor 488 secondary antibody (Molecular Probes, A21206, 1:1000) (Extended Data Fig. 2e). Immunofluorescence samples prepared in Nunc™ LabTek™ II chambered cover glass wells were stored in PBS containing 1.62 µM Hoechst 33342 (Invitrogen). Immunofluorescence samples prepared on 18 mm round Menzel cover glasses were embedded in Vectashield with or without DAPI (Vectorlabs, H-1000 or H-1200).

Preparation of 384-well microscopy plates and coverslips for *in vitro* assays

384-well µCLEAR® microscopy plates (Greiner Bio-One, 781906) were washed with 5% HellmanexIII (Lactan, 105513203) in ≥18 MΩ MonoQ H_2O at 65°C in a table top Incu-Line oven (VWR) for 4 h and then rinsed 10 times with ≥ 18 MΩ MonoQ H_2O. Silica was etched with 1 M KOH (Sigma-Aldrich) for 1 h at room temperature rinsed again 10 times with ≥ 18 MΩ MonoQ H_2O. Etched multiwell plate was treated with 5k-mPEG-silane (Creative PEGworks, PLS-2011) suspended in 95% ethanol (VWR) for 18h at room temperature. Plate was washed once with 95% EtOH, then 10 times with ≥ 18 MΩ MonoQ H_2O and dried in a clean chemical hood overnight. Until individual wells were used, the plate was sealed with adhesive PCR plate foil (Thermo Fisher Scientific) and kept in a dry and dark space. Before an experiment, foil above individual wells was cut and 50 µl of 100 mg ml^{-1} BSA (Sigma-Aldrich, A7030).

For microtubule/nucleosome array droplet experiments (Fig. 3e), thin layer cover glass sandwiches were constructed from passivated 24x60 mm Menzel coverglass (VWR). To clean coverslips, they were vertically stacked into a Coplin jar (Canfortlab, LG084). Coplin jars were then sonicated in acetone (Sigma-Aldrich) for 15 min, in 100% EtOH (VWR) for 15 min and then washed 10 times with ≥ 18 MΩ MonoQ H_2O. All sonication steps were performed using an ultrasonic cleaning bath (Branson, 2800 Series Ultrasonic Cleaner, M2800). In a separate Erlenmeyer flask, 31.5 ml 30% aqueous hydrogen peroxide solution (Sigma-Aldrich, 31642) was added to 58.5 ml concentrated sulfuric acid (Sigma-Aldrich, 258105) (“piranha” acid). The flask was gently swirled until bubbling and heat occurred, then the whole contents of the flask was added to the coverslips in the Coplin jars, ensuring that all coverslip surfaces were covered. The jar

was transferred into a 95°C water bath and heated for 1 h. Afterwards, piranha solution was discarded, and cover glasses washed once with ≥18 MΩ MonoQ H_2O and etched with 0.1 M KOH for 5 min. Cover glasses were transferred to a fresh, dry Coplin jar and dried to completion in a 65°C bench top oven, and afterwards let to cool to room temperature. In a separate Erlenmeyer flask, 4 ml dichlorodimethylsilane (DCDMS) (Sigma-Aldrich, 440272, anhydrous) was injected into 80 ml heptane (Sigma, 246654, anhydrous). The contents of the flask were immediately transferred to the jar containing the cover glasses, and jar was incubated for 1 h at room temperature. Afterwards, silane was decanted, and cover glasses are sonicated in chloroform (Sigma-Aldrich) for 5 min, washed in chloroform once, sonicated in chloroform again for 5 min, and sonicated twice in ≥18 MΩ MonoQ H_2O. Finally, cover glasses were washed once more in chloroform, air dried, and stored in a sealed container in a dry and dark, dust-free space (up to 6 months).

To passivate cover glasses, on the day of an experiment a cover glass was transferred to a drop of 5% Pluronic F-127 (Thermo Fisher Scientific, P6866) dissolved in BRB80 buffer (80 mM K-PIPES, pH 6.9 (Sigma-Aldrich, P6757), 1 mM $MgCl_2$ (Sigma-Aldrich), 1 mM EGTA (Merck, 324626)) for >2 h at room temperature. Directly prior to assembly of the imaging chamber, cover glass was rinsed once with ≥18 MΩ MonoQ H_2O and once with BRB80 (80 mM K-PIPES, pH 6.9 (Sigma-Aldrich, P6757), 1 mM $MgCl_2$ (Sigma-Aldrich), 1 mM EGTA (Merck, 324626)).

Expression and purification of GFP proteins

pET-based constructs for the expression and purification of mEGFP(-7e) and scGFP(+7e) were a generous gift from Dr. David Liu[55]. An overnight culture of Rosetta 2 (pLysS) *E. coli* (Novagen) transformed with pET_-7GFP, or pET_+7GFP plasmids encoding GFP with a theoretical peptide charge of -7e or +7e, respectively, were grown on an agar plate by re-plating a single transformant on LB supplemented with 100 ng/µl of ampicillin at 37°C. The bacterial lawn was suspended in LB supplemented with the 100 ng/µl of ampicillin and grown at 37˚C to a density ($OD_{600\ nm}$) of 0.4, cooled over 1 h to 18˚C, and recombinant protein expression was induced by addition of IPTG to 0.5 mM for 18 h at 18°C. The cells were collected by centrifugation, resuspended in NiNTA Lysis Buffer (50 mM HEPES•NaOH, pH 7, 150 mM NaCl, 10% [w/v] glycerol, 15 mM Imidazole, 5 mM ß-mercaptoethanol, 1 mM Benzamidine, 100 µM Leupeptin, 100 µM Antipain, 1 µM Pepstatin), the cellular suspension was flash frozen in liquid N_2, and stored at -80°C.

Bacterial cultures with expressed GFP proteins in NiNTA Lysis Buffer were thawed in a water bath and lysed by multiple passages through an Avestin Emulsiflex-C5 high pressure homogenizer at ~10,000 PSI. An equal volume of NiNTA Dilution Buffer (50 mM HEPES•NaOH, pH 7, 1.85 M NaCl, 10% [w/v] glycerol, 15 mM Imidazole, 5 mM ß-mercaptoethanol, 1 mM Benzamidine, 100 µM Leupeptin, 100 µM Antipain, 1 µM Pepstatin) was added to the lysate to increase NaCl concentration to 1 M. Soluble bacterial lysate was isolated by centrifugation of cellular debris in a Beckman Avanti J-26 XPI centrifuge in a JA25.5 rotor at 20,000 RPM. Soluble lysate was incubated with NiNTA resin (Qiagen) equilibrated in NiNTA Wash Buffer A (50 mM HEPES•NaOH, pH 7, 1 M NaCl, 10% [w/v] glycerol, 15 mM Imidazole, 5 mM ß-mercaptoethanol, 1 mM Benzamidine, 100 µM Leupeptin, 100 µM Antipain, 1 µM Pepstatin) for 2 h in batch with end-over-end mixing. NiNTA resin was poured into a BioRad EconoColumn and resin was washed 20 column volumes of NiNTA Wash Buffer A and 20 column volumes of NiNTA Wash Buffer B (50 mM HEPES•NaOH, pH 7, 150 mM NaCl, 10% [w/v] glycerol, 15 mM Imidazole, 5 mM ß-mercaptoethanol, 1 mM Benzamidine, 100 µM Leupeptin, 100 µM Antipain, 1 µM Pepstatin) before elution in NiNTA Elution Buffer (50 mM HEPES•NaOH, pH 7, 150 mM NaCl, 10% [w/v] glycerol, 350 mM Imidazole, 5 mM ß-mercaptoethanol, 1 mM Benzamidine, 100 µM Leupeptin, 100 µM Antipain, 1 µM Pepstatin).

GFP proteins were diluted with 9 volumes of Buffer SA (20 mM HEPES•NaOH, pH 7, 10% [w/v] glycerol, 1 mM DTT) and applied to Source 15S (meGFP) or Source15Q (scGFP) resin (GE Healthcare) equilibrated in 98.5% Buffer SA and 1.5 % Buffer SB (20 mM HEPES•NaOH, pH 7, 1 M NaCl, 10% [w/v] glycerol, 1 mM DTT) and eluted with a linear gradient to 100% Buffer SB. Fractions containing GFP proteins were concentrated in a centrifugal concentrator with a 3,000 dalton MWCO and purified further by size exclusion chromatography using a Superdex 200 10/300 GL gel filtration column equilibrated with Gel Filtration Buffer (20 mM Tris•HCl, pH 8, 150 mM NaCl, 10% [w/v] glycerol, 1 mM DTT). Peak fractions of purified mEGFP(-7e) and scGFP(+7e) protein were concentrated in a centrifugal concentrator, as above, and quantified by measuring protein absorbance at 280 nm using their calculated molar extinction coefficient (https://web.expasy.org/protparam/) of 23,380/M•cm for meGFP and 18,910/M•cm for scGFP. Purified proteins were flash frozen in liquid N_2 and stored at -80˚C in single use aliquots.

Nucleosome array *in vitro* experiments

Generation, fluorophore labelling, assembly and quality control of nucleosome arrays has been described in [13]. In this study, 12X601 nucleosome arrays carrying no label, an Alexa Fluor 488, or Alexa Fluor 594 label were used. The covalently fluorescently labelled nucleosome arrays used for microinjection were labeled at an 8% fluorophore density (8 in 100 histone2B proteins labeled with a fluorophore) and dialyzed against TE (10 mM Tris-HCl (Sigma-Aldrich), pH 7.4 (Sigma-Aldrich), 1 mM EDTA (Sigma-Aldrich), pH 8.0, 1mM DTT (Roche, 10708984001)) to remove glycerol.

To induce phase separation of nucleosome arrays (Extended Data Figs. 4e, 5e,g), arrays were first equilibrated in chromatin dilution buffer (25 mM Tris•OAc, pH 7.5 (Sigma-Aldrich), 5 mM DTT (Roche, 10708984001), 0.1 mM EDTA (Sigma-Aldrich), 0.1 mg ml^{-1} BSA (Sigma-Aldrich, A7030), 5% (w/v) glycerol (Applichem, A0970)) in the presence of 2.03 µM Hoechst 33342 (Invitrogen, H1399) when using unlabeled arrays for 10 min at room temperature. Phase separation was induced by addition of 1 volume phase separation buffer (25 mM Tris•OAc, pH 7.5 (Sigma-Aldrich), 5 mM DTT (Roche, 10708984001), 0.1 mM EDTA (Sigma-Aldrich), 0.1 mg ml-1 BSA (Sigma-Aldrich, A7030), 5% (w/v) glycerol (Applichem, A0970), 300 mM KOAc (Sigma-Aldrich), 1 mM Mg[OAc]2, 2 µg ml^{-1} glucose oxidase (Sigma-Aldrich, G2133), 350 ng ml^{-1} catalase (Sigma-Aldrich, C1345) and 4 mM glucose (AMRESCO, 0188)). For in vitro assays containing tubulin, EGTA was substituted for EDTA in the dilution and phase separation buffers. After addition of phase separation buffer, the final concentration of nucleosome arrays per reaction was 500 nM, and reactions were incubated at room temperature for 10 min before transferring the suspension to imaging chambers.

To visualize soluble tubulin partitioning relative to chromatin droplets *in vitro*, 20 µl of chromatin droplet suspension were transferred to a passivated well of a 384-well microscopy plate. Chromatin droplets were to sedimented for 15 min. Afterwards, 5 µl of soluble TRITC-labelled tubulin (Cytoskeleton, TL590M) in phase separation buffer containing 500 ng ml^{-1} nocodazole was added for a final tubulin concentration of 5 µM. Soluble tubulin equilibrated for 10 min before images were recorded.

To visualize GFP surface charge variant partitioning relative to chromatin droplets *in vitro*, 20 µl of chromatin droplet suspension were transferred to a passivated well of a 384-well microscopy plate. Chromatin droplets were allowed to sediment for 15 min, after which 5 µl of GFP solution in phase separation was added to a final concentration of 5 µM. GFP proteins equilibrated for 10 min before images were recorded.

To visualize chemically modified dextran partitioning into chromatin droplets *in vitro*, 20 µl of chromatin droplet suspension were transferred to a passivated well of a 384-well microscopy plate. Chromatin droplets were allowed to sediment for 15 min, after which 5 µl dextran solution in phase separation buffer was added to a final concentration of 500 µg ml^{-1}. The dextran used was a fluorescein (FITC) labelled 4.4 kDa dextran fraction (negative overall charge conferred to dextran by fluorophore charge) (Sigma-Alrich, FD4) or a FITC labelled 4.4 kDa dextran fraction modified with diethylaminoethyl (DEAE) groups conferring overall positive charge (TdB, DD4).

All images of macromolecule partitioning relative to chromatin droplets *in vitro* (Fig. 3e, Extended data Fig. 5e, g) were recorded on the incubated stage of a customized Zeiss LSM980 microscope using a x40 1.4 NA Oil DIC Plan-Apochromat objectives (Zeiss).

Nucleosome array acetylation *in vitro*

To generate acetylated nucleosome arrays for microinjection, recombinant p300 histone acetyl transferase domain was generated (VBCF Protein technologies Facility) using plasmid $pETduet+p300_{HAT}$ according to a purification strategy described in [13]. To induce histone acetylation of nucleosome arrays, arrays with 8% Alexa Fluor 488 or Alexa Fluor 594 label density at a concentration of 3.85 µM were incubated with 6.12 µM p300-HAT (enzyme stock 61.2 µM in gel filtration buffer (20 mM Tris•HCl, pH 8.0, 150 mM NaCl, 10% (w/v) glycerol, 1mM DTT)) in the presence of 750 µM Acetyl-CoA (Sigma-Aldrich, A2056) in gel filtration buffer at room temperature for 2 h with occasional agitation. Afterwards, the acetylation was stopped by addition of A-485 (Tocris, 6387) to a final concentration of 9 µM and the reaction mixture stored in the dark. To 10 µl of quenched acetylation reaction, 10 µl dilution buffer containing 5 µM A-485 (Tocris, 6387) were added and reaction allowed to equilibrate at room temperature for 10 min. Afterwards, 1 volume of phase separation buffer containing 5 µM A-485 (Tocris, 6387) was added and the mixture incubated for 10 min at room temperature before transferring the suspension to a passivated 384-well microscopy plate well.

Microtubule *in vitro* polymerization

To generate stabilized microtubule seeds for nucleation of microtubule networks *in vitro*, 22 µl of 5 mg ml^{-1} tubulin protein (Cytoskeleton, T240) was mixed with 2 µl of 5 mg ml^{-1} TRITC-labeled tubulin protein (Cytoskeleton, TL590M) and 1 µl of 5 mg ml^{-1} Biotin-XX-labeled tubulin (Pursolutions, 033305). All tubulin storage solutions were prepared in BRB80 (80 mM K-PIPES, pH 6.9 (Sigma-Aldrich, P6757), 1 mM $MgCl_2$ (Sigma-Aldrich), 1 mM EGTA (Merck, 324626)). The tubulin mixture was centrifuged at 4°C for 15 min in a tabletop centrifuge (Eppendorf, 5424R) at 21k x g. To 22.5 µl of the resulting supernatant, 2.5 µl 10 mM guanylyl-(alpha, beta)-methylene-diphosphonate (GMPCPP) (Jena Biosciences, NU-405) were added to a final concentration of 1 mM and the resulting solution incubated at 37°C in a water bath in the dark for 30 min. The resulting seeds were sheared using a 22-gauge needle Hamilton syringe (Sigma-Aldrich, 20788). The resulting suspension was stored in the dark. Seeds were prepared freshly per day and used for subsequent experiments.

Soluble tubulin polymerization mix containing 50 µM tubulin protein (Cytoskeleton, T240), 1 µM TRITC-labeled tubulin protein (Cytoskeleton, TL590M) and 1 mM GTP (Sigma-Aldrich, G8877) in BRB80 (80 mM K-PIPES, pH 6.9 (Sigma-Aldrich, P6757), 1 mM $MgCl_2$ (Sigma-Aldrich), 1 mM EGTA (Merck, 324626)) was centrifuged at 4°C for 15 min in a tabletop centrifuge (Eppendorf, 5424R) at 21k x g. The resulting supernatant was used to assemble a microtubule polymerization mix containing 20 µM total soluble tubulin (19.61 µM unlabeled tubulin dimers, 0.39 µM labelled tubulin), 50 mM DTT (Roche, 10708984001), 120 µM glucose (AMRESCO, 0188), 1 mM GTP (Sigma-Aldrich, G8877), 20 µg ml^{-1} glucose oxidase (Sigma-Aldrich, G2133), 175 ng ml^{-1} (Sigma-Aldrich, C1345) in BRB80 (80 mM K-PIPES, pH 6.9 (Sigma-Aldrich, P6757), 1 mM $MgCl_2$ (Sigma-Aldrich), 1 mM EGTA (Merck, 324626)). Composition of soluble tubulin and tubulin polymerization mix was adapted from a procedure for visualization of microtubule plus-end tracking (+TIP) proteins[56].

To visualize chromatin droplets along with polymerized microtubules, imaging chambers were constructed as described in [57]. Prior to Pluronic F-127 passivation, each silanized 24x60 mm cover glass was cut into a 24x25 mm (top piece) and 24x35 mm (bottom piece) using a diamond tipped steel scribe (Miller, DS-60-C). The bottom coverslip was mounted into the support slide and fixed in place with preheated VALAP (1 part Vaseline (Sigma-Aldrich, 16415), 1 part lanolin (Sigma-Aldrich, L7387), 1 part Paraffin wax (Sigma-Aldrich, 327204); all parts by weight). In the central region of the bottom cover glass, a 2 Well Silicon Culture-Insert (ibidi, 80209) was attached and 40 µl of nucleosome array droplet suspension added to one of the wells. The suspension was sedimented for 15 min in a humidified chamber at room temperature. Afterwards, 32 µl of buffer were removed from the well, the Culture-Insert removed from the coverslip and 20 µl soluble tubulin mix added to the remaining chromatin droplet suspension. The top coverslip was added on top with the passivated side facing the reaction mixture, and the droplet was allowed to spread fully (~10 s). Afterwards, the sample was sealed with VALAP to prevent evaporation and thermal streams within the liquid film. This procedure yielded a liquid film of ~30 µm thickness. The assembled imaging cell was transferred to the incubated stage of a customized Zeiss LSM980 microscope combined with the Airyscan2 detector, using a x63 1.4 NA Oil DIC Plan-Apochromat objective (Zeiss). The sample was incubated at 37°C for >30 min before images were recorded.

CLEM and electron tomography

HeLa cells stably expressing H2B-mCherry were cultured on carbon-coated Sapphire discs (0.05 mm thick, 3 mm diameter; Wohlwend GmbH). To enrich prometaphase cells, cells were synchronized to G2-M using a double thymidine (Sigma-Aldrich) block for 16 h with 2 mM thymidine each and a subsequent RO3306 (Sigma-Aldrich) block for 6 h with 8 µM RO3306. During the RO-3306 block, cells were treated with 5 µM TSA for 3 h prior to RO3306 washout. RO3306 was washed out by rinsing the cells 3 times with prewarmed imaging medium. Cells were observed on a customized Zeiss LSM780 microscope, using a x20 0.5 NA EC PlnN DICII Air objective (Zeiss). 25 min after the RO3306 washout, most cells reached prometaphase (based on DIC and chromatin morphology), and cells were subsequently processed for electron microscopy. Immediately before freezing, cells were immersed in cryoprotectant solution (imaging medium containing 20% Ficoll PM400; Sigma Aldrich), and instantly frozen using a high-pressure freezing machine (HPF Compact 01; Wohlwend GmbH).

Frozen cells were freeze-substituted into Lowicryl HM20 resin (Polysciences Inc., 15924-1) using freeze-substitution device (Leica EM AFS2, Leica Microsystems) as follows: Cells were incubated with 0.1% uranyl acetate (UA) (Serva Electrophoresis GmbH, 77870) in acetone at −90 °C for 24 h. The temperature was increased to −45 °C at a rate of 5 °C/h and then incubate for 5 h at −45 °C. Cells were washed three times in acetone at −45°C and then incubated in increasing concentrations of resin Lowicryl, HM20 in acetone (10, 25, 50, and 75% for 2 h each) while the temperature is further increased to −25°C at a rate of 2.5°C/h. Cells were then incubated in 100% resin Lowicryl, HM20 at −25°C for a total of 16 h, changing the pure resin solution after 12 h, 14 h, and 16 h. The resin was polymerized under UV light at −25 °C for 48 h. The temperature was increased to 20°C (5°C/h) and UV polymerization was continued for another 48 h.

After resin polymerization, sections of 250 nm thickness were cut with an ultramicrotome (Ultracut UCT; Leica) and collected on copper–palladium slot grids (Science Services) coated with 1% Formvar (Plano GmbH). The sections were post-stained with 2% UA in 70% methanol at room temperature for 7 min and lead citrate at room temperature for 5 min. The sections were observed by Tecnai F20 transmission EM (200 kV; FEI). H2B fluorescence was used to choose cells and subcellular ROIs for tomography. For tomography, a series of tilt images were acquired over a −60° to +60° tilt range with an angular increment of 1° using Serial EM software[58] at a final x-y pixel size of 1.14 nm. Tomograms were reconstructed using R-weighted back projection method implemented in the IMOD software package[59].

Western blotting

Samples were separated by Novex NuPAGE SDS-PAGE system (Thermo Fisher Scientific) using 4% - 12% BisTris in MES running buffer according to manufacturer's guidelines, and transferred to a 0.45 µm nitrocellulose membrane (Bio-Rad) by tank-blot wet transfer (Bio-Rad) at room temperature for 1 h. Blocking, primary antibody incubations (4°C, 16 h) and secondary antibody incubations (room temperature, 1.5 h) were performed in 5% (w/v) milk (Maresi, "fixmilch" Instant milk powder) in PBS, containing 0.05% Tween-20 (Sigma-Aldrich). Smc4 was probed using a rabbit polyclonal antibody (Abcam, ab229213, GR3228108-5, 1:1000). GAPDH was probed with a rabbit polyclonal antibody (Abcam, ab9485, GR3212164-2, 1:2500). hKid was probed with a monoclonal rabbit antibody (Abcam, ab75783, GR129278-4). Kif4a was probed with a recombinant rabbit antibody (Abcam, ab124903, GR96215-7, 1:1000). Horseradish peroxidase (HRP)-conjugated anti-mouse or anti-rabbit secondary antibodies (Bio-Rad, 1:10000) were visualized using ECL Plus Western Blotting Substrate (Thermo Fisher Scientific) on a Bio-Rad ChemiDoc Imager.

Microscopy

Images of G2-to-mitosis inductions, DsRed transfections, HaloTag stainings of wildtype and Smc4-mAID-HaloTag cells, histone acetylation, p300 overexpression, and fluorescence recovery after photobleaching (FRAP) experiments were recorded on a customized Zeiss LSM780 microscope, using x40 or x63 1.4 NA Oil DIC Plan-Apochromat objectives (Zeiss), operated by ZEN Black 2011 software. Images of chromatin density, live-microtubule stains, AluI-digestion time-lapse videos, nucleosome array microinjections, tubulin microinjections, CENP-A/Pericentrin immunofluorescence experiments and Cyclin B1 staining were recorded on a customized Zeiss LSM980 microscope combined with the Airyscan2 detector, using x40 or x63 1.4 NA Oil DIC Plan-Apochromat objectives (Zeiss), operated by ZEN3.3 Blue 2020 software. For all confocal microscopes, an incubator chamber (EMBL) provided a humidified atmosphere and a constant 37 °C temperature with 5% CO2.

For FRAP experiments, selected image regions were bleached using a laser intensity 200-fold higher than the laser intensity used for image acquisition, and each bleached pixel was illuminated 20 times with the pixel dwell time used for acquisition (1.79 µs). Images were acquired every 25 ms for the course of the experiment.

Images of nucleosome array droplets and *in vitro* polymerized microtubules were recorded on a customized Zeiss LSM980 microscope combined with the Airyscan2 detector, using x40 or x63 1.4 NA Oil DIC Plan-Apochromat objectives (Zeiss), operated by ZEN3.3 Blue 2020 software. For mounting 384-well microscopy plates, a Pecon® Universal Mounting Frame KM adapter was used. For mounting microtubule imaging slides, a custom aluminum mounting block for 24 mm X 24-60 mm coverslips was used (IMP/IMBA workshop and BioOptics).

Microinjection experiments

Live-cell microinjection experiments were performed using a FemtoJet® 4i microinjector in conjunction with an InjectMan® 4 micromanipulation device (Eppendorf). All microinjections were performed using pre-pulled Femtotips® injection capillaries (Eppendorf). The microinjection device was directly mounted on a customized confocal Zeiss LSM780 (Figs. 2c, g,i,l, Extended Data Fig. 4c) or a customized Zeiss LSM980 microscope (Figs. 2a, e, m, 3a, 4a, Extended Data Figs. 4a, 5a, c, 6a, c) with live-cell incubation (37°C, 5% CO_2). For all microinjections, cells were cultured in µ-Dish 35 mm high wall imaging dishes with polymer or glass bottom (ibidi) to reach near-confluency on the day of the injection.

For injection of AluI (Fast Digest, Thermo Fisher Scientific, FD0014), 1 volume of AluI-stock was added to 2 volumes of 5 mg ml^{-1} fluorescein (FITC) labelled 500 kDa dextran fraction (Sigma-Aldrich, FD500S) dissolved in injection buffer (50 mM K-HEPES, pH 7.4 (Sigma-Aldrich, H3375), 5% glycerol (Applichem, A0970), 1 mM $Mg(OAc)_2$ (Sigma-Aldrich, M5661)). Microinjection of mitotic cells (Figs. 2a, c, e, 4a, Extended Data Figs. 4a, 6a, c) was performed using injection settings of 130-150 hPa injection pressure, 0.15 to 0.25 s injection time and 30 hPa

compensation pressure. Microinjection of G2 interphase cells (Figs. g, I, k, Extended Data Fig. 4c) was performed using injection settings of 120 hPa injection pressure, 0.4 to 0.5 s injection time and 20 hPa compensation pressure.

For injection of nucleosome arrays (Fig. 2m), 1 volume of injection buffer (50 mM K-HEPES, pH 7.4, 25% glycerol buffer) was added to 1 volume unmodified and 1 volume acetylated nucleosome array solution (1.3 µM final concentration for each nucleosome in the injection buffer). Microinjection of mitotic cells was performed using injection settings of 180−190 hPa injection pressure, 0.35 s injection time, 85 hPa compensation pressure).

For injection of tubulin protein, TRITC-labelled tubulin (Cytoskeleton, TL590M) was dissolved in 5%-GPEM (80 mM K-PIPES, pH 6.9 (Sigma-Aldrich, P6757), 1 mM $MgCl_2$ (Sigma-Aldrich, 63065), 1 mM EGTA (Merck, 324626)) supplemented with 1 mM GTP (Sigma-Aldrich, G8877) to a concentration of 0.5 mg/ml. Protein was clarified by centrifugation at 4°C for 15 min in a tabletop centrifuge at 21,000 x g. Supernatant was microinjected into mitotic cells using injection settings of 175 hPa injection pressure, 0.25 s, 85 hPa compensation pressure. For microinjection of cells arrested in prometaphase with nocodazole, the G-PEM was additionally supplemented with 100 ng ml^{-1} nocodazole (Sigma-Aldrich, M1404).

For microinjection of GFP surface charge variants (Extended Data Fig. 5a), recombinant mEGFP(-7e) or scGFP(+7e) were dissolved in injection buffer (50 mM K-HEPES, pH 7.4 (Sigma-Aldrich, H3375), 25% glycerol (Applichem, A0970)) to a concentration of 15 µM. Microinjection of mitotic cells was performed using injection settings of 125 hPa injection pressure, 0.2 s injection time, 40 hPa compensation pressure.

For microinjection of charge modified dextran fractions (Extended Data Fig. 5c), a fluorescein (FITC) labelled 4.4 kDa dextran fraction (negative overall charge conferred to dextran by fluorophore charge) (Sigma-Alrich, FD4) or a FITC labelled 4.4 kDa dextran fraction modified with diethylaminoethyl (DEAE) groups conferring overall positive charge (TdB, DD4) were dissolved in injection buffer (50 mM K-HEPES, pH 7.4 (Sigma-Aldrich, H3375), 25% glycerol (Applichem, A0970)) to a concentration of 5 mg ml^{-1}. Microinjection of mitotic cells was performed using injection settings of 125 hPa injection pressure, 0.1-15 s injection time, 20 hPa compensation pressure.

Image analysis

DNA congression analysis

To quantify DNA congression to the spindle equator in live cells, the DNA distribution along a line profile (Fig. 1b, 7.06 µm width, 22.5 µm length, Extended Data Fig. 3 c, d, 12.04 µm width, 22.5 µm length) parallel to the pole-to-pole axis was measured. Along each line profile (22.5 µm length in total), the accumulated DNA density in the central 5 µm interval around the 50% distance between the poles (determined by pericentrin stain (Fig. 1a,b) or highest SiR-tubulin staining intensity (Extended Data Fig. 3c,d)) was divided by the total DNA density along the entire profile, after subtraction of the extracellular background fluorescence, with every line profile consisting of an average intensity projection of Z-slices around the pole-to-pole axis (Fig. 1a,b, 2.4 µm range, Extended Data Fig. 3 c, d, 0.75 µm range).

Chromatin/DNA compaction analysis

To quantify DNA density, in a central z-section of a mitotic cell (determined by visual inspection based on highest SiR-tubulin staining intensity at the poles (Fig. 1a, c, Extended Data Fig. 3c, e)) the DNA channel was denoised using a Gaussian blur filter (σ=2) and thresholded using the Otsu dark method in Fiji. The resulting binary mask was converted into a selection and the DNA density within this region of interest (ROI) measured. All data points were normalized to the mean of unperturbed control cells.

In STLC-treated cells used for AluI microinjection experiment (Fig. 2a, e, Extended Data Fig. 4c) , the DNA density was measured in line profiles. In a single Z-slice, a line profile (3 pixels wide, 2 µm long) through a chromosome parallel to the imaging plane (before AluI-injection) or a chromatin droplet (20 min after AluI-injection) was measured. The mean histone 2B fluorescence intensity in a 200 nm interval around the peak value was measured. Values were normalized to the mean of the non-injected control (Fig. 2b, f) or the non-injected condensin degraded control (Extended Data Fig. 4d).

In cells subjected to G2-mitosis induction experiments (Fig. 2g, i, k, Extended Data Fig. 4c), the YFP channel was denoised using a Gaussian blur filter (σ=2) and thresholded using the Otsu dark method in Fiji. The resulting mask was converted into a ROI and the histone 2B-YFP mean fluorescence recorded within this ROI. Per experiment, the values were normalized to the mean of the G2 measurements.

Electron tomography analysis

Analysis of electron tomograms were performed in IMOD/3dmod, Version 4.11. Annotation of all structures was performed in the 'Slicer Window' view, using running Z average intensity projections to increase contrast (microtubule annotation: projection of 10-20 Z-slices, chromatin annotation: 35-50 Z-slices). To account for loss in image sharpness towards the top and bottom of the recorded tomograms, for all tomograms, only the center section of the recorded volume was analyzed (tomograms with 120 to 150 slices, no annotation in the top and bottom 20 slices). For microtubule annotation, a zoom factor of 0.8 to 1.0 was used. For chromatin annotation, a zoom factor of 0.35-0.45 was used. Assignment of microtubules was based on ultrastructural morphology, and assignment of chromatin boundaries was performed based on local grain size, considering the transition of a large-grained, coarsely interspersed particle containing area (cytosol with ribosomes; typical CV>0.4) to a fine-grained, finely interspersed particle containing area (chromatin with nucleosomes; typical CV<0.3 for control, CV<0.4 for TSA) as the chromosome surface. The electron density as a determining factor of a chromatin surface was only used as a secondary direction since TSA treatment perturbs the chromatin density/morphology and thus decreases annotation accuracy. In average, an annotation landmark was set every 5-10 nm for both microtubules and the chromatin surface. After manual annotation of microtubules and a chromatin surface, a model of a meshed chromatin surface was generated, by averaging 5 consecutive annotated slices to increase surface smoothness. Microtubule segment length was measured within cytoplasm and chromatin-internal regions and normalized to the total volume of the respective domain.

Mitotic duration measurements in absence or presence of TSA

Fields of asynchronous cells stably expressing histone 2B-mRFP were imaged for up to 4 h. Timing of nuclear envelope breakdown (NEBD) and anaphase onset was determined by visual inspection of chromatin morphology.

FRAP analysis of chromatin mobility

To measure FRAP, raw data measurement, background subtraction, data correction and normalization was performed according to [60]. The measurement of FRAP ROI and background fluorescence signal was performed directly in ZEN software. Total chromatin fluorescence per time-lapse movie was measured using the 'Time Series Analyzer v3' (Author: Balaji J balaji2007@ucla.edu, Dept. of Neurobiology, UCLA).

FRET-analysis of AurB-FRET biosensor

To determine the mitotic state of control and AluI-injected cells at the G2 to M transition (Fig. 2g,I,k, Extended data Fig. 4c), CFP, FRET and YFP signals of the histone 2B fused Aurora B-FRET biosensor[37] were recorded at the same time. To quantify FRET efficiency, a custom Fiji script was used. In average intensity projections of 9 z-slices (1 μm each), a nuclear mask was generated using the YFP fluorescence, after denoising using a Gaussian blur filter (σ=5), by thresholding using the Otsu dark method. For each time point, the background for FRET and CFP channel was measure in an extracellular ROI (square of ~1 by 1 μm). After background subtraction, FRET and CFP signals within the nuclear ROI were denoised using a Gaussian blur filter (σ=5) and a FRET/CFP ratio calculated. The resulting ratiometric image was depicted using the "Fire" lookup-table in Fiji, in an interval of 0 to 1.4 for FRET/CFP.

Macromolecule partitioning relative to chromatin

In images of microinjected nucleosome arrays into metaphase cells (Fig. 2m), the DNA channel was denoised using a Gaussian blur filter (σ=2) and thresholded using the Otsu dark method in Fiji. The chromatin mask was converted into a ROI by using the 'Analyze Particles' function in Fiji. For the two injected nucleosome arrays of different colors, the mean fluorescence intensity was measured in the DNA ROI and divided by the fluorescence intensity in the cytosol measured in a circular ROI of ~5 µm diameter, with at least 1 µm distance to the chromosomes.

TRITC-tubulin partition coefficient (Fig. 3a, b) was measured >10 min after microinjection in nocodazole arrested cells. At the surface of a chromosome at the edge of the chromosome cluster, mean fluorescence intensity of TRITC was measured along a line profile (5 pixels width, 1.3 µm length) orthogonal to the chromosome surface. Values 1 µm apart within and outside of chromatin were divided, resulting in the measured equilibrium partition coefficient.

Distribution of different expressed DsRed fusions (Fig. 3c, d) was measured using a custom Fiji script. A chromatin mask was generated using thresholding (Default method, Fiji), after Gaussian blur filtering (σ=2) the chromatin channel. The mask was then shrunk by 0.2 µm and mean fluorescence measured within the mask. Cytoplasmic fluorescence was measured within a 0.5 µm wide ring, generated by extending the mask by 1.5 µm. Background mean fluorescence was measured within a small circular region outside of the cell and subtracted from chromatin and cytoplasmic values. Partitioning coefficients were obtained by dividing chromatin by cytoplasmic fluorescence values. Measurements were performed on the central Z-slice.

Distribution of microinjected differently charged GFPs (Extended Data Fig. 5a, b) and differently modified FITC-labelled dextran fractions (Extended Data Fig. c,d) was measured analogously, along line profiles orthogonal to the metaphase plate at the orthogonal surface of the chromatin mass (5 pixels width, 2.5 µm length). Values 1 µm apart within and outside of chromatin were divided, resulting in the measured equilibrium partition coefficient.

The distribution of soluble TRITC-tubulin dimers (Fig. 3e, f), differently charged GFPs (Extended Data Fig. 5e.f) and differently modified FITC-labelled dextran fractions (Extended Data Fig. g,h) within nucleosome array droplets *in vitro* was measured by determining the mean fluorescence intensity in the droplet in a central section of the droplet, in a small circular region covering ~25% of the droplet area in the respective section. In a large, rectangular buffer ROI without droplets, the mean fluorescence in the buffer was measured and the partition coefficient calculated for each field of droplets.

Chromatin droplet distribution analysis in cells

Chromatin distribution in pole-peripheral regions was measured at 36 min after nocodazole washout. The spindle pole position was determined as the z-slice with highest tubulin signal (SiR-tubulin (Fig. 4a) or eGFP-α-tubulin (Extended Data Fig. 4a, c)) and the total histone 2B (Fig. 4a, Extended Data Fig. 6a, c) and eGFP-CENPA fluorescence intensity in circular regions of interest (ROIs) (r=5 µm) in maximum intensity projections of 5 z-slices (1 µm offset between slices) around the central section was subtracted from the total cellular fluorescence in maximum intensity projections (cell outline determined by DIC-channel). Each dataset was normalized to the mean of the total fluorescence intensities of all cells.

Microtubule density distribution *in vitro*

After deconvolution in ZEN, Airyscan images of fields of microtubules were denoised using a Gaussian blur filter (σ=2). The background was then removed using the 'subtract background' function in Fiji, using a rolling ball radius of 740 pixels. The image was converted into 8-bit, and thresholded using the 'Auto Local Threshold' (v1.10.1) plugin in Fiji, with the Phansalkar method and a radius of 100. The resulting binary image was skeletonized using the 'Skeletonize' function in Fiji. The resulting skeleton length was measured. The chromatin channel was denoised using a Gaussian blur filter (σ=2) and thresholded using the Otsu method in Fiji. The resulting binary image was transformed into a ROI using the 'Analyze particles' function (size range: 5-infinity). Microtubule skeleton lengths were measured within chromatin ROIs and surrounding buffer and the ratio of total segment length in chromatin/buffer calculated per image.

Validation of auxin-inducible degradation of Smc4-mAID-HaloTAG in live cells

In images of fields of live cells stained with OregonGreen488 HaloTAG ligand, the total fluorescence intensity in average intensity projection was recorded in Fiji. To normalize the values to the cell count, ratios of HaloTAG fluorescence over SiR-DNA intensity were calculated, and the values normalized to the mean of the Hela WT cells.

Acetylated histone fluorescence intensity measurements

After indirect immunofluorescence of the respective histone-acetyl marks, a mask of the DNA channel was generated by thresholding using the Otsu method in Fiji. Next, the obtained binary image was converted to ROIs using the 'Analyze particles' function (size range: 5-infinity). Mitotic and interphase cells were differentiated manually based chromatin morphology. Within the obtained ROI per cell, the mean fluorescence intensity of the acetyl-mark was recorded, the extracellular background measured in a rectangular ROI subtracted and a ratio of histone mark over DNA mean intensity generated to account for changes in DNA compaction between the different conditions. For comparison of untreated interphase and mitotic cells, obtained ratios were normalized to the mean of untreated interphase cells (Extended Data Fig. 2a, b). For comparison of untreated and TSA-treated mitotic cells, ratios were normalized to the mean of untreated mitotic cells (Extended Data Fig. 2c, d). For comparison of p300-expressing mitotic cells, ratios were normalized to the mean of the mock-plasmid transfected mitotic cells (Extended Data Fig. 3a, b).

Measurement of Cyclin B1 stain

In interphase mitotic cells, determined by absence or presence of cell rounding, in the central section of the recorded Z-stack (7 Z-slices, 1 µm each, central section manually determined), the cell outline in DIC images was used to determine a ROI per cell. The total fluorescence intensity of the CyclinB1 fluorescence within this ROI was recorded in Fiji. The values were normalized to the mean of the CyclinB1 stain in interphase cells.

Determination of coefficient of variation of chromatin droplets *in vitro*

In entire fields of chromatin droplets or nucleosome array solution (Extended Data Fig. 4e) (both recorded ~3 μm above the cover glass using laser powers adjusted to the unmodified condition), the mean fluorescence intensity and standard deviation was measured, and the coefficient of variation ($CV=\alpha\,\mu^{-1}$) was calculated.

Airyscan processing and deconvolution

Raw images recorded using the Airyscan2 detector using AS-SR or multiplex airyscan modes were processed using ZEN3.3 Blue 2020 software.

Fiji version details

The Fiji-integrated distribution/version used for analyses in this study was ImageJ 1.53c, using Java 1.8.0_66 (64-bit), with in part custom ImageJ plugins as indicated.

Statistical analyses and data reporting

No statistical methods were used to predetermine sample size. Data were tested for normality and equal variances with Shapiro–Wilk/D'Agostino–Pearson and F-test/Levene's tests (α = 0.05), respectively. The appropriate statistical test was chosen as follows: Data were tested for normality. Unpaired, normally distributed data were tested with a two-tailed *t*-test (in the case of similar variances) or with a two-tailed *t*-test with Welch's correction (in the case of different variances). Unpaired, not-normally distributed data were tested with a two-tailed Mann–Whitney test (in the case of similar variances) or with a two-tailed Kolmogorov–Smirnov test (in the case of different variances). Paired, normally distributed data were tested with two-tailed *t*-test and paired, not-normally distributed data were tested with a Wilcoxon matched-pairs signed rank test. When manual annotation was required, blinding precautions were made.

Sample numbers

Fig. 1a, b: representative examples and quantification of chromatin fraction at spindle center: Control (*n*=51 cells), ΔCondensin (*n*=65 cells), ΔCondensin+TSA (*n*=34 cells), TSA (*n*=61). Fig. 1c: quantification of DNA density: Control (*n*=31 cells), ΔCondensin (*n*=89 cells), ΔCondensin+TSA (*n*=99 cells), TSA (*n*=74). Fig. 1d,e: representative examples and quantification of microtubule densities: Control (*n*=4 tomograms from 3 different cells), TSA (*n*=4 tomograms from 3 different cells). Fig. 1f: quantification of microtubule segment length in cytoplasm: Control (*n*=4 tomograms from 3 different cells), TSA (*n*=4 tomograms from 3 different cells). Fig. 2a, b: representative example and quantification of 11 cells, 3 ROIs per cell. Fig. 2c, d: representative examples and quantification of 8 cells (Undigested) and 10 cells (AluI-digested). Fig. 2e, f: Representative example and quantification of 11 cells, 3 ROIs per cell. Fig. 2g, h: Representative example and quantification of 13 cells. Fig. 2i, j: Representative example and quantification of 8 cells. Fig. 2k, l: Representative example and quantification of 10 cells. Fig. 2m, n: Representative example and quantification of 28 cells. Fig. 3a: Representative example of an untreated metaphase cell (*n*=27). Fig. 3a, b: Representative examples and quantification of nocodazole treated cells: Control (*n*=46), TSA (*n*=31). Fig. 3c, d: Representative examples and quantification of: DsRed (*n*=26), DsRed(-7e) (*n*=26), DsRed(+9e) (*n*=26). Fig. 3e, f: Representative examples and quantification of: Nocodazole (*n*=94 from 45 fields of droplets), polymerized microtubules (*n*=13 fields of droplets). Fig. 4 a, b: Representative example and quantification of 15 cells. Extended Data Fig. 1a, b: Representative examples and quantification of HeLa WT (*n*=25), HeLa Smc4-mAID-Halo (*n*=25), HeLa Smc4-mAID-Halo + 5-PhIAA (*n*=25). Extended Data Fig. 1d: Representative examples of in total recorded cells: Control (*n*=20), ΔCondensin (*n*=20), ΔCondensin+TSA (*n*=45), TSA (*n*=40). Extended Data Fig. 1e: Quantification of mitotic duration in control (*n*=44) and TSA-treated (*n*=36) cells. Extended Data Fig. 1f, g: Representative examples and quantification of control (*n*=64) and TSA-treated (*n*=110). Extended Data Fig. 2a, b: Representative examples and quantification of interphase (H2B-Ac (*n*=20), H3-Ac (*n*=20), H4K16-Ac (*n*=20)) and mitotic (H2B-Ac (*n*=20), H3-Ac (*n*=20), H4K16−Ac (*n*=20)) cells. Extended Data Fig. 2c, d: Representative examples and quantification of control (see Extended Data Fig. 2b) and TSA treated (H2B-Ac (*n*=20), H3-Ac (*n*=20), H4K16−Ac (*n*=20)). Extended data Fig. 2e, f: Representative examples and quantification of interphase (*n*=60), untreated mitotic (*n*=89), ΔCondensin (*n*=59), ΔCondensin+TSA (*n*=83), TSA (*n*=67). Extended Data Fig. 3a, b: representative examples and quantification of mock (*n*= 20), $p300_{HAT}$ (*n*=26), p300(D1399Y) (*n*=20) transfected cells. Extended Data Fig. 3c, d, e: representative examples and quantification of chromatin fraction at spindle center (d) and chromatin density (e) of mock (*n*=20), ΔCondensin+$p300_{HAT}$ (*n*=20), ΔCondensin+300(D1399Y) (*n*=24) transfected cells. Extended Data Fig. 4a, b: Representative example and

quantification of 7 cells, 3 ROIs per cell. Extended Data Fig. 4c, d: Representative example and quantification of 11 cells. Extended Data Fig. 4e, f: Representation examples and quantification of fields of unmodified (AF488: *n*=26, AF594: *n*=25) and acetylated (AF488: *n*=25, AF594: *n*=30) nucleosome arrays. Extended Data Fig. 5a, b: Representative examples and quantification of microinjected mEGFP (*n*=17) and scGFP(*n*=20). Extended Data Fig. 5c, d: Representative examples and quantification of microinjected FITC-dextran (-) (*n*=21) and FITC-DEAE-dextran (+) (*n*=10). Extended Data Fig. 5e, f: Representative examples and quantification of nucleosome array droplets with mEGFP (*n*=69) and scGFP (*n*=73). Extended Data Fig. 5g, h: Representative examples and quantification of nucleosome array droplets with FITC-dextran (-) (*n*=69) and FITC-DEAE-dextran (+) (*n*=57). Extended Data Fig. 6 a, b: Representative example and quantification of 13 cells. Extended Data Fig. c, d: Representative example and quantification of 16 cells. All experiments in this study were performed in at least 2 biological replicates.

Data availability

Raw microscopy data are available from the corresponding authors upon request, given the large file sizes that are involved.

Code availability

All of the steps of the image analyses that were performed in this study are described in detail to allow reproduction of the results. The corresponding authors will provide the code upon request.

Methods references

51. Schmitz, M. H. A. *et al.* Live-cell imaging RNAi screen identifies PP2A-B55α and importin-β 21 as key mitotic exit regulators in human cells. *Nature Cell Biology* **12**, 886–893 (2010).
52. Samwer, M. *et al.* DNA Cross-Bridging Shapes a Single Nucleus from a Set of Mitotic Chromosomes. *Cell* **170**, 956-972.e23 (2017).
53. Gutschner, T., Haemmerle, M., Genovese, G., Draetta, G. F. & Chin, L. Post-translational Regulation of Cas9 during G1 Enhances Homology-Directed Repair. *Cell Reports* **14**, 1555–1566 (2016).
54. Li, S., Prasanna, X., Salo, V. T., Vattulainen, I. & Ikonen, E. An efficient auxin-inducible degron system with low basal degradation in human cells. *Nat Methods* **16**, 866–869 (2019).
55. Thompson, D. B., Cronican, J. J. & Liu, D. R. Engineering and identifying supercharged proteins for macromolecule delivery into mammalian cells. *Methods in enzymology* **503**, 293–319 (2012).
56. Dixit, R. & Ross, J. L. Chapter 27 - Studying Plus-End Tracking at Single Molecule Resolution Using TIRF Microscopy. in *Methods in Cell Biology* (eds. Wilson, L. & Correia, J. J.) vol. 95 543–554 (Academic Press, 2010).
57. Field, C. M., Pelletier, J. F. & Mitchison, T. J. Chapter 24 - Xenopus extract approaches to studying microtubule organization and signaling in cytokinesis. in *Methods in Cell Biology* (ed. Echard, A.) vol. 137 395–435 (Academic Press, 2017).
58. Mastronarde, D. N. Automated electron microscope tomography using robust prediction of specimen movements. *Journal of Structural Biology* **152**, 36–51 (2005).
59. Kremer, J. R., Mastronarde, D. N. & McIntosh, J. R. Computer Visualization of Three-Dimensional Image Data Using IMOD. *Journal of Structural Biology* **116**, 71–76 (1996).
60. Bancaud, A., Huet, S., Rabut, G. & Ellenberg, J. Fluorescence perturbation techniques to study mobility and molecular dynamics of proteins in live cells: FRAP, photoactivation, photoconversion, and FLIP. *Cold Spring Harbor protocols* **2010**, pdb.top90 (2010).

Acknowledgments

The authors thank the IMBA/IMP/GMI BioOptics and Molecular Biology Service and the VBCF Electron Microscopy and Protein Technologies facilities for technical support. The authors thank Iain Patten, Alexey Khodjakov, Helder Maiato, and Carsten Janke for comments on the manuscript. The authors thank Paul Batty for assistance with cell line generation and Angela M. Rodrigues Viana for advice and reagents for genome engineering. Research in the laboratory of D.W.G. is supported by the Austrian Academy of Sciences, the Austrian Science Fund (FWF; Doktoratskolleg "Chromosome Dynamics" DK W1238), and the Vienna Science and Technology Fund (WWTF; projects LS17-003 and LS19-001). Research in the laboratory of S.O. is supported by the Vienna Science and Technology Fund (WWTF; project LS19-001). Research in the laboratory of M.K.R. is supported by the Howard Hughes Medical Institute, a Paul G. Allen Frontiers Distinguished Investigator Award (to M.K.R.) and grants from the NIH (F32GM129925 to B.A.G.) and the Welch Foundation (I-1544 to M.K.R.). M.W.G.S. and M.P. have received a PhD fellowship from the Boehringer Ingelheim Fonds.

Author contributions

D.W.G. and M.W.G.S. conceived the project, with input from B.A.G. and M.K.R.. M.W.G.S. designed, performed, and analyzed all experiments, except those shown in Fig. 1 d-f (M.W.G.S. together with S.O), Figs. ED 4a, b, ED 5e-h (M.W.G.S. together with C.B.), Figs. ED 1 a, b, e, ED 2 a-d, ED 3 a-c (M.F.D.S.), Fig. 3 c, d (M.P.). B.A.G. and L.K.D. generated nucleosome arrays and developed *in vitro* chromatin condensate assays. C.C.H.L. developed image analysis procedures. D.W.G and M.K.R acquired funding and supervised the project. D.W.G and M.W.G.S wrote the manuscript, with input from all authors.

Competing interests

M.K.R. is a co-founder of Faze Medicines. The other authors declare no competing interests.

Additional information

Supplementary information is available for this paper.

Correspondence and requests for materials should be addressed to M.W.G.S. or D.W.G.

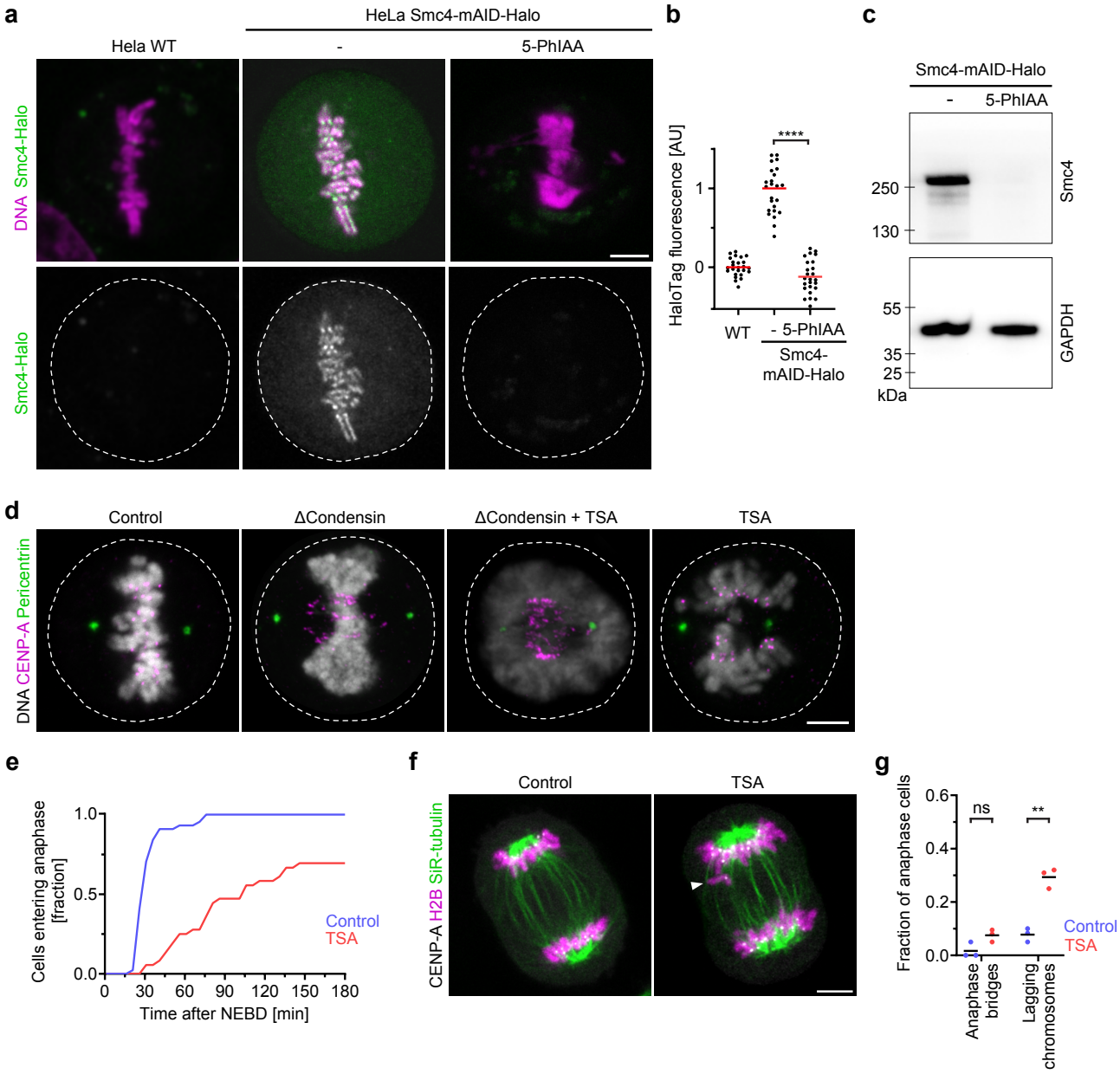

Extended Data Figure 1. Characterization of HeLa Smc4-mAID-HaloTAG cells and effect of TSA on chromosome segregation. a-c, Smc4 expression analysis. **a**, HeLa cells with homozygous Smc4-mAID-Halo alleles and stably expressing OsTIR(F74G) were analyzed with or without treatment of 5-Phenylindole-3-eacetic acid (5-PhIAA) for 3 hours and stained with OregonGreen-488 HaloTAG stain; HeLa wildtype (WT) cells serve as control to measure fluorescence background. DNA was stained with Hoechst 33342. **b**, Quantification of HaloTAG fluorescence in live mitotic cells. *n*=25 for WT, *n*=25 for Smc4-mAID-Halo without 5-PhIAA, *n*=25 for Smc4-mAID-Halo with 5-PhIAA. Bars indicate mean; significance was tested by a two-tailed Welch *t*-test (Smc4-mAID-Halo with 5-PhIAA, $P<10^{-15}$). **c,** Immunoblot analysis of Smc4-mAID-Halo cells with or without 3h 5-PhIAA treatment. **d**, Immunofluorescence analysis of centromeres and spindle poles in mitotic Smc4-mAID-Halo cells after 3 h degradation of Smc4 (ΔCondensin), 3 h treatment with TSA as indicated. Projection of 7 Z-sections. **e**. Mitotic progression analysis by time-lapse microscopy of HeLa cells expressing H2B-mRFP, in untreated control and TSA-treated cells. *n*=44 for control from 5 biological replicates, *n*=36 for TSA from 4 biological replicates. **f**. Chromosome missegregation analysis by live Airyscan imaging of HeLa cells expressing H2B-mCherry and mEGFP-CENP-A and stained with SiR-tubulin. Representative images of untreated controls or 3 h TSA-treated anaphase cells. Single Airyscan Z-slices. **g**. Quantification of chromosome missegregation as illustrated in **f**. Dots indicate biological replicates, bars indicate mean. *n*=64 cells for control, *n*=110 for TSA. Significance was tested by an unpaired, two-tailed *t*-test (anaphase bridges, *P*=0.052, lagging chromosomes. $P=1.209\text{x}10^{-3}$). Scale bars, 5 µm.

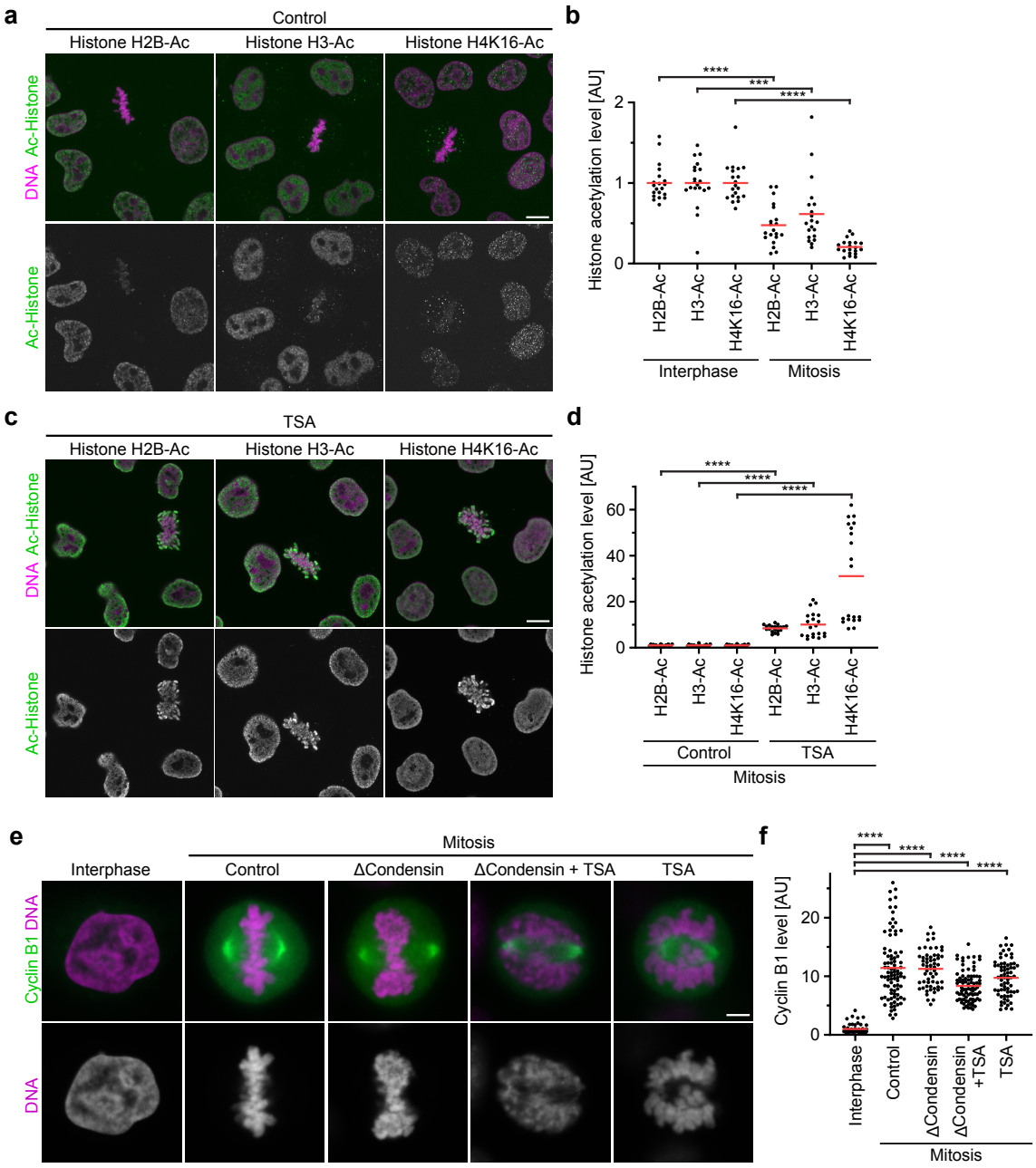

Extended Data Figure 2. Analysis of histone acetylation and cell cycle states. **a**,**b**, Immunofluorescence analysis of histone acetylation in interphase and mitosis. **a**, HeLa cells were fixed and stained with antibodies against different acetylated histones for immunofluorescence as indicated. **b**, Quantification of histone acetylation by immunofluorescence as in **a**, by the ratio of antibody fluorescence to DNA reference staining by Hoechst 33342. For each acetylated histone, all data points were normalized to the mean of interphase cells. *n*=20 for H2B-Ac, Interphase, *n*=20 for H3-Ac, Interphase, *n*=20 for H4K16-Ac, Interphase, *n*=20 for H2B-Ac, Mitosis, *n*=20 for H3-Ac, Mitosis, *n*=20 for H4K6-Ac, Mitosis. Bars indicate mean; significance was tested by a two-tailed Welch *t*-test (H2B-Ac, Mitosis, $P=2.572\text{x}10^{-8}$), or a two-tailed Mann-Whitney test (H3-Ac, Mitosis, $P=4.72\text{x}10^{-4}$), or a Kolmogorov-Smirnov test (H4K16Ac, Mitosis, *P*=4.122x). **c**,**d**, Histone acetylation in mitotic cells 3 h after TSA treatment. **c**, HeLa cells were treated with TSA for 3 h, fixed, and histone acetylation analyzed by immunofluorescence as in **a**. **d**, Quantification of histone acetylation as in b, comparing mitotic cells 3 h after TSA treatment with untreated control cells. For each acetylated histone antibody, all data points were normalized to the mean of control metaphase cells. *n*=20 for H2B-Ac, control, *n*=20 for H3-Ac, control, *n*=20 for H4K16-Ac, control, *n*=20 for H2B-Ac, TSA, *n*=20 for H3-Ac, TSA, *n*=20 for H4K16-Ac, TSA. Bars indicate mean; significance was tested by a two-tailed Welch *t*-test (H2B-Ac, TSA, $P<10^{-15}$; H3-Ac, TSA, $P=4.767\text{x}10^{-7}$) or a two-tailed Mann-Whitney test (H4K16-Ac, TSA, $P=1.451\text{x}10^{-11}$). **e**, **f**, Analysis of cell cycle state by immunofluorescence staining against Cyclin B1. HeLa cells with homozygously mAID-tagged SMC4 were treated with 5-PhIAA to deplete condensin (ΔCondensin) or with TSA to suppress mitotic histone deacetylation as indicated. DNA was stained with Hoechst 33342. Classification of interphase and mitotic cell is based on overall cell shape and spindle morphology. **f**, Quantification of Cyclin B1 fluorescence in cells as in **e**. Data normalized to the mean of untreated interphase cells. *n*=60 (interphase), *n*=89 (mitotic), *n*=59 (ΔCondensin), *n*=83 (ΔCondensin+TSA), *n*=67 (TSA) cells. Bars indicate mean; significance was tested by a two-tailed Mann-Whitney test (CTRL, $P<10^{-15}$); ΔCondensin, $P<10^{-15}$; ΔCondensin+TSA, $P<10^{-15}$; TSA, $P<10^{-15}$). Scale bars, **a**,**c**, 10 μm, **e**, 5 μm.

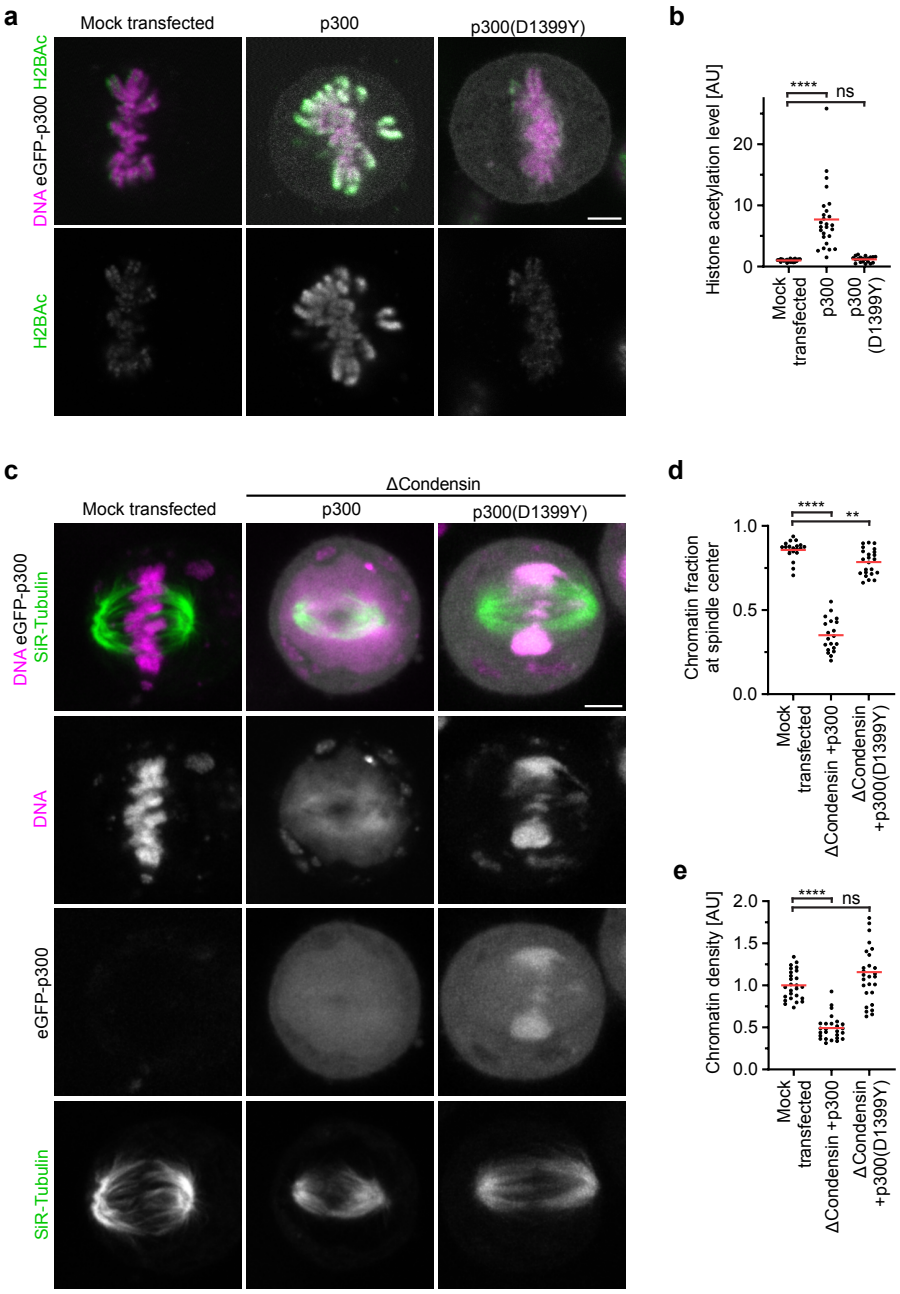

Extended Data Figure 3. Histone acetylation and chromosome organization in cells overexpressing eGFP-p300. **a**, **b**, Immunofluorescence analysis of histone acetylation in mitotic cells overexpressing p300 histone acetyltransferase or catalytically dead p300(D1399Y). **a**, Cells were transfected with a plasmid coding for eGFP-p300 or eGFP-p300 (D1399Y) and fixed after 48 h. Histone 2B acetylation was analyzed by immunofluorescence. DNA was stained with Hoechst 3342. **b**, Quantification of histone acetylation in metaphase cells as in **a**. Data points were normalized to the mean of mock-transfected mitotic cells. *n*=20 for mock-transfected, *n*=26 for p300, *n*=20 for p300 (D1399Y). Bars indicate mean; significance was tested by a two-tailed Mann-Whitney test (p300, P=3.57x10^{-13}) or a two-tailed Welch *t*-test (p300(D1399Y), P=0.138). **c**-**e**, Analysis of chromatin density and congression to spindle center in cells after SMC4-AID-Halo degradation (ΔCondensin) and overexpression of p300 or catalytically dead p300(D1399Y). **c**, Cells transfected with a plasmid coding for eGFP-p300 or eGFP-p300 (D1399Y) for 48 hours were stained with Hoechst 33342 and SiR-Tubulin and mitotic cells with bipolar spindles imaged live. Projection of 5 z-sections. **d**, Quantification of chromosome congression by the fraction of chromatin localizing to the central spindle region. *n*=20 for mock-transfected, *n*=24 for ΔCondensin+p300, *n*=20 for ΔCondensin+p300(D1399Y). Bars indicate mean; significance was tested by a Kolmogorov-Smirnov test (ΔCondensin+p300, P=4.122x10^{-9}) or a two-tailed Mann-Whitney test (ΔCondensin+p300(D1399Y), P=1.72x10^{-3}). **e**, Quantification of chromatin density in cells treated as in **c**. *n*=20 for mock-transfected, *n*=24 for ΔCondensin+p300, *n*=20 for ΔCondensin+p300(D1399Y). Bars indicate mean; significance was tested by a two-tailed Mann-Whitney test (ΔCondensin+p300, P=7.86x10^{-13}) or a two-tailed Welch *t*-test (ΔCondensin+p300(D1399Y), P=0.051). Scale bars, 5 µm.

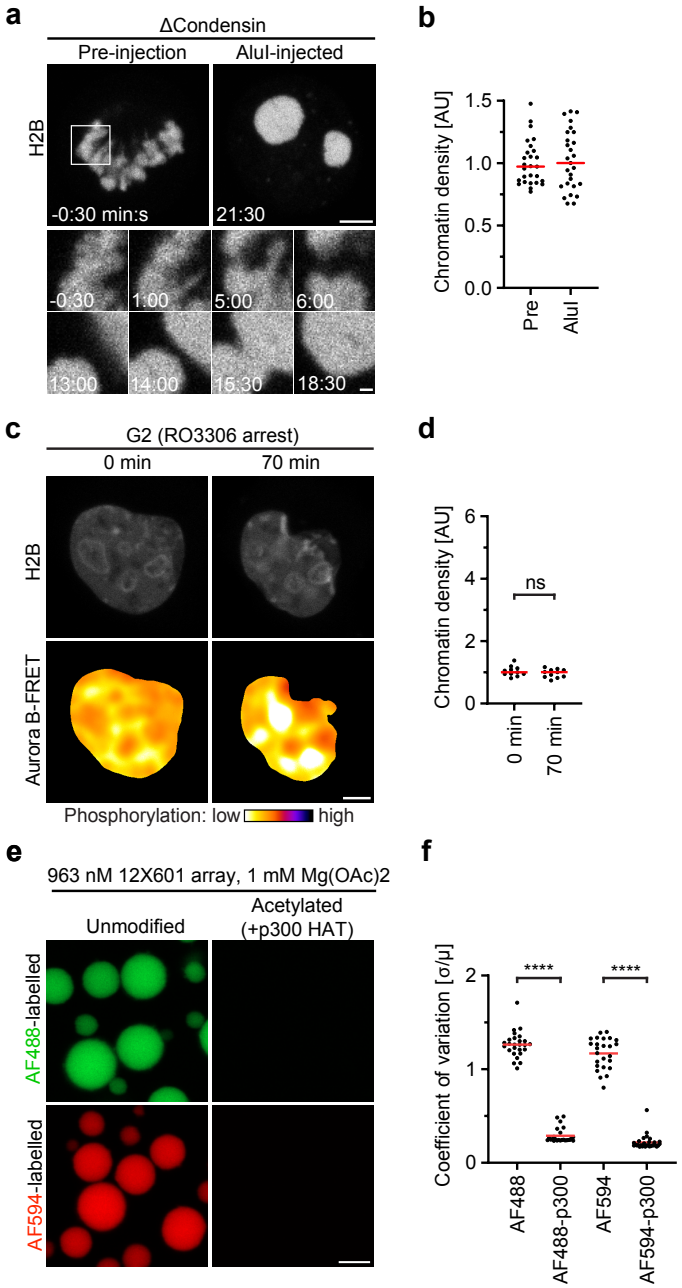

Extended Data Figure 4. Phase separation behavior of chromatin fragments. **a**, **b**, Condensin is not required for liquid phase separation of chromatin fragments in mitotic cells. **a**. Smc4-AID HeLa cells expressing H2B-mCherry were treated 3 h with 5-PhIAA to deplete condensin and a mitotic cell was then injected with AluI (t=0 min) and imaged by time-lapse microscopy. **b**, Quantification of chromatin density before and after injection of AluI, normalized to the mean of untreated pre-injection cells. *n*=7 cells, 3 ROIs each. Bars indicate mean. **c**, **d**, Chromatin fragments do not undergo liquid phase separation in G2 cells. **c**, HeLa cell expressing Aurora B-FRET biosensor was synchronized to G2 by RO3306 and microinjected in the nucleus with AluI. G2 state was retained in presence of RO3306 as indicated by FRET signal. t=0 minutes refers to the first timepoint of the recorded time-lapse. **d**, Quantification of chromatin density in cells as in **c**, normalized to the mean of t=0 min. *n*=11 cells. Bars indicate mean; significance tested by a paired, two-tailed *t*-test (*P*=0.091). **e**, **f**, In vitro liquid-liquid phase separation behavior of unmodified or acetylated nucleosome arrays. **e**, 12X601 Nucleosome arrays labelled with fluorophores as indicated were treated with recombinant p300 histone acetyltransferase or no enzyme *in vitro* and then subjected to identical phase separation buffers for 30 minutes. **f**, Quantification of nucleosome array self-association by coefficient of variation (CV= σ/μ) in images as in **e**. *n*=26 for AlexaFlour488 array (AF488), *n*=25 for acetylated AlexaFluor488 array (AF488-p300), *n*=25 for AlexaFluor594 array (AF594), *n*=30 for acetylated AlexaFluor594 array (AF594-p300). Bars indicate mean; significance tested by a Kolmogorov-Smirnov test (AF488-p300, $P=1.701\times10^{-11}$; AF594-p300, $P=2.862\times10^{-12}$). Scale bars, 5 μm, **a**, insert 1 μm.

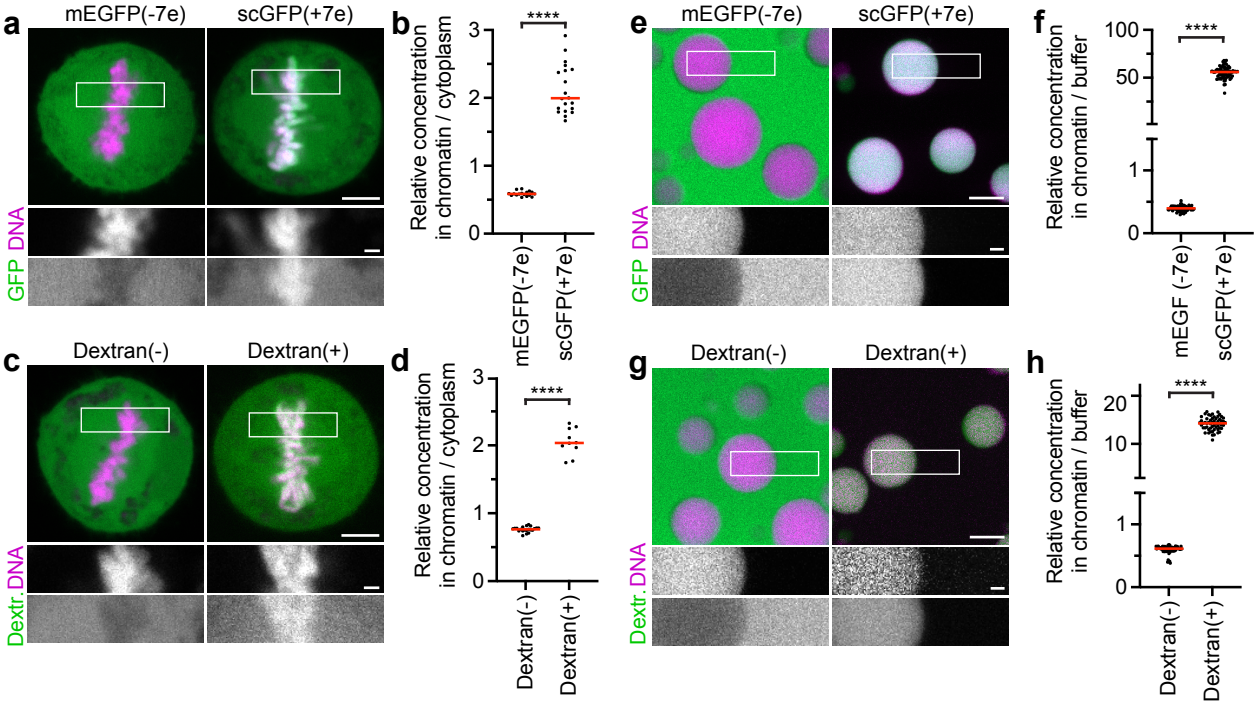

Extended Data Figure 5. Partitioning of proteins and dextrans relative to chromatin depends on electrical charge. a, **b**, Partitioning of GFP surface charge variants relative to chromatin in metaphase cells. **a**, Live metaphase cells after injection of recombinant mEGFP(-7e) or scGFP(+7e). DNA stained with Hoechst 33342. **b**, Quantification of GFP fluorescence in chromatin relative to cytoplasm. *n*=17 for mEGFP(-7e), *n*=20 for scGFP(+7e). Bars indicate mean; significance tested by a two-tailed Welch *t*-test (P=5.6x10^{-14}). **c**, **d**, Partitioning of charge-modified fluorescent dextrans relative to chromatin in metaphase cells. **c**, Live metaphase cells after injection of negatively or positively charged 4.4 kDa dextrans. DNA stained with Hoechst 33342. **d**, Quantification of dextran fluorescence in chromatin relative to cytoplasm. *n*=21 for 4.4 kDa dextran (-), *n*=10 for 4.4 kDa dextran(+). Bars indicate mean; significance tested by a two-tailed Welch *t*-test (P=4.553x10^{-9}). **e**, **f**, Partitioning of GFP surface charge variants relative to liquid droplets of nucleosome arrays *in vitro*. **e**, Liquid chromatin droplets were formed *in vitro* by exposing 12X601 nucleosome arrays to phase separation buffer. GFP charge variants were added for 10 minutes and then imaged. DNA was stained with Hoechst 33342. **f**, Quantification of GFP fluorescence in chromatin relative to buffer. *n*=69 for mEGFP(-7e), *n*=73 for scGFP(+7e). Bars indicate mean; significance tested by a two-tailed Welch *t*-test (P<10^{-15}). **g**, **h**, Partitioning of charge modified dextrans relative to liquid droplets of nucleosome arrays *in vitro*. **g**, Liquid chromatin droplets were formed were formed as in **e**. Charge modified 4.4 kDa dextrans were added for 10 minutes and then imaged. DNA was stained with Hoechst 33342. **h**, Quantification of dextran fluorescence in chromatin relative to buffer. *n*=69 for 4.4 kDa dextran(-), *n*=57 for 4.4 kDa dextran(+). Bars indicate mean; significance tested by a two-tailed Mann-Whitney test (P<10^{-15}). Scale bars, 5 μm, inserts 1 μm.

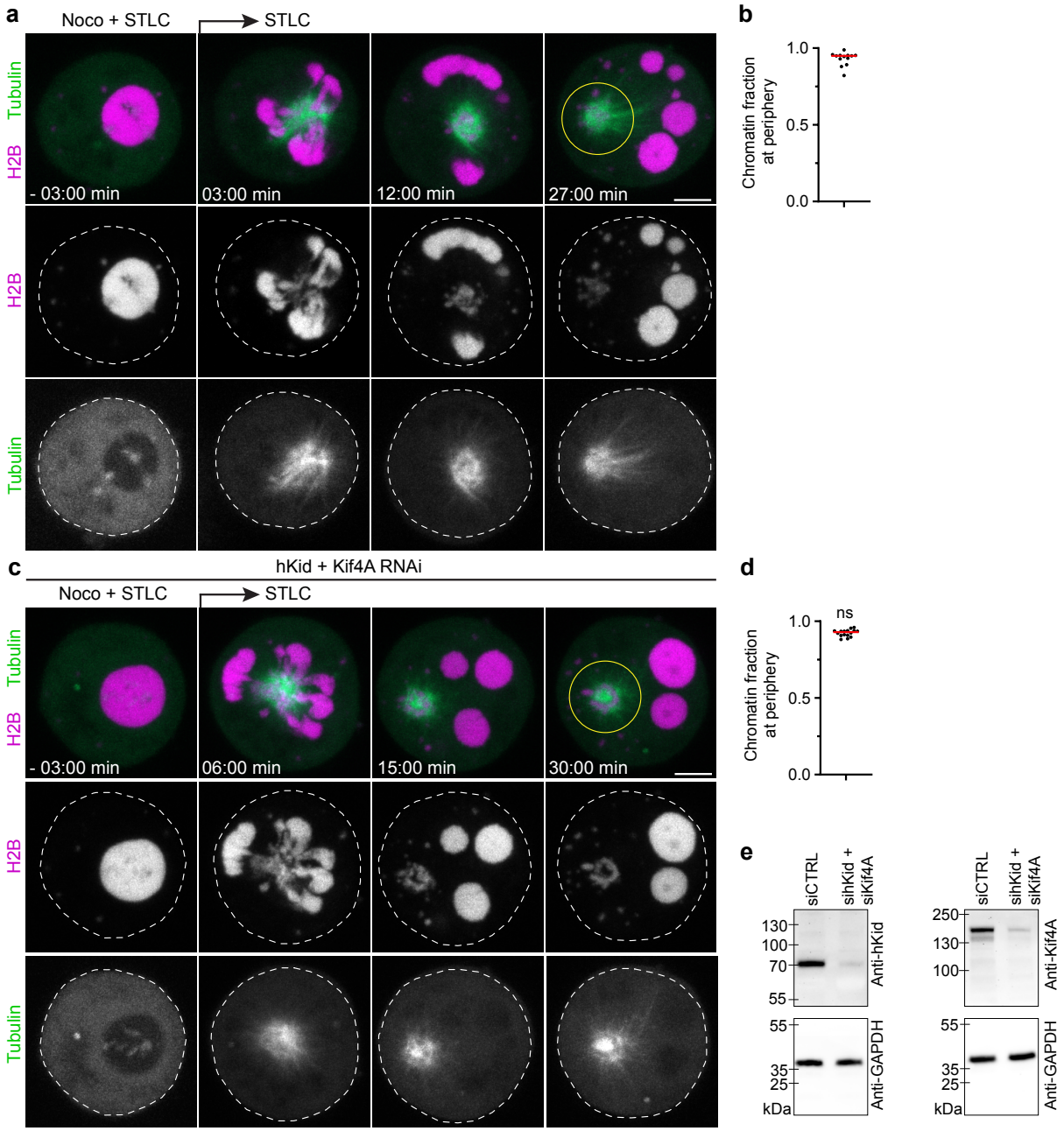

Extended Data Figure 6. Microtubules push liquified chromatin away from the spindle pole independently of hKid and Kif4A. a, Time-lapse microscopy of liquified chromatin during chemically-induced assembly of monopolar spindles. Live mitotic HeLa cells expressing H2B-mCherry and eGFP-α-tubulin were treated with nocodazole and STLC and then injected with AluI. Nocodazole was removed at t=0 min during time-lapse imaging. Projection of 4 z-sections. **b**, Quantification of chromatin localization at the cell periphery relative to the region around the spindle monopole at = 36 min. *n*=13 cells. **c,** Time-lapse microscopy of liquified chromatin during spindle assembly as in **a** for cells depleted of Kid and Kif4a by RNAi. **d,** Quantification as in **b** for hKid/Kif4a-RNAi cells. *n*=16 cells. Bar indicates mean; significance tested by a two-tailed Mann-Whitney test (*P*=0.215) **e,** Validation of RNAi efficiency by Western Blotting. Samples were collected 30 h after transfection of siRNAs targeting hKid and Kif4a and probed by antibodies as indicated. Scale bars, 5 μm.

4 Discussion

4.1. Mechanisms for cytoplasmic separation from chromosomes in open mitosis

Re-establishing cellular compartmentalization after open mitosis is essential for proper gene expression in newly forming daughter cells. Here I describe a novel mechanism, termed chromosome clustering, which mediates unmixing of bulk cytoplasm from chromosomes before the nuclear envelope seals around the chromosome cluster. I show that chromosome clustering happens in the absence of mitotic spindle and causes exclusion of large artificial substrates (GEM particles, p.27, Fig. 2c, d, [148]) as well as endogenous macromolecular assemblies (mature ribosomes, p.29, Fig. 4d-f, [148]). Hence, chromosomes have an inherent ability to protect the reforming nucleus from cytoplasmic invasion.

In the presence of microtubules, chromosome coalescence to a cluster might further be assisted by the spindle forces during poleward segregation. While the spindle is dispensable in cytoplasmic exclusion (p.27, Fig. 2c, d, [148]), the relative contributions of spindle pulling forces and Ki-67-regulated chromosome clustering in unperturbed mitosis remain unclear. The methods we developed to inhibit chromosome clustering during spindle-less mitosis led to cytoplasmic retention in the nuclei of daughter cells, but also prevented progression to anaphase, thereby limiting the analysis of spindle forces during anaphase. Further dissection of Ki-67's function in a regular anaphase situation might be achieved by acute Ki-67 depletion. The growing toolbox of inducible protein degradation systems[149–152] should make it feasible to design such an experiment in the close future.

Chromosome clustering excludes large cytoplasmic components from inter-chromosomal spaces and thereby causes unmixing of cytoplasm and chromatin. However, some cytoplasmic organelles do not enter the space occupied by mitotic spindle during open mitosis. In *Drosophila melanogaster* S2 cells, which undergo semi-open mitosis, a membranous envelope excludes organelles to the periphery, and concentrates spindle and SAC-essential components to chromosome-proximal regions, while laser microsurgery disrupted this compartmentalization[98]. Human cells completely disassemble the NE during mitotic entry, NE membranes are recycled into the ER, which forms a network that surrounds the mitotic spindle[2]. This membranous network is not impermeable for the diffusion of small protein substrates, but it is proposed to keep large membranous organelles, such as mitochondria, away from the mitotic spindle[98]. Other studies report that mitochondria retain their peripheral localization through interactions with subcortical actin filaments[144]. Interestingly, although it is conceivable that the mitotic spindle itself may impose a steric barrier for organelle diffusion into central cellular regions, spindle drug depolymerization did not lead to chromosome intermixing with mitochondria, ER membranes nor lysosomes[98].

Taken together, apart from chromosome clustering, faithful compartment re-establishment in the newly forming daughter cells involves additional mechanisms, including the mitotic spindle, ER membranes, and other cytoskeletal elements.

4.2. Potential molecular basis for Ki-67-mediated clustering

In early mitosis Ki-67 adopts an extended conformation, with highly positively charged molecular brushes perpendicularly extending from the surface of chromosomes towards the cytoplasm. This contributes to chromosome individualization and enables independent chromosome motility. Chromosomes lacking Ki-67 show increased adhesion and cluster together already in prometaphase[113]. Therefore, we speculate that regulated increase in chromosomal surface adhesion during mitotic exit stabilizes contacts between chromosomes and causes clustering. My collaboration partner, S. Cuylen-Haering shows that upon mitotic exit induction, Ki-67 changes its conformation and extended brushes collapse on the surface of mitotic chromosomes (p.28, Fig. 3a-d, [148]). Such conformational change is necessary for chromosome clustering, yet the details of how it contributes to surface adhesion remain to be investigated.

Chromosome individualization can be re-established in the absence of Ki-67 through overexpression of core histones[113], conceivably through mimicking the positive charge that may provide electrostatic repulsion between chromosomes. Whether the conformational change of Ki-67 also includes neutralization of electrical charge is an interesting open question. S. Cuylen-Haering confirmed that Ki-67 interaction with PP1 is dispensable for both chromosome clustering and conformational change (p.45-46, Extended Data Fig. 8d, e), however other unknown interactors may still contribute to Ki-67-mediated clustering.

4.3. Consequences of ribosomal retention in the nucleus

It has been proposed that ribosomes might contribute to mRNA translation inside the nucleus of vertebrate cells[153–155], but these findings have remained controversial. Several arguments speak against nuclear protein synthesis. Firstly, many initiation, elongation and termination factors would need to be present in the nucleus to enable translation. Live cell fluorescent imaging showed that less than 1% of these factors localize in the cell nucleus[156]. In addition, several nuclear export receptors were shown to specifically transport these factors outside of the nucleus[157]. Further on, the strongest arguments for nuclear translation were obtained from isolated nuclei[153], raising the question of purity of the isolate. Optimization of the nuclear isolation protocol decreased the levels of nuclear amino acid incorporation to almost

undetectable, indicating that the initially reported incorporation likely came from cytoplasmic contaminations[155]. Another important issue is the integrity of the NE, which might have been compromised by detergent treatment during isolation and could explain the accumulation of translation factors within the nuclei. Finally, an attempt was made to detect nuclear translation in cells, using nascent chain puromycylation combined with elongation inhibitors to immobilize the nascent chain on ribosomes[154]. The localization of translated chains was then detected using anti-puromycin antibodies, which required detergent treatment to ensure antibody accessibility. The authors verify that chemical treatment causes retention of nascent chains on ribosomes, yet the mobility of the whole ribosome-nascent peptide complex in the cytoplasm depends on the order of fixation and permeabilization events. Since both fixation and permeabilization were done simultaneously, the evidence for nuclear translation remains under question due to possible cytoplasmic leakage into the nucleus. Taken together, the presence of mature translationally competent ribosomes in the cell nucleus remains an exception rather than a physiological state. In the absence of chromosome clustering, all mature ribosomes localized between mitotic chromosomes are enclosed by the nuclear envelope at the end of mitosis (p.29, Fig. 4e, f, [148]). This exposes unprocessed pre-mRNAs inside the nucleus to an active protein translation machinery, potentially along with necessary cofactors. This mislocalization of ribosomes might lead to synthesis of dysfunctional proteins owing to translation of pre-mRNAs, which would threaten cellular homeostasis. Whether and how ribosome mislocalization after mitotic exit with perturbed chromosome clustering leads to protein synthesis defects might be addressed by mass-spectrometric analysis of proteomes of unperturbed versus clustering-deficient cells.

After ribosomal assembly in the cytoplasm, the adaptor proteins carrying NES are released from the complex, disabling further binding to nuclear export receptors[84]. It is therefore unclear whether mature ribosomes that localize in the cell nucleus, as for example after an open mitosis in clustering deficient cells, could be exported via nuclear pores. Although our preliminary observations indicate that fluorescent signal from mature ribosomes may persist in the nucleus for several hours after mitotic exit, follow up experiments are necessary to determine whether this affects nuclear processes. In addition, although mature ribosomes are too large to be transported through the NPCs in their native conformation, there is increasing evidence that the pore size might transiently increase for transport of large substrates. A recent study highlights that HIV capsids of 60 nm diameter can be inserted into the central channel of the nuclear pore without major structural changes to the NPC[78]. Therefore, the possibility of mature ribosome export cannot be completely ruled out based on size constraint considerations. Follow-up experiments investigating nuclear translation and other potential

deficiencies of clustering-incompetent cells will be necessary to clarify the physiological role of nucleo-cytoplasmic compartmentalization by this mechanism in proliferating cells.

4.4. Molecular partitioning relative to compact mitotic chromosomes during open mitosis

Chromosomes cluster before nuclear envelope sealing to exclude large cytoplasmic molecules from inter-chromosomal spaces. This cytoplasmic displacement mechanism first relies on exclusion of cytoplasmic molecules from mitotic chromatin (p.26, Fig. 1b, [148]). We show that molecules of much smaller size than GEM particles can still be excluded from mitotic chromosomes, such as fluorescent GFP molecules (p.75, Extended Data Fig. 5a, b, [147]). Altering electrical charge of similarly sized proteins has led to opposite distributions relative to mitotic chromosomes (p.58, Fig. 3c, d, [147]). Therefore, electrical charge is a key regulator of molecular access to chromosomes. An interesting follow-up to these findings would combine the effects of both molecule size and electrical charge to gain a systematic insight into cytoplasmic distribution relative to chromosomes. Further on, M.W.G. Schneider shows that fluorescent protein distribution depends on the acetylation state of mitotic chromatin (p.58, Fig. 3a, b, [147]). This might be explained by a change in mitotic chromatin pore size due to hyperacetylation-induced decompaction. Larger pores of decompacted chromatin might facilitate access of cytoplasmic molecules. However, the compaction state and pore size of chromatin might not be the only feature affected by hyperacetylation. Addition of acetyl groups to histone tails neutralizes the positive charge of their lysine residues and changes the overall electrical charge of chromatin, which we show is relevant for protein partitioning. Systematic altering of the chromatin compaction state in combination with exploring a wider range of sizes and charges of cytoplasmic molecules will reveal more about underlying principles of compartmentalization during open mitosis.

The observed macromolecular exclusion mechanism during nuclear assembly raises the question how components that need to be incorporated in the nucleus after open mitosis avoid exclusion via clustering. Nuclear retention after an open mitosis might be achieved by binding to the chromosome surface. Consistent with this idea, many pre-ribosomal RNAs and nucleolar proteins are localized to a chromosome periphery compartment that remains bound to chromosomes throughout mitotic exit, so that they are enwrapped by the reforming nuclear envelope regardless of chromosome clustering. Depletion of Ki-67 causes displacement of these components from the chromosome surface to the cytoplasm, and their uneven distribution between newly forming daughter cells[52]. Cells lacking Ki-67 have fewer nucleoli and decreased levels of RNA-synthesis, possibly because essential components for nucleolar

reformation are not incorporated into the nucleus on time. Alternatively, electrical charge, or yet undescribed molecular features might further govern immediate inclusion into nuclei along with chromosomes.

From a partitioning point of view, the chromosome periphery represents a unique entity whose components do not enter chromosomal bodies yet are not completely excluded to the cytoplasm. Hence, chromosome periphery components might reveal additional features responsible for molecular distribution relative to chromosomes (3D conformation, charge localization, hydrophobicity etc.). Uncovering the principles of molecular distribution between chromatin, periphery and cytoplasm during open mitosis will provide a better understanding of how cellular compartmentalization is re-established at mitotic exit.

5 Conclusion

The results presented in this work reveal a new mechanism for re-establishing nucleo-cytoplasmic compartmentalization after open mitosis that involves clustering of chromosomes regulated by the chromosome periphery protein Ki-67. In addition, we show that exclusion of soluble proteins from compact mitotic chromosomes depends on the electrical charge of the protein, whereby negative charge contributes to chromosome-cytoplasmic unmixing. Taken together, this study provides key insights into how cellular compartmentalization is regulated and maintained throughout cell division to ensure homeostasis of newly emerging daughter cells.

6 Abbreviations

APC	anaphase promoting complex
BAF	barrier-to-autointegration factor
CAS	cellular apoptosis susceptibility
CDC	cell division control protein
CDH1	CDC20 homologue 1
CDK	cyclin-dependent kinase
DFC	dense fibrillar component
DNA	deoxyribonucleic acid
eGFP	enhanced green fluorescent protein
ER	endoplasmic reticulum
ESCRT	endosomal sorting complex required for transport
FC	fibrillar center
GC	granular component
GFP	green fluorescent protein
HAT	histone acetyltransferase
HDAC	histone deacetylases
HP1	heterochromatin protein 1
INM	inner nuclear membrane
LBR	lamin B receptor protein
LINC	linker of nucleoskeleton and cytoskeleton
LLPS	liquid-liquid phase separation
MCC	mitotic checkpoint complex
mRNA	messenger RNA
NE	nuclear envelope
NEBD	nuclear envelope break down
NES	nuclear export signal
NLS	nuclear localization signal
NOR	nucleolar organizer regions
NPC	nuclear pore complex
NTF2	nuclear transport factor 2
NTR	nuclear transport receptor

NUP	nucleoporin
ONM	outer nuclear membrane
Rb	retinoblastoma
RNA	ribonucleic acid
RNP	ribonucleoprotein
rRNA	ribosomal RNA
SAC	spindle assembly checkpoint
SMC	structural maintenance of chromosomes
snoRNP	small nucleolar ribonucleoproteins
TSA	trichostatin A
VRK	vaccinia-related kinase

7 References

1. Obaya, A. J. & Sedivy, J. M. *Review Regulation of cyclin-Cdk activity in mammalian cells*. *CMLS, Cell. Mol. Life Sci* **59**, (2002).

2. Ungricht, R. & Kutay, U. Mechanisms and functions of nuclear envelope remodelling. *Nat. Rev. Mol. Cell Biol.* **18**, 229–245 (2017).

3. Alberts, Bruce, Alexander Johnson, Julian Lewis, Martin Raff, Keith Roberts, P. W. *Molecular Biology of the Cell*. (Garland Science, 2002).

4. Malumbres, M. & Barbacid, M. Mammalian cyclin-dependent kinases. *Trends in Biochemical Sciences* **30**, 630–641 (2005).

5. Aktas, H., Cai, H. & Cooper, G. M. Ras links growth factor signaling to the cell cycle machinery via regulation of cyclin D1 and the Cdk inhibitor p27KIP1. *Mol. Cell. Biol.* **17**, 3850–3857 (1997).

6. Kato, J., Matsushime, H., Hiebert, S. W., Ewen, M. E. & Sherr, C. J. Direct binding of cyclin D to the retinoblastoma gene product (pRb) and pRb phosphorylation by the cyclin D-dependent kinase CDK4. *Genes Dev.* **7**, 331–342 (1993).

7. Ikeda, M. A., Jakoi, L. & Nevins, J. R. A unique role for the Rb protein in controlling E2F accumulation during cell growth and differentiation. *Proc. Natl. Acad. Sci. U. S. A.* **93**, 3215–3220 (1996).

8. Lundberg, A. S. & Weinberg, R. A. Functional Inactivation of the Retinoblastoma Protein Requires Sequential Modification by at Least Two Distinct Cyclin-cdk Complexes. *Mol. Cell. Biol.* **18**, 753–761 (1998).

9. Leone, G., Degregori, J., Jakoi, L., Cook, J. G. & Nevins, J. R. Collaborative role of E2F transcriptional activity and G1 cyclin-dependent kinase activity in the induction of S phase. *Proc. Natl. Acad. Sci. U. S. A.* **96**, 6626–6631 (1999).

10. Elledge, S. J. *et al.* CDK2 encodes a 33-kDa cyclin A-associated protein kinase and is expressed before CDC2 in the cell cycle. *Proc. Natl. Acad. Sci. U. S. A.* **89**, 2907–2911 (1992).

11. Petersen, B. O., Lukas, J., Sørensen, C. S., Bartek, J. & Helin, K. Phosphorylation of mammalian CDC6 by cyclin A/CDK2 regulates its subcellular localization. *EMBO J.* **18**, 396–410 (1999).

12. C, H. *et al.* HIRA, the human homologue of yeast Hir1p and Hir2p, is a novel cyclin-cdk2 substrate whose expression blocks S-phase progression. *Mol. Cell. Biol.* **21**, 1854–1865 (2001).

13. Ohtoshi, A., Maeda, T., Higashi, H., Ashizawa, S. & Hatakeyama, M. Human p55(CDC)/Cdc20 associates with cyclin A and is phosphorylated by the cyclin A-Cdk2 complex. *Biochem. Biophys. Res. Commun.* **268**, 530–534 (2000).

14. Mailer, J. L. Mitotic control. *Curr. Opin. Cell Biol.* **3**, 269–275 (1991).

15. Macaulay, C., Meier, E. & Forbes, D. J. Differential mitotic phosphorylation of proteins of the nuclear pore complex. *J. Biol. Chem.* **270**, 254–262 (1995).

16. Long, J. J., Leresche, A., Kriwacki, R. W. & Gottesfeld, J. M. Repression of TFIIH Transcriptional Activity and TFIIH-Associated cdk7 Kinase Activity at Mitosis. *Mol. Cell. Biol.* **18**, 1467–1476 (1998).

17. Keryer, G., Celati, C. & Klotz, C. In isolated human centrosomes, the associated

kinases phosphorylate a specific subset of centrosomal proteins. *Biol. Cell* **84**, 155–165 (1995).

18. Hendrickson, M., Madine, M., Dalton, S. & Gautier, J. Phosphorylation of MCM4 by cdc2 protein kinase inhibits the activity of the minichromosome maintenance complex. *Proc. Natl. Acad. Sci. U. S. A.* **93**, 12223–12228 (1996).

19. McLean, J. R., Chaix, D., Ohi, M. D. & Gould, K. L. State of the APC/C: Organization, function, and structure. *Critical Reviews in Biochemistry and Molecular Biology* **46**, 118–136 (2011).

20. Hochegger, H., Takeda, S. & Hunt, T. Cyclin-dependent kinases and cell-cycle transitions: Does one fit all? *Nature Reviews Molecular Cell Biology* **9**, 910–916 (2008).

21. Killander, D. & Zetterberg, A. A quantitative cytochemical investigation of the relationship between cell mass and initiation of DNA synthesis in mouse fibroblasts in vitro. *Exp. Cell Res.* **40**, 12–20 (1965).

22. Jorgensen, P., Nishikawa, J. L., Breitkreutz, B. J. & Tyers, M. Systematic identification of pathways that couple cell growth and division in yeast. *Science (80-.).* **297**, 395–400 (2002).

23. Latif, C., den Elzen, N. R. & O'Connell, M. J. DNA damage checkpoint maintenance through sustained Chk1 activity. *J. Cell Sci.* **117**, 3489–3498 (2004).

24. Giono, L. E. & Manfredi, J. J. The p53 tumor suppressor participates in multiple cell cycle checkpoints. *Journal of Cellular Physiology* **209**, 13–20 (2006).

25. Barnum, K. J. & O'connell, M. J. Chapter 2 Cell Cycle Regulation by Checkpoints. *Methods Mol. Biol.* **1170**, 29–40 (2014).

26. Musacchio, A. & Salmon, E. D. The spindle-assembly checkpoint in space and time. *Nat. Rev. Mol. Cell Biol.* **8**, 379–393 (2007).

27. A, D. A. *et al.* The Mad1/Mad2 complex as a template for Mad2 activation in the spindle assembly checkpoint. *Curr. Biol.* **15**, 214–225 (2005).

28. Waters, J. C., Chen, R. H., Murray, A. W. & Salmon, E. D. Localization of Mad2 to kinetochores depends on microtubule attachment, not tension. *J. Cell Biol.* **141**, 1181–1191 (1998).

29. Howell, B. J. *et al.* Cytoplasmic dynein/dynactin drives kinetochore protein transport to the spindle poles and has a role in mitotic spindle checkpoint inactivation. *J. Cell Biol.* **155**, 1159–1172 (2001).

30. Nicklas, R. B., Waters, J. C., Salmon, E. D. & Ward, S. C. Checkpoint signals in grasshopper meiosis are sensitive to microtubule attachment, but tension is still essential. *J. Cell Sci.* **114**, 4173–4183 (2001).

31. Tanaka, T. U. *et al.* Evidence that the Ipl1-Sli15 (Aurora Kinase-INCENP) complex promotes chromosome bi-orientation by altering kinetochore-spindle pole connections. *Cell* **108**, 317–329 (2002).

32. Pinsky, B. A. & Biggins, S. The spindle checkpoint: Tension versus attachment. *Trends in Cell Biology* **15**, 486–493 (2005).

33. Morrow, C. J. *et al.* Bub1 and aurora B cooperate to maintain BubR1-mediated inhibition of APC/CCdc20. *J. Cell Sci.* **118**, 3639–3652 (2005).

34. Hauf, S. *et al.* The small molecule Hesperadin reveals a role for Aurora B in correcting

kinetochore-microtubule attachment and in maintaining the spindle assembly checkpoint. *J. Cell Biol.* **161**, 281–294 (2003).

35. Murata-Hori, M., Tatsuka, M. & Wang, Y. L. Probing the dynamics and functions of aurora B kinase in living cells during mitosis and cytokinesis. *Mol. Biol. Cell* **13**, 1099–1108 (2002).

36. Mirny, L. A., Imakaev, M. & Abdennur, N. Two major mechanisms of chromosome organization. *Current Opinion in Cell Biology* **58**, 142–152 (2019).

37. Rowley, M. J. *et al.* Evolutionarily Conserved Principles Predict 3D Chromatin Organization. *Mol. Cell* **67**, 837-852.e7 (2017).

38. Davidson, I. F. & Peters, J. M. Genome folding through loop extrusion by SMC complexes. *Nature Reviews Molecular Cell Biology* (2021). doi:10.1038/s41580-021-00349-7

39. Rao, S. S. P. *et al.* Cohesin Loss Eliminates All Loop Domains. *Cell* **171**, 305-320.e24 (2017).

40. Solovei, I., Thanisch, K. & Feodorova, Y. How to rule the nucleus: divide et impera. *Current Opinion in Cell Biology* **40**, 47–59 (2016).

41. Grunstein, M. Histone acetylation in chromatin structure and transcription. *Nature* **389**, 349–352 (1997).

42. BJ, W. *et al.* A cascade of histone modifications induces chromatin condensation in mitosis. *Science* **343**, 77–80 (2014).

43. Boisvert, F. M., Van Koningsbruggen, S., Navascués, J. & Lamond, A. I. The multifunctional nucleolus. *Nature Reviews Molecular Cell Biology* **8**, 574–585 (2007).

44. Fatica, A. & Tollervey, D. Making ribosomes. *Current Opinion in Cell Biology* **14**, 313–318 (2002).

45. Tschochner, H. & Hurt, E. Pre-ribosomes on the road from the nucleolus to the cytoplasm. *Trends in Cell Biology* **13**, 255–263 (2003).

46. Lafontaine, D. L. J., Riback, J. A., Bascetin, R. & Brangwynne, C. P. The nucleolus as a multiphase liquid condensate. *Nature Reviews Molecular Cell Biology* **22**, 165–182 (2021).

47. Feric, M. *et al.* Coexisting Liquid Phases Underlie Nucleolar Subcompartments. *Cell* **165**, 1686–1697 (2016).

48. Stenström, L. *et al.* Mapping the nucleolar proteome reveals a spatiotemporal organization related to intrinsic protein disorder. *Mol. Syst. Biol.* **16**, e9469 (2020).

49. Mitrea, D. M. *et al.* Nucleophosmin integrates within the nucleolus via multi-modal interactions with proteins displaying R-rich linear motifs and rRNA. *Elife* **5**, (2016).

50. Yao, R. W. *et al.* Nascent Pre-rRNA Sorting via Phase Separation Drives the Assembly of Dense Fibrillar Components in the Human Nucleolus. *Mol. Cell* **76**, 767-783.e11 (2019).

51. Berry, J. *et al.* RNA transcription modulates phase transition-driven nuclear body assembly. *Proc. Natl. Acad. Sci. U. S. A.* **112**, E5237–E5245 (2015).

52. Booth, D. G. *et al.* Ki-67 is a PP1-interacting protein that organises the mitotic chromosome periphery. *Elife* **3**, (2014).

53. Knockenhauer, K. E. & Schwartz, T. U. The Nuclear Pore Complex as a Flexible and

Dynamic Gate. *Cell* **164**, 1162–1171 (2016).

54. Starr, D. A. & Fridolfsson, H. N. Interactions between nuclei and the cytoskeleton are mediated by SUN-KASH nuclear-envelope bridges. *Annual Review of Cell and Developmental Biology* **26**, 421–444 (2010).

55. Gruenbaum, Y. & Foisner, R. Lamins: Nuclear intermediate filament proteins with fundamental functions in nuclear mechanics and genome regulation. *Annu. Rev. Biochem.* **84**, 131–164 (2015).

56. Harada, T. *et al.* Nuclear lamin stiffness is a barrier to 3D migration, but softness can limit survival. *J. Cell Biol.* **204**, 669–682 (2014).

57. Guelen, L. *et al.* Domain organization of human chromosomes revealed by mapping of nuclear lamina interactions. *Nature* **453**, 948–951 (2008).

58. Beck, M. & Hurt, E. The nuclear pore complex: Understanding its function through structural insight. *Nature Reviews Molecular Cell Biology* **18**, 73–89 (2017).

59. Von Appen, A. & Beck, M. Structure Determination of the Nuclear Pore Complex with Three-Dimensional Cryo electron Microscopy. *Journal of Molecular Biology* **428**, 2001–2010 (2016).

60. Andersen, K. R. *et al.* Scaffold nucleoporins Nup188 and Nup192 share structural and functional properties with nuclear transport receptors. *Elife* **2013**, (2013).

61. Yoshida, K., Seo, H. S., Debler, E. W., Blobel, G. & Hoelz, A. Structural and functional analysis of an essential nucleoporin heterotrimer on the cytoplasmic face of the nuclear pore complex. *Proc. Natl. Acad. Sci. U. S. A.* **108**, 16571–16576 (2011).

62. Görlich, D., Prehn, S., Laskey, R. A. & Hartmann, E. Isolation of a protein that is essential for the first step of nuclear protein import. *Cell* **79**, 767–778 (1994).

63. Moore, M. S. & Blobel, G. The GTP-binding protein Ran/TC4 is required for protein import into the nucleus. *Nature* **365**, 661–663 (1993).

64. Ribbeck, K., Lipowsky, G., Kent, H. M., Stewart, M. & Görlich, D. NTF2 mediates nuclear import of Ran. *EMBO J.* **17**, 6587–6598 (1998).

65. Rexach, M. & Blobel, G. Protein import into nuclei: association and dissociation reactions involving transport substrate, transport factors, and nucleoporins. *Cell* **83**, 683–692 (1995).

66. Rout, M. P., Aitchison, J. D., Magnasco, M. O. & Chait, B. T. Virtual gating and nuclear transport: The hole picture. *Trends Cell Biol.* **13**, 622–628 (2003).

67. Schmidt, H. B. & Görlich, D. Transport Selectivity of Nuclear Pores, Phase Separation, and Membraneless Organelles. *Trends in Biochemical Sciences* **41**, 46–61 (2016).

68. Banani, S. F. *et al.* Compositional Control of Phase-Separated Cellular Bodies. *Cell* **166**, 651–663 (2016).

69. Frey, S., Richter, R. P. & Görlich, D. FG-rich repeats of nuclear pore proteins form a three-dimensional meshwork with hydrogel-like properties. *Science (80-.).* **314**, 815–817 (2006).

70. Ribbeck, K. & Görlich, D. The permeability barrier of nuclear pore complexes appears to operate via hydrophobic exclusion. *EMBO J.* **21**, 2664–2671 (2002).

71. Frey, S. *et al.* Surface Properties Determining Passage Rates of Proteins through

Nuclear Pores. *Cell* **174**, 202-217.e9 (2018).

72. Paine, P. L., Moore, L. C. & Horowitz, S. B. Nuclear envelope permeability. *Nature* **254**, 109–114 (1975).

73. Panté, N. & Kann, M. Nuclear Pore Complex Is Able to Transport Macromolecules with Diameters of 39 nm. *Mol. Biol. Cell* **13**, 425–434 (2002).

74. Hellberg, T., Paßvogel, L., Schulz, K. S., Klupp, B. G. & Mettenleiter, T. C. Nuclear Egress of Herpesviruses: The Prototypic Vesicular Nucleocytoplasmic Transport. in *Advances in Virus Research* **94**, 81–140 (Academic Press Inc., 2016).

75. Maric, M. *et al.* A Functional Role for TorsinA in Herpes Simplex Virus 1 Nuclear Egress. *J. Virol.* **85**, 9667–9679 (2011).

76. Speese, S. D. *et al.* Nuclear envelope budding enables large ribonucleoprotein particle export during synaptic Wnt signaling. *Cell* **149**, 832–846 (2012).

77. Jokhi, V. *et al.* Torsin Mediates Primary Envelopment of Large Ribonucleoprotein Granules at the Nuclear Envelope. *Cell Rep.* **3**, 988–995 (2013).

78. Zila, V. *et al.* Cone-shaped HIV-1 capsids are transported through intact nuclear pores. *Cell* **184**, (2021).

79. Moore, M. J. & Proudfoot, N. J. Pre-mRNA Processing Reaches Back toTranscription and Ahead to Translation. *Cell* **136**, 688–700 (2009).

80. Rogozin, I. B., Carmel, L., Csuros, M. & Koonin, E. V. Origin and evolution of spliceosomal introns. *Biology Direct* **7**, (2012).

81. Palazzo, A. F. & Lee, E. S. Sequence determinants for nuclear retention and cytoplasmic export of mRNAs and lncRNAs. *Frontiers in Genetics* **9**, (2018).

82. Zemp, I. & Kutay, U. Nuclear export and cytoplasmic maturation of ribosomal subunits. *FEBS Lett.* **581**, 2783–2793 (2007).

83. Hedges, J., West, M. & Johnson, A. W. Release of the export adapter, Nmd3p, from the 60S ribosomal subunit requires Rpl10p and the cytoplasmic GTPase Lsg1p. *EMBO J.* **24**, 567–579 (2005).

84. West, M., Hedges, J. B., Chen, A. & Johnson, A. W. Defining the Order in Which Nmd3p and Rpl10p Load onto Nascent 60S Ribosomal Subunits. *Mol. Cell. Biol.* **25**, 3802–3813 (2005).

85. Champion, L., Linder, M. I. & Kutay, U. Cellular Reorganization during Mitotic Entry. *Trends Cell Biol.* **27**, 26–41 (2017).

86. Matthews, H. K. *et al.* Changes in Ect2 Localization Couple Actomyosin-Dependent Cell Shape Changes to Mitotic Progression. *Dev. Cell* **23**, 371–383 (2012).

87. Dao, V. T., Dupuy, A. G., Gavet, O., Caron, E. & de Gunzburg, J. Dynamic changes in Rap1 activity are required for cell retraction and spreading during mitosis. *J. Cell Sci.* **122**, 2996–3004 (2009).

88. Cramer, L. P. & Mitchison, T. J. Investigation of the mechanism of retraction of the cell margin and rearward flow of nodules during mitotic cell rounding. *Mol. Biol. Cell* **8**, 109–119 (1997).

89. Salbreux, G., Charras, G. & Paluch, E. Actin cortex mechanics and cellular morphogenesis. *Trends in Cell Biology* **22**, 536–545 (2012).

90. Laurell, E. *et al.* Phosphorylation of Nup98 by multiple kinases is crucial for NPC

disassembly during mitotic entry. *Cell* **144**, 539–550 (2011).

91. Mall, M. *et al.* Mitotic lamin disassembly is triggered by lipid-mediated signaling. *J. Cell Biol.* **198**, 981–990 (2012).

92. Fischle, W. *et al.* Regulation of HP1-chromatin binding by histone H3 methylation and phosphorylation. *Nature* **438**, 1116–1122 (2005).

93. Tseng, L. C. & Chen, R. H. Temporal control of nuclear envelope assembly by phosphorylation of lamin B receptor. *Mol. Biol. Cell* **22**, 3306–3317 (2011).

94. Nichols, R. J., Wiebe, M. S. & Traktman, P. The vaccinia-related kinases phosphorylate the N′ terminus of BAF, regulating its interaction with DNA and its retention in the nucleus. *Mol. Biol. Cell* **17**, 2451–2464 (2006).

95. Molitor, T. P. & Traktman, P. Depletion of the protein kinase VRK1 disrupts nuclear envelope morphology and leads to BAF retention on mitotic chromosomes. *Mol. Biol. Cell* **25**, 891–903 (2014).

96. Salina, D. *et al.* Cytoplasmic dynein as a facilitator of nuclear envelope breakdown. *Cell* **108**, 97–107 (2002).

97. Schlaitz, A. L., Thompson, J., Wong, C. L., Yates, J. & Heald, R. REEP3/4 ensure endoplasmic reticulum clearance from metaphase chromatin and proper nuclear envelope architecture. *Dev. Cell* **26**, 315–323 (2013).

98. Schweizer, N., Pawar, N., Weiss, M. & Maiato, H. An organelle-exclusion envelope assists mitosis and underlies distinct molecular crowding in the spindle region. *J. Cell Biol.* **210**, 695–704 (2015).

99. Gibcus, J. H. *et al.* A pathway for mitotic chromosome formation. *Science (80-.).* **359**, (2018).

100. Vagnarelli, P. *et al.* Condensin and Repo-Man-PP1 co-operate in the regulation of chromosome architecture during mitosis. *Nat. Cell Biol.* **8**, 1133–1142 (2006).

101. Ogryzko, V. V, Schiltz, L. R., Russanova, V., Howard, B. H. & Nakatani, Y. The transcriptional coactivators p300 and CBP are histone acetyltransferases. *Cell* **87**, 953–959 (1996).

102. Kruhlak, M. J. *et al.* Regulation of Global Acetylation in Mitosis through Loss of Histone Acetyltransferases and Deacetylases from Chromatin. *J. Biol. Chem.* **276**, 38307–38319 (2001).

103. Shogren-Knaak, M. *et al.* Histone H4-K16 acetylation controls chromatin structure and protein interactions. *Science (80-.).* **311**, 844–847 (2006).

104. Dorigo, B., Schalch, T., Bystricky, K. & Richmond, T. J. Chromatin fiber folding: Requirement for the histone H4 N-terminal tail. *J. Mol. Biol.* **327**, 85–96 (2003).

105. Chen, Q., Yang, R., Korolev, N., Liu, C. F. & Nordenskiöld, L. Regulation of Nucleosome Stacking and Chromatin Compaction by the Histone H4 N-Terminal Tail–H2A Acidic Patch Interaction. *J. Mol. Biol.* **429**, 2075–2092 (2017).

106. Kan, P.-Y., Caterino, T. L. & Hayes, J. J. The H4 Tail Domain Participates in Intra- and Internucleosome Interactions with Protein and DNA during Folding and Oligomerization of Nucleosome Arrays. *Mol. Cell. Biol.* **29**, 538–546 (2009).

107. Gibson, B. A. *et al.* Organization of Chromatin by Intrinsic and Regulated Phase Separation. *Cell* (2019). doi:10.1016/j.cell.2019.08.037

108. Cimini, D., Mattiuzzo, M., Torosantucci, L. & Degrassi, F. Histone hyperacetylation in mitosis prevents sister chromatid separation and produces chromosome segregation defects. *Mol. Biol. Cell* **14**, 3821–3833 (2003).

109. Maeshima, K. *et al.* A Transient Rise in Free Mg2+ Ions Released from ATP-Mg Hydrolysis Contributes to Mitotic Chromosome Condensation. *Curr. Biol.* **28**, 444-451.e6 (2018).

110. Dueva, R. *et al.* Neutralization of the Positive Charges on Histone Tails by RNA Promotes an Open Chromatin Structure. *Cell Chem. Biol.* **26**, 1436-1449.e5 (2019).

111. Booth, D. G. *et al.* 3D-CLEM Reveals that a Major Portion of Mitotic Chromosomes Is Not Chromatin. *Mol. Cell* **64**, 790–802 (2016).

112. Booth, D. G. & Earnshaw, W. C. Ki-67 and the Chromosome Periphery Compartment in Mitosis. *Trends in Cell Biology* **27**, 906–916 (2017).

113. Cuylen, S. *et al.* Ki-67 acts as a biological surfactant to disperse mitotic chromosomes. *Nature* **535**, 308–312 (2016).

114. Ohta, S. *et al.* The Protein Composition of Mitotic Chromosomes Determined Using Multiclassifier Combinatorial Proteomics. *Cell* **142**, 810–821 (2010).

115. Whitfield, M. L., George, L. K., Grant, G. D. & Perou, C. M. Common markers of proliferation. *Nature Reviews Cancer* **6**, 99–106 (2006).

116. Silva, T. M. C., Souza, S. D. S., De Almeida, T. F. & Andrade, Z. A. Ki-67 is expressed in multiplying forms of Schistosoma mansoni, but not in snail host tissues. *Mem. Inst. Oswaldo Cruz* **102**, 651–653 (2007).

117. Schluter, C. *et al.* The cell proliferation-associated antigen of antibody Ki-67: A very large, ubiquitous nuclear protein with numerous repeated elements, representing a new kind of cell cycle-maintaining proteins. *J. Cell Biol.* **123**, 513–522 (1993).

118. Mora-Bermúdez, F., Gerlich, D. & Ellenberg, J. Maximal chromosome compaction occurs by axial shortening in anaphase and depends on Aurora kinase. *Nat. Cell Biol.* **9**, 822–831 (2007).

119. Magalska, A. *et al.* RuvB-like atpases function in chromatin decondensation at the end of mitosis. *Dev. Cell* **31**, 305–318 (2014).

120. Ramadan, K. *et al.* Cdc48/p97 promotes reformation of the nucleus by extracting the kinase Aurora B from chromatin. *Nature* **450**, 1258–1262 (2007).

121. Lu, X. *et al.* Requirement for lamin B receptor and its regulation by importin β and phosphorylation in nuclear envelope assembly during mitotic exit. *J. Biol. Chem.* **285**, 33281–33293 (2010).

122. Chi, Y. H., Haller, K., Peloponese, J. M. & Jeang, K. T. Histone acetyltransferase hALP and nuclear membrane protein hsSUN1 function in de-condensation of mitotic chromosomes. *J. Biol. Chem.* **282**, 27447–27458 (2007).

123. Schellhaus, A. K., De Magistris, P. & Antonin, W. Nuclear Reformation at the End of Mitosis. *J. Mol. Biol.* **428**, 1962–1985 (2016).

124. Samwer, M. *et al.* DNA Cross-Bridging Shapes a Single Nucleus from a Set of Mitotic Chromosomes. *Cell* **170**, 956-972.e23 (2017).

125. Zhang, C. Z. *et al.* Chromothripsis from DNA damage in micronuclei. *Nature* **522**, 179–184 (2015).

126. Anderson, D. J. & Hetzer, M. W. Nuclear envelope formation by chromatin-mediated reorganization of the endoplasmic reticulum. *Nat. Cell Biol.* **9**, 1160–1166 (2007).

127. Lu, L., Ladinsky, M. S. & Kirchhausen, T. Formation of the postmitotic nuclear envelope from extended ER cisternae precedes nuclear pore assembly. *J. Cell Biol.* **194**, 425–440 (2011).

128. Ye, Q., Callebaut, I., Pezhman, A., Courvalin, J. C. & Worman, H. J. Domain-specific interactions of human HP1-type chromodomain proteins and inner nuclear membrane protein LBR. *J. Biol. Chem.* **272**, 14983–14989 (1997).

129. Haraguchi, T. *et al.* Live cell imaging and electron microscopy reveal dynamic processes of BAF-directed nuclear envelope assembly. *J. Cell Sci.* **121**, 2540–2554 (2008).

130. Ulbert, S., Platani, M., Boue, S. & Mattaj, I. W. Direct membrane protein-DNA interactions required early in nuclear envelope assembly. *J. Cell Biol.* **173**, 469–476 (2006).

131. Schmitz, M. H. A. *et al.* Live-cell imaging RNAi screen identifies PP2A-B55α and importin-β 21 as key mitotic exit regulators in human cells. *Nat. Cell Biol.* **12**, 886–893 (2010).

132. Hirota, T., Lipp, J. J., Toh, B. H. & Peters, J. M. Histone H3 serine 10 phosphorylation by Aurora B causes HP1 dissociation from heterochromatin. *Nature* **438**, 1176–1180 (2005).

133. Asencio, C. *et al.* Coordination of kinase and phosphatase activities by Lem4 enables nuclear envelope reassembly during mitosis. *Cell* **150**, 122–135 (2012).

134. Ma, Y. *et al.* Lamin B receptor plays a role in stimulating nuclear envelope production and targeting membrane vesicles to chromatin during nuclear envelope assembly through direct interaction with importin β. *J. Cell Sci.* **120**, 520–530 (2007).

135. Vietri, M. *et al.* Spastin and ESCRT-III coordinate mitotic spindle disassembly and nuclear envelope sealing. *Nature* **522**, 231–235 (2015).

136. Newport, J. W., Wilson, K. L. & Dunphy, W. G. A lamin-independent pathway for nuclear envelope assembly. *J. Cell Biol.* **111**, 2247–2259 (1990).

137. Antonin, W., Ellenberg, J. & Dultz, E. Nuclear pore complex assembly through the cell cycle: Regulation and membrane organization. *FEBS Letters* **582**, 2004–2016 (2008).

138. Franz, C. *et al.* MEL-28/ELYS is required for the recruitment of nucleoporins to chromatin and postmitotic nuclear pore complex assembly. *EMBO Rep.* **8**, 165–172 (2007).

139. Antonin, W., Franz, C., Haselmann, U., Antony, C. & Mattaj, I. W. The integral membrane nucleoporin pom121 functionally links nuclear pore complex assembly and nuclear envelope formation. *Mol. Cell* **17**, 83–92 (2005).

140. Otsuka, S. *et al.* Postmitotic nuclear pore assembly proceeds by radial dilation of small membrane openings. *Nat. Struct. Mol. Biol.* **25**, 21–28 (2018).

141. Liu, S. & Pellman, D. The coordination of nuclear envelope assembly and chromosome segregation in metazoans. *Nucleus* **11**, 35–52 (2020).

142. D'Angelo, M. A., Anderson, D. J., Richard, E. & Hetzer, M. W. Nuclear pores form de novo from both sides of the nuclear envelope. *Science (80-.).* **312**, 440–443 (2006).

143. Rohn, J. L. *et al.* Myo19 ensures symmetric partitioning of mitochondria and coupling

of mitochondrial segregation to cell division. *Curr. Biol.* **24**, 2598–2605 (2014).

144. Hatch, A. L., Gurel, P. S. & Higgs, H. N. Novel roles for actin in mitochondrial fission. *Journal of Cell Science* **127**, 4549–4560 (2014).

145. Tsai, Y. J., Lee, H. I. & Lin, A. Ribosome distribution in HeLa cells during the cell cycle. *PLoS One* **7**, 32820 (2012).

146. Swanson, J. A. & Mcneil, P. L. Nuclear reassembly excludes large macromolecules. *Science (80-.).* **238**, 548–550 (1987).

147. Schneider, M. W. G. *et al.* A chromatin phase transition protects mitotic chromosomes against microtubule perforation. *bioRxiv* 2021.07.05.450834 (2021). doi:10.1101/2021.07.05.450834

148. Cuylen-Haering, S. *et al.* Chromosome clustering by Ki-67 excludes cytoplasm during nuclear assembly. *Nature* 1–6 (2020). doi:10.1038/s41586-020-2672-3

149. Nabet, B. *et al.* The dTAG system for immediate and target-specific protein degradation. *Nat. Chem. Biol.* **14**, 431–441 (2018).

150. Daniel, K. *et al.* Conditional control of fluorescent protein degradation by an auxin-dependent nanobody. *Nat. Commun.* **9**, 1–13 (2018).

151. Li, S., Prasanna, X., Salo, V. T., Vattulainen, I. & Ikonen, E. An efficient auxin-inducible degron system with low basal degradation in human cells. *Nat. Methods* **16**, 866–869 (2019).

152. Yesbolatova, A. *et al.* The auxin-inducible degron 2 technology provides sharp degradation control in yeast, mammalian cells, and mice. *Nat. Commun.* **11**, 1–13 (2020).

153. Iborra, F. J., Jackson, D. A. & Cook, P. R. Coupled transcription and translation within nuclei of mammalian cells. *Science (80-.).* **293**, 1139–1142 (2001).

154. David, A. *et al.* Nuclear translation visualized by ribosome-bound nascent chain puromycylation. *J. Cell Biol.* **197**, 45–57 (2012).

155. Nathanson, L., Xia, T. & Deutscher, M. P. Nuclear protein synthesis: A re-evaluation. *RNA* **9**, 9–13 (2003).

156. Bohnsack, M. T. *et al.* Exp5 exports eEF1A via tRNA from nuclei and synergizes with other transport pathways to confine translation to the cytoplasm. *EMBO J.* **21**, 6205–6215 (2002).

157. Calado, A., Treichel, N., Müller, E. C., Otto, A. & Kutay, U. Exportin-5-mediated nuclear export of eukaryotic elongation factor 1A and tRNA. *EMBO J.* **21**, 6216–6224 (2002).